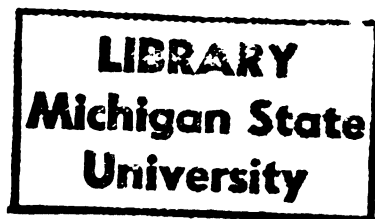




25024131



This is to certify that the

dissertation entitled

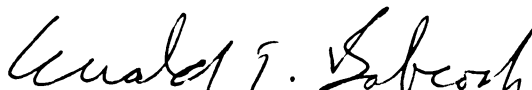
Characterization of the Vibrational Properties  
of Metallochlorins, Chlorophylls and Chlorophyll -  
Binding Proteins by Resonance Raman Spectroscopy

presented by

Harold Fonda

has been accepted towards fulfillment  
of the requirements for

PHD degree in Chemistry

  
Major professor

Date October 3, 1989

**PLACE IN RETURN BOX to remove this checkout from your record.  
TO AVOID FINES return on or before date due.**

<b>DATE DUE</b>	<b>DATE DUE</b>	<b>DATE DUE</b>
_____	_____	_____
_____	_____	_____
_____	_____	_____
_____	_____	_____
_____	_____	_____
_____	_____	_____
_____	_____	_____

**MSU Is An Affirmative Action/Equal Opportunity Institution**

CHARACTERIZATION OF THE VIBRATIONAL PROPERTIES OF  
METALLOCHLORINS, CHLOROPHYLLS AND CHLOROPHYLL-BINDING  
PROTEINS BY RESONANCE RAMAN SPECTROSCOPY

By

Harold Norman Fonda

A DISSERTATION

Submitted to  
Michigan State University  
in partial fulfillment of the requirements  
for the degree of

DOCTOR OF PHILOSOPHY

Department of Chemistry

1989



605954

## ABSTRACT

# CHARACTERIZATION OF THE VIBRATIONAL PROPERTIES OF METALLOCHLORINS, CHLOROPHYLLS AND CHLOROPHYLL-BINDING PROTEINS BY RESONANCE RAMAN SPECTROSCOPY

By

Harold Norman Fonda

Three systems of increasing complexity from metallo-chlorin model compounds to chlorophylls to chlorophyll-binding proteins have been studied. Resonance Raman and IR spectra of metallo-octaethylchlorins (MOEC) show significant differences in the vibrational mode properties of metallochlorins and metalloporphyrins. The core-size correlation parameters for Zn, Cu and NiOEC reveal mixing of  $C_aC_m$  and  $C_bC_b$  stretching character in the high frequency modes. The isotopic frequency shifts observed for the  $\nu_3$  and  $\nu_{10}$  modes of fully and partially deuterated copper octaethylporphyrin establish that, for a delocalized vibrational mode, methine  $d_2$  deuteration produces half of the  $d_4$  shift. CuOEC exhibits different patterns of frequency shifts upon  $\alpha, \beta$  and  $\gamma, \delta$  methine deuteration that demonstrate the phenomenon of mode localization in metallo-chlorins.

The vibrational mode characteristics determined for MOEC provide the basis for the interpretation of the resonance Raman spectra of metallochlorin  $\pi$  cation radicals and

metal-substituted chlorophyll a. Resonance Raman spectra of the  $\pi$  cation radicals of CuOEC and selectively methine-deuterated CuOEC complexes show that unlike the situation in metalloporphyrins, changes in mode composition occur upon macrocycle oxidation in metallochlorins. Metal-substituted chlorophyll a complexes display altered mode compositions compared to MOEC as a result of addition of the isocyclic ring. Identification of the core-size sensitive modes in these complexes provides a reliable method to determine the coordination state of chlorophyll a in solution and in vivo. The results obtained for chlorophyll a in solution have been extended to chlorophyll-binding proteins. Resonance Raman spectra of the light-harvesting chlorophyll a/b protein complex (LHC) show four populations of chlorophyll a and two of chlorophyll b that are distinguished by the stretching frequencies of their conjugated carbonyl groups. Each of the chlorophylls has a 5-coordinate Mg atom. The chlorophyll b and two of the chlorophyll a populations result from H-bonds of different strength to the carbonyl groups. H-bonding to the conjugated carbonyls is proposed as a mechanism to account for the broadened and red-shifted electronic absorption bands of the chlorophylls in LHC.

To my parents and in memory of my  
grandfather, Neil W. Stuart.

## ACKNOWLEDGMENTS

I would like to thank Dr. Gerald T. Babcock for his support and guidance; Dr. George E. Leroi for serving as Second Reader; Tony Oertling and Asaad Salehi for their collaboration on the chlorin and  $\pi$  cation radical work; Dwight Lillie and Matt Espe for maintaining the computer system; and Bob Kean and Chris Bender for comic relief.

## TABLE OF CONTENTS

LIST OF TABLES	ix
LIST OF FIGURES	xi
CHAPTER 1 INTRODUCTION	
1. The Role of Chlorophyll in Photosynthesis	1
2. The Structure of Metalloporphyrins, Metallochlorins and Chlorophyll	5
3. The Electronic Absorption Spectra of Metalloporphyrins and Metallochlorins	9
4. Infrared and Raman Spectroscopy	15
5. Vibrational Mode Assignments for Metalloporphyrins	19
6. The Application of Resonance Raman Spectroscopy to the Study of Chlorophyll	25
7. Aim and Scope of this Work	26
CHAPTER 2 MATERIALS AND METHODS	
1. Materials	27
i. Preparation of Chlorins	27
ii. Preparation of Chlorophyll a and b	28
iii. Preparation of Metal-Substituted Chlorophyll a	29
iv. Isolation of Chlorophyll-Binding Proteins	30

2. Spectroscopic Techniques	31
i. Electronic Absorption Spectroscopy	31
ii. Infrared Spectroscopy	31
iii. Resonance Raman Spectroscopy	31

### CHAPTER 3 VIBRATIONAL PROPERTIES OF METALLOCHLORINS

1. Introduction	35
2. Results	39
i. Electronic Absorption Spectra	39
ii. Resonance Raman Spectra of MOEC	42
iii. IR Spectra of MOEC	47
iv. Effects of Methine Deuteration	51
v. Resonance Raman Spectra of CuECI	57
vi. Solid State Spectra	59
3. Discussion	62
i. $C_aC_m$ and $C_bC_b$ Modes	62
ii. $C_aN$ Modes	74
iii. $C_mH$ Modes	76
iv. Ethyl Group Vibrations	79
4. Conclusions	80

### CHAPTER 4 VIBRATIONAL PROPERTIES OF METALLOCHLORIN

#### $\pi$ CATION RADICALS

1. Introduction	82
2. Results	86
3. Discussion	90
4. Conclusions	97

<b>CHAPTER 5 VIBRATIONAL PROPERTIES OF METALLOCHLOROPHYLLS</b>	
1. Introduction	99
2. Results	103
i. Electronic Absorption Spectra	103
ii. Resonance Raman Spectra	107
3. Discussion	110
4. Conclusions	116
 <b>CHAPTER 6 RESONANCE RAMAN SPECTROSCOPY OF CHLOROPHYLL-BINDING PROTEINS</b>	
1. Introduction	118
2. Results	127
i. Electronic Absorption Spectra	127
ii. Resonance Raman Spectra	129
3. Discussion	140
i. Selective Enhancement of Chlorophyll a and Chlorophyll b	140
ii. Mg Coordination State	144
iii. Carbonyl Stretching Region	147
iv. 28 kDa and Reaction Center Complex Proteins	151
4. Conclusions	153
 <b>CHAPTER 7 SUGGESTIONS FOR FURTHER WORK</b>	 155
 <b>LIST OF REFERENCES</b>	 162

## LIST OF TABLES

Table 1.1	Observed and calculated frequencies ( $\text{cm}^{-1}$ ) of NiOEP for modes in the region from 900 to $1700 \text{ cm}^{-1}$ (from ref. 55)	21
Table 3.1	Electronic absorption maxima (nm) for MOEC complexes in benzene solution	41
Table 3.2	Electronic absorption maxima (nm) for MOEP complexes in benzene solution	42
Table 3.3	Vibrational frequencies ( $\text{cm}^{-1}$ ) and Raman depolarization ratios of MOEC	44
Table 3.4	Vibrational frequencies ( $\text{cm}^{-1}$ ), isotope shifts ( $\text{cm}^{-1}$ ) and core-size correlation parameters for metallochlorin $\text{C}_4\text{C}_m$ and $\text{C}_6\text{C}_b$ normal modes	67
Table 3.5	Vibrational frequencies ( $\text{cm}^{-1}$ ), isotope shifts ( $\text{cm}^{-1}$ ) and core-size correlation parameters for metalloporphyrin $\text{C}_4\text{C}_m$ and $\text{C}_6\text{C}_b$ normal modes	68
Table 3.6	Vibrational frequencies ( $\text{cm}^{-1}$ ) and isotope shifts ( $\text{cm}^{-1}$ ) for metallochlorin $\text{C}_4\text{N}$ modes	75
Table 3.7	Vibrational frequencies ( $\text{cm}^{-1}$ ) for CuOEC normal modes in the frequency region below $1350 \text{ cm}^{-1}$	77
Table 4.1	Predicted and observed frequency shifts for porphyrin normal modes upon oxidation (from ref. 99)	92
Table 4.2	Mode characters predicted for CuOEC/CuOEC <sup>+</sup>	94



Table 4.3	Vibrational frequencies ( $\text{cm}^{-1}$ ) and isotope shifts ( $\text{cm}^{-1}$ ) for the high frequency resonance Raman modes of CuOEC and CuOEC <sup>+</sup> .	95
Table 5.1	Chlorophylls and chlorophyll-derivatives for which resonance Raman spectra have been reported	101
Table 5.2	Electronic absorption maxima (nm) for metal-substituted chlorophyll a in diethyl ether solution	105
Table 5.3	Electronic absorption maxima (nm) for chlorophyll a in various solvents	107
Table 5.4	Resonance Raman frequencies ( $\text{cm}^{-1}$ ) and core-size correlation parameters for metal-substituted chlorophyll a	109
Table 6.1	Electronic absorption maxima (nm) of chlorophyll a and chlorophyll b	127
Table 6.2	Chlorophyll a and chlorophyll b carbonyl stretching frequencies ( $\text{cm}^{-1}$ ) in LHC	147

## LIST OF FIGURES

Figure 1.1 Structure and labelling scheme for chlorophyll a	2
Figure 1.2 Structure and labelling scheme for a) metallo-octaethylporphyrin (MOEP) and b) <u>trans</u> -metallo-octaethylchlorin (MOEC)	6
Figure 1.3 Molecular structure of a) Fe <sup>II</sup> OEP and b) Fe <sup>II</sup> OEC as determined by X-ray crystallography (from ref. 35)	8
Figure 1.4 Electronic absorption spectrum of copper octaethylporphyrin (CuOEP) in CH <sub>2</sub> Cl <sub>2</sub> solution	10
Figure 1.5 Porphyrin M.O.'s comprising the Gouterman four-orbital model (from ref. 42)	12
Figure 1.6 Electronic absorption spectrum of copper octaethylchlorin (CuOEC) in CH <sub>2</sub> Cl <sub>2</sub> solution	14
Figure 1.7 Molecular processes associated with a) Infrared and b) Raman spectroscopy (from ref. 45)	16
Figure 1.8 Atomic displacements in the $\nu_2$ vibrational mode of NiOEP (from ref. 55)	23
Figure 2.1 Diagram of the apparatus used for the collection of Raman spectra of KBr disc samples	34
Figure 3.1 Structure and labelling scheme for metallo- chlorin model compounds. MOEC = <u>trans</u> - metallo-octaethylchlorin and MECI = <u>trans</u> - metallo-etiochlorin I	38

Figure 3.2	Electronic absorption spectra of ZnOEC, CuOEC and NiOEC in benzene solution	40
Figure 3.3	Resonance Raman spectra of ZnOEC, CuOEC and NiOEC in CH <sub>2</sub> Cl <sub>2</sub> solution obtained with Soret excitation at 406.7 nm. Laser powers: 5, 7 and 20 mW, respectively	43
Figure 3.4	Resonance Raman spectra of CuOEC in CH <sub>2</sub> Cl <sub>2</sub> solution obtained with Q <sub>x</sub> excitation at 488.0 nm and Q <sub>y</sub> excitation at 615.0 nm. Laser powers: 100 and 35 mW, respectively	48
Figure 3.5	Resonance Raman spectra of NiOEC in CH <sub>2</sub> Cl <sub>2</sub> solution obtained with Q <sub>x</sub> excitation at 488.0 nm and Q <sub>y</sub> excitation at 615.0 nm. Laser powers: 70 and 40 mW, respectively	49
Figure 3.6	IR spectra of ZnOEC, CuOEC and NiOEC in CCl <sub>4</sub> solution	50
Figure 3.7	IR spectra of CuOEC- $\gamma,\delta$ -d <sub>2</sub> , CuOEC- $\alpha,\beta$ -d <sub>2</sub> and CuOEC-d <sub>4</sub> in CCl <sub>4</sub> solution	52
Figure 3.8	Resonance Raman spectra of CuOEC- $\gamma,\delta$ -d <sub>2</sub> , CuOEC- $\alpha,\beta$ -d <sub>2</sub> and CuOEC-d <sub>4</sub> in CH <sub>2</sub> Cl <sub>2</sub> solution obtained with Q <sub>y</sub> excitation at 615.0 nm. Laser power: 40 mW	53
Figure 3.9	Resonance Raman spectra of CuOEP, CuOEP-d <sub>2</sub> and CuOEP-d <sub>4</sub> in CH <sub>2</sub> Cl <sub>2</sub> solution obtained with Soret excitation at 406.7 nm. Laser power: 10 mW	55
Figure 3.10	Resonance Raman spectra of CuOEP, CuOEP-d <sub>2</sub> and CuOEP-d <sub>4</sub> in CH <sub>2</sub> Cl <sub>2</sub> solution obtained with visible excitation at 514.5 nm. Laser power: 50 mW	56
Figure 3.11	Resonance Raman spectra of CuECI in CH <sub>2</sub> Cl <sub>2</sub> solution obtained with Soret excitation at 406.7 nm, Q <sub>x</sub> excitation at 488.0 nm and Q <sub>y</sub> excitation at 615.0 nm. Laser powers: 6, 70 and 40 mW, respectively	58

Figure 3.12	Resonance Raman spectra of NiOEC in KBr obtained with Soret excitation at 406.7 nm, $Q_x$ excitation at 488.0 nm and $Q_y$ excitation at 615.0 nm. Laser powers: 20, 70 and 50 mW, respectively	60
Figure 3.13	Resonance Raman spectra of CuOEC in KBr obtained with Soret excitation at 406.7 nm, $Q_x$ excitation at 488.0 nm and $Q_y$ excitation at 615.0 nm. Laser powers: 20, 75 and 50 mW, respectively	61
Figure 3.14	Core-size correlation for the high frequency modes of MOEC	65
Figure 3.15	Core-size correlation for the resonance Raman active (—) and IR active (- -) high frequency modes of MOEP	66
Figure 4.1	Structure of metallo-methyloctaethylchlorin (MMeOEC)	84
Figure 4.2	Electronic absorption spectrum of CuOEC <sup>+</sup> in CH <sub>2</sub> Cl <sub>2</sub> solution	87
Figure 4.3	Resonance Raman spectra of CuOEC, CuOEC- $\gamma, \delta$ -d <sub>2</sub> , CuOEC- $\alpha, \beta$ -d <sub>2</sub> , CuOEC-d <sub>4</sub> and CuECI in CH <sub>2</sub> Cl <sub>2</sub> solution obtained with Soret excitation at 363.8 nm	88
Figure 4.4	Resonance Raman spectra of CuOEC <sup>+</sup> , CuOEC- $\gamma, \delta$ -d <sub>2</sub> <sup>+</sup> , CuOEC- $\alpha, \beta$ -d <sub>2</sub> <sup>+</sup> , CuOEC-d <sub>4</sub> <sup>+</sup> and CuECI <sup>+</sup> in CH <sub>2</sub> Cl <sub>2</sub> solution obtained with Soret excitation at 363.8 nm	89
Figure 4.5	Electron density contour maps for the a <sub>1u</sub> and a <sub>2u</sub> orbitals of a) free base porphine and b) free base chlorin (from ref. 123)	91
Figure 5.1	Electronic absorption spectra of chlorophyll a and Zn, Cu and Ni-substituted chlorophyll a in diethyl ether solution	104
Figure 5.2	Electronic absorption spectra of chlorophyll a in acetone, methanol and pyridine solution	106

Figure 5.3	Resonance Raman spectra of chlorophyll a in acetone solution and Zn, Cu and Ni-substituted chlorophyll a in diethyl ether solution obtained with Soret excitation at 406.7 nm. Laser powers: 35, 20, 20 and 20 mW, respectively	108
Figure 5.4	Resonance Raman spectra of chlorophyll a in acetone, pyridine, methanol and diethyl ether solution obtained with Soret excitation at 441.6 nm. Laser powers: 20, 15, 15 and 15 mW, respectively	111
Figure 6.1	Proposed arrangement of the polypeptides and electron transfer components in the PS II/OEC complex (from ref. 154)	121
Figure 6.2	Arrangement of pigments in the L and M subunits of the reaction center from <u>Rhodopseudomonas viridis</u> (from ref. 158)	123
Figure 6.3	Electronic absorption spectrum of LHC isolated from pea leaves	128
Figure 6.4	Electronic absorption spectra of LHC, the 28 kDa chlorophyll a-binding protein and the LHC-depleted Photosystem II reaction center complex isolated from spinach	130
Figure 6.5	Resonance Raman spectra of LHC at -125°C obtained with 413.1 and 441.6 nm excitation. Laser powers: 28 and 25 mW, respectively	131
Figure 6.6	Resonance Raman spectra of LHC at -125°C obtained with 472.7 and 514.5 nm excitation. Laser power: 45 mW	132
Figure 6.7	Resonance Raman spectra of chlorophyll a in acetone at -125°C obtained with 413.1 and 441.6 nm excitation. Laser powers: 19 and 22 mW, respectively	133

Figure 6.8	Resonance Raman spectra of chlorophyll b in acetone at -125°C obtained with 441.6 and 472.7 nm excitation. Laser powers: 20 and 40 mW, respectively	135
Figure 6.9	Resonance Raman spectra of LHC, the 28 kDa protein and the reaction center complex obtained with 406.7 nm excitation. Laser power: 20 mW	136
Figure 6.10	Resonance Raman spectra of LHC, the 28 kDa protein and the reaction center complex obtained with 441.6 nm excitation. Laser power: 22 mW	138
Figure 6.11	Resonance Raman spectra of LHC, the 28 kDa protein and the reaction center complex obtained with 476.5 nm excitation. Laser power: 25 mW	139
Figure 6.12	Calculated excitation profiles for a 1600 $\text{cm}^{-1}$ mode and a 300 $\text{cm}^{-1}$ mode of chlorophyll a (—) and chlorophyll b (- -) in LHC	143

## CHAPTER 1

### INTRODUCTION

#### 1. The Role of Chlorophyll in Photosynthesis

In the process of photosynthesis in higher plants, light energy absorbed by chlorophyll is utilized to convert water and carbon dioxide into oxygen and stored chemical energy in the form of carbohydrate (1,2). Ingenhousz in 1779 showed that it is the green parts of plants that are involved. The structure of the green pigment chlorophyll (Figure 1.1) was determined by Willstätter and Stoll in the early 1900's; at the same time organomagnesium reagents were being developed by Grignard. This coincidence led to the (incorrect) idea that photosynthesis occurred by the photodecomposition of carbon dioxide bound to chlorophyll. More recent work has shown that the photosynthetic process is considerably more complex.

In our present understanding of photosynthesis in higher plants, there are two photosystems (called Photosystem I and Photosystem II) that operate in series to drive a sequence of electron transfer reactions (3). These reactions culminate in the splitting of oxygen from water and the formation of NADPH

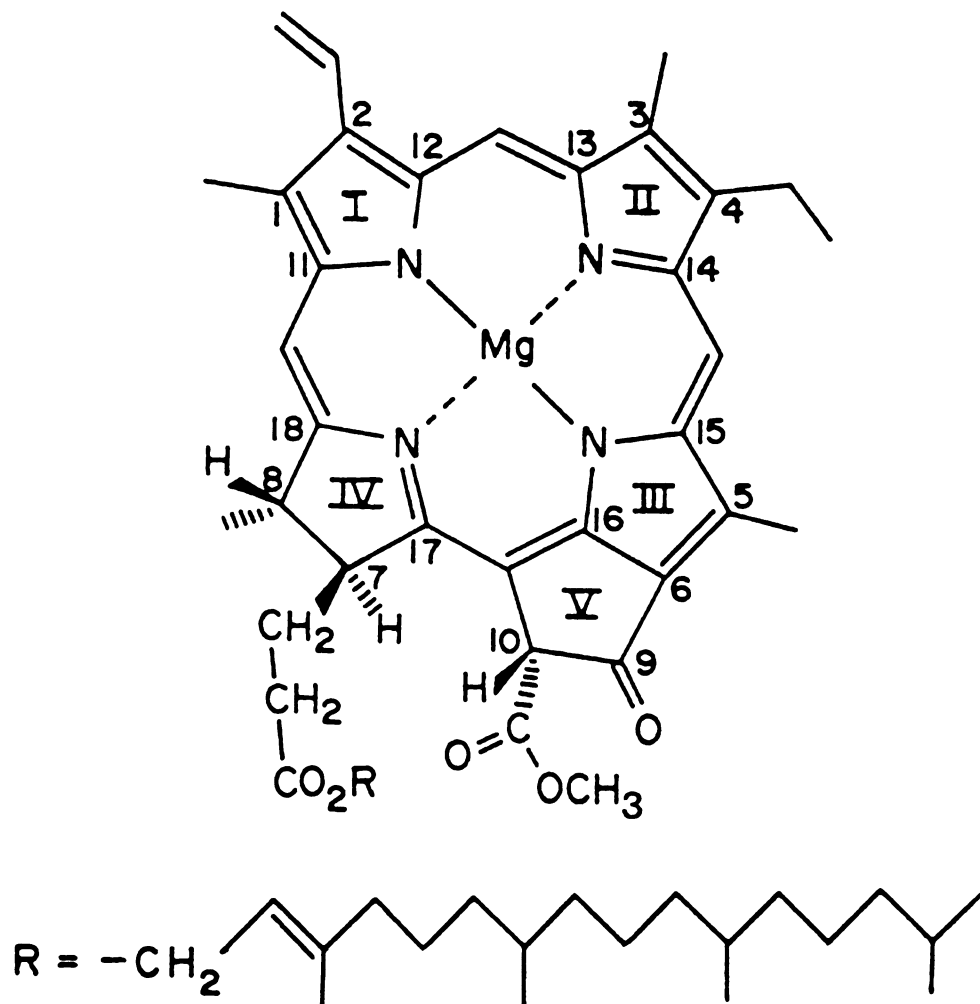


Figure 1.1 Structure and labelling scheme for chlorophyll a



(= reduced nicotinamide-adenine dinucleotide phosphate) and ATP (= adenosine triphosphate) to be used for the subsequent reduction of carbon dioxide. The components of the two Photosystems in the electron transfer chain are arranged within protein complexes embedded in the photosynthetic membrane. At the heart of these Photosystems are chlorophyll a molecules that form the reaction centers, P-700 (P-700 refers to a pigment with an electronic absorption maximum at 700 nm) of Photosystem I (4) and P-680 of Photosystem II (5). The primary energy conversion processes in photosynthesis occur at these sites.

The exact nature of the P-680 and P-700 reaction center chlorophylls has been difficult to ascertain. P-680 is thought to be a ligated monomeric chlorophyll a (6) whereas P-700 may have a dimeric structure (7-14). Other structures for P-700 that have been suggested are the enol form of chlorophyll a (15),  $\delta$ -chloro-substituted 10-hydroxy-chlorophyll a (16) or chlorophyll a' (the C<sub>10</sub> epimer of chlorophyll a) (17). The reaction center chlorophylls have electronic absorption maxima in the visible region that are red-shifted compared to the 662 nm absorption maximum of monomeric chlorophyll a in acetone solution. Further modification of the properties of the reaction center chlorophylls is seen by comparison of their mid-point potentials. The mid-point potential,  $E_m$  of chlorophyll a in an organic solvent is in the region of +0.8 V (6) but for P-700/P-700<sup>+</sup>,  $E_m$  = +0.49 V (18) and for P-680/P-680<sup>+</sup>,

$E_m = +1.1$  V (19). The high redox potential of  $P-680^+$  is necessary for the oxidation of water:  $2H_2O/O_2 + 4H^+$ , at pH 7.0,  $E_m = +0.82$  V or under estimated physiological conditions at pH 5.0,  $E_m = +0.93$  V.

The reaction center chlorophylls constitute less than 1% of the total number of chlorophyll molecules in the plant. The vast majority of chlorophylls are involved in light absorption and transfer of the excitation energy to the reaction centers. The major chlorophyll-binding protein is the light-harvesting chlorophyll a/b protein complex (LHC), which serves both Photosystem I and Photosystem II (20,21). LHC contains chlorophyll a and chlorophyll b molecules (chlorophyll b has a formyl group in the 3-position instead of a methyl group as in chlorophyll a) that absorb maximally at 677 and 652 nm, respectively. Additionally, there are separate sub-antenna complexes of chlorophyll a serving each Photosystem. The chlorophylls absorb maximally in the range 670 to 683 nm for the Photosystem II subantenna and 680 to 695 nm for the Photosystem I subantenna. This arrangement of light-harvesting and reaction center chlorophylls ensures that the light energy is distributed to both Photosystems and that energy transfer is "downhill" energetically to the reaction center. Directing the light energy absorbed by a large number of antenna chlorophylls to a single reaction center chlorophyll raises the photochemical turnover rate thereby increasing the efficiency of photosynthesis (22).

## 2. The Structure of Metalloporphyrins, Metallochlorins and Chlorophyll

A metalloporphyrin is a tetrapyrrole macrocycle with an extensively delocalized  $\pi$  electron system. Metalloporphyrins with a range of structures play important roles in numerous and diverse biological processes (23). The structure of a typical synthetic metalloporphyrin, that of metallo-octaethylporphyrin (MOEP) is shown in Figure 1.2(a). Without the central metal ion, hydrogens are bonded to two of the pyrrole nitrogens and the structure is known as the free base. In the labelling scheme,  $C_a$  and  $C_b$  refer to the carbon atoms of the pyrrole rings and  $C_m$  to the methine bridge carbons. The four methine bridge carbons are labelled  $\alpha$ ,  $\beta$ ,  $\gamma$  and  $\delta$ . The core-size of a metalloporphyrin is defined as the distance from the center of the macrocycle to the pyrrole nitrogen atoms ( $C_t$ -N distance). The core-size depends on the size and coordination state of the central metal ion and is determined from the X-ray crystal structures of representative metalloporphyrin complexes.

A metallochlorin is a derivative of a metalloporphyrin in which a  $C_bC_b$  bond of one of the pyrrole rings has been reduced (24). Figure 1.2(b) shows the structure of trans-metallo-octaethylchlorin (MOEC). Both cis- and trans-configurations of the reduced  $C_bC_b$  bond are possible. In nature, metallochlorins occur as the magnesium-containing

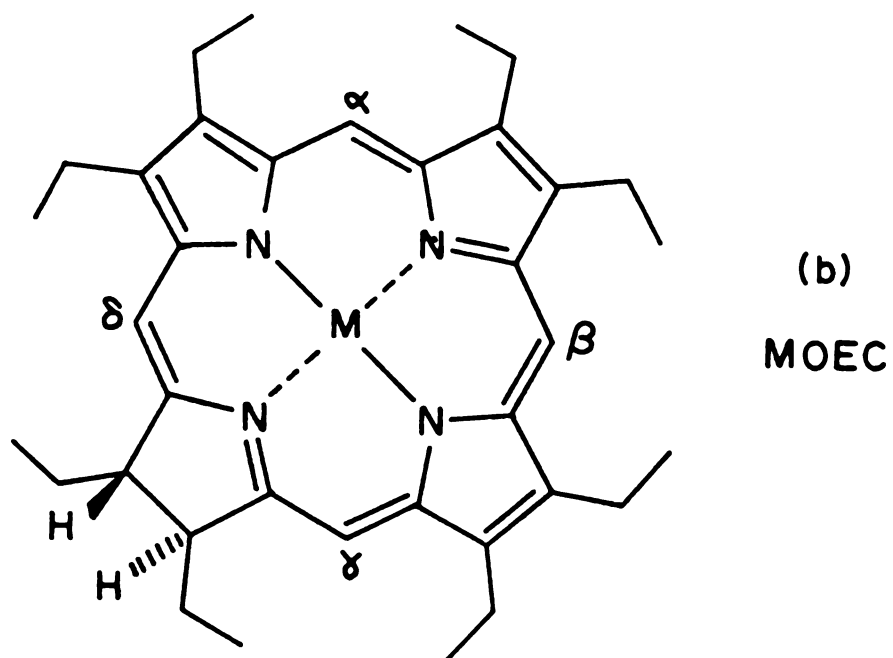
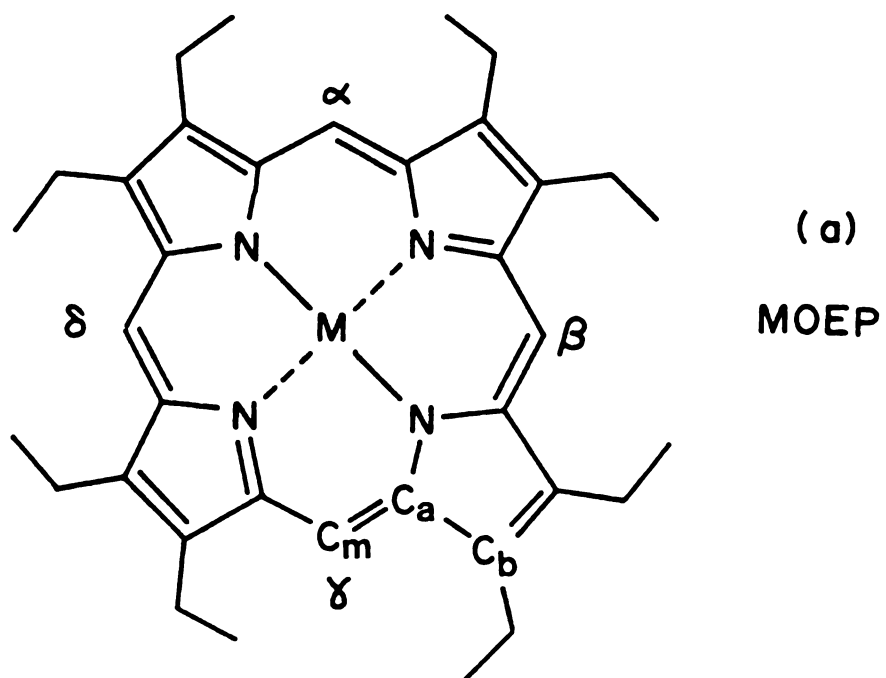


Figure 1.2 Structure and labelling scheme for a) metallo-octaethylporphyrin (MOEP) and b) trans-metallo-octaethylchlorin (MOEC)

chlorophyll pigments (25) and in iron-containing leukocyte myeloperoxidase (26,27) and bacterial heme d enzymes (28-30). Several studies have been directed towards elucidating the structural, redox and ligand-binding properties of metallo-chlorins (31-34) to determine the factors that make a chlorin the preferred macrocycle in these instances. A comparative study of  $\text{Fe}^{\text{II}}\text{OEP}$  and  $\text{Fe}^{\text{II}}\text{OEC}$  by X-ray crystallography (35) showed that the average iron-nitrogen distance is very similar in the two complexes (1.996 Å for  $\text{Fe}^{\text{II}}\text{OEP}$  and 1.986 Å for  $\text{Fe}^{\text{II}}\text{OEC}$ ). However, the porphyrin macrocycle in  $\text{Fe}^{\text{II}}\text{OEP}$  is planar but the chlorin macrocycle of  $\text{Fe}^{\text{II}}\text{OEC}$  is  $S_4$  ruffled (Figure 1.3). The core-size of the chlorin macrocycle in the planar conformation is intrinsically larger than the corresponding porphyrin macrocycle. Ruffling of the chlorin macrocycle reduces the core-size (and hence the metal-nitrogen distance) compared to the planar conformation. This distortion is possible because the chlorin, being less aromatic, has increased flexibility. Similar conformational flexibility was observed for nickel tetramethylchlorin compared to nickel tetramethylporphyrin (36).

The two main chlorophyll pigments in higher plants are chlorophyll a and chlorophyll b. A key structural feature of chlorophyll is the presence of a chlorin macrocycle with a trans-configuration of the hydrogens about the reduced  $\text{C}_b\text{C}_b$  bond of ring IV. Fused onto the chlorin macrocycle is a fifth ring containing a keto carbonyl group. The X-ray crystal

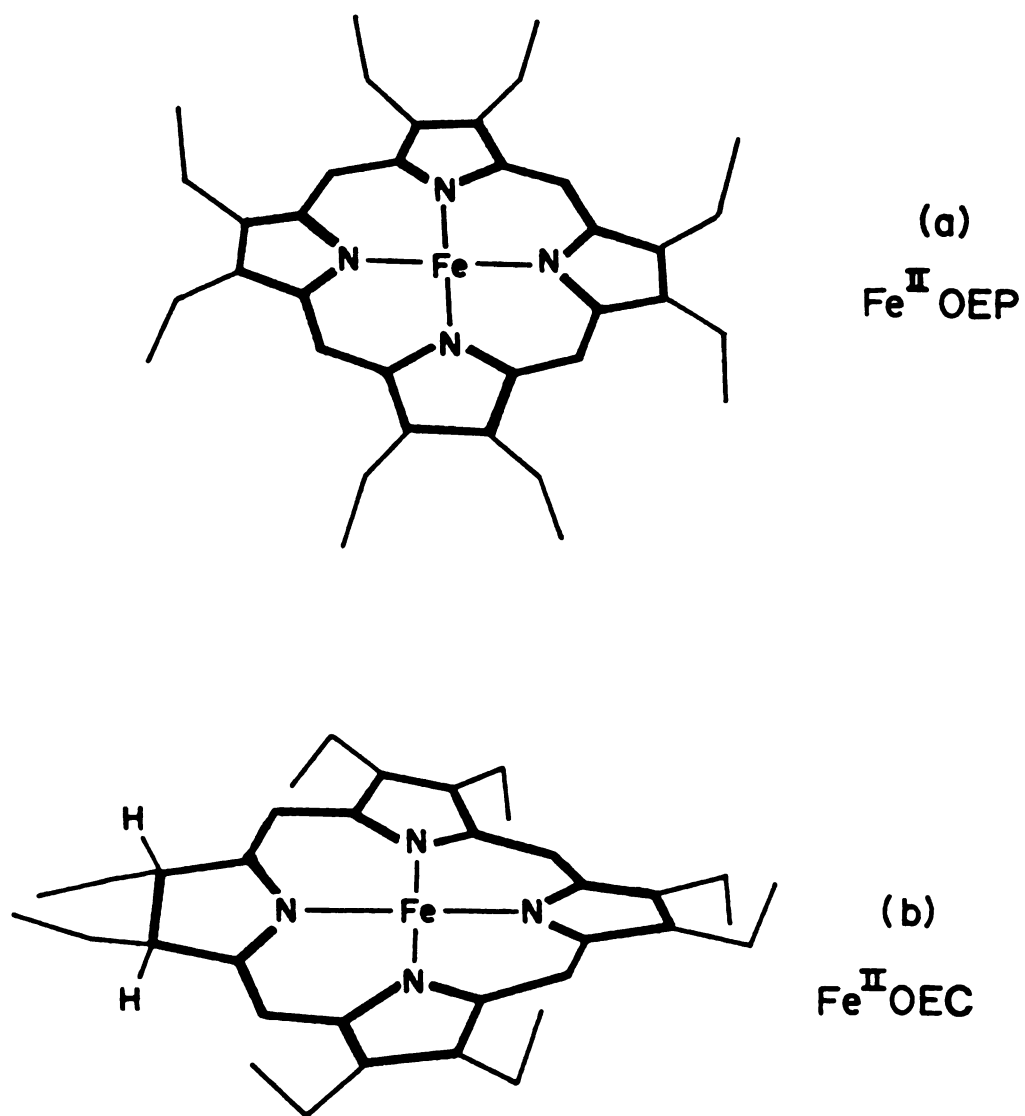


Figure 1.3 Molecular structure of a)  $\text{Fe}^{\text{II}}\text{OEP}$  and b)  $\text{Fe}^{\text{II}}\text{OEC}$  as determined by X-ray crystallography (from ref. 35)

structure of ethyl chlorophyllide a dihydrate (37) (where  $R = C_2H_5$ , in Figure 1.1) shows that the effect of the fifth ring is to reduce the amount of buckling of the macrocycle. This in turn increases the extent of conjugation of the keto carbonyl with the main  $\pi$  electron system. In the naturally-occurring chlorophyll pigments the central metal ion is magnesium. The free base form of chlorophyll is called a pheophytin. Photosynthetic bacteria utilize bacteriochlorophyll pigments in which both rings II and IV are reduced (25,38). Bacteriochlorophyll a has the same pattern of peripheral substituents as chlorophyll a except for replacement of the vinyl group by an acetyl group in the 2 position. Chlorophyll  $c_1$  and chlorophyll  $c_2$  are another type of naturally-occurring chlorophyll pigment found in diatoms and brown algae (25,39,40). Chlorophylls c have the same oxidation state as that of a porphyrin.

### 3. The Electronic Absorption Spectra of Metalloporphyrins and Metallochlorins

The electronic absorption spectrum of a typical metalloporphyrin of  $D_{4h}$  symmetry, copper octaethylporphyrin, in  $CH_2Cl_2$  solution is shown in Figure 1.4. The observed bands correspond to in-plane  $\pi - \pi^*$  electronic transitions which for a  $D_{4h}$  metalloporphyrin are of  $E_u$  symmetry. The intense transition around 400 nm is called the Soret or B band. The two weaker

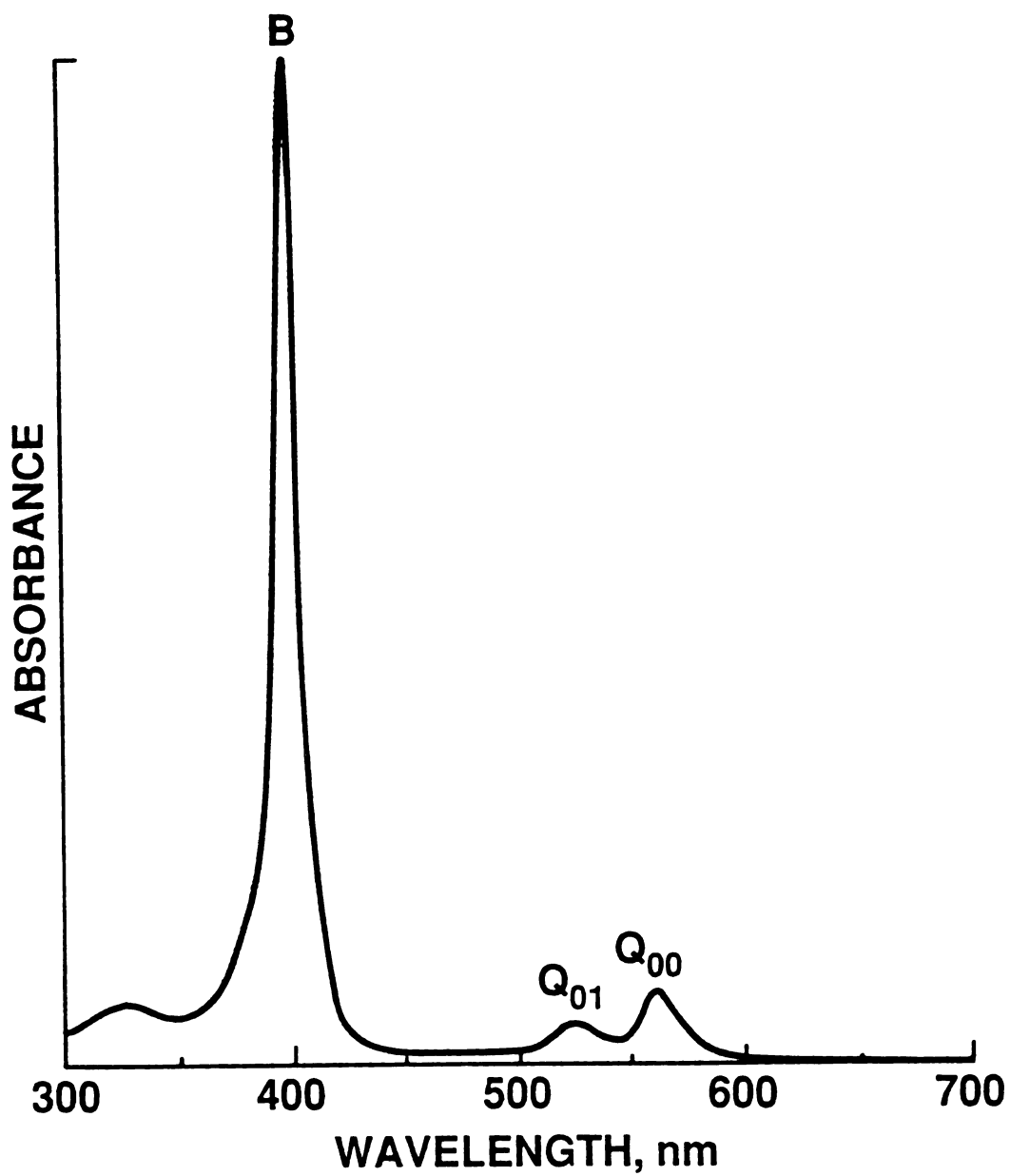


Figure 1.4 Electronic absorption spectrum of copper octaethylporphyrin (CuOEP) in  $\text{CH}_2\text{Cl}_2$  solution



transitions in the visible region are labelled the  $\alpha$  and  $\beta$  bands or  $Q_{00}$  and  $Q_{01}$ . The  $\beta$  band is a vibronic overtone of the  $\alpha$  band.

The theoretical interpretation of the electronic absorption spectra of metalloporphyrins is based on the four-orbital model of Gouterman (41,42). M.O. calculations (43) predict two HOMO's and two LUMO's as shown in Figure 1.5. Under  $D_{4h}$  symmetry the two HOMO's, labelled  $b_1$  and  $b_2$ , are of  $a_{2u}$  and  $a_{1u}$  symmetry, respectively. The  $a_{2u}$  orbital is calculated to be higher in energy than the  $a_{1u}$  orbital. The two LUMO's, labelled  $c_1$  and  $c_2$  are a degenerate pair of  $e_g$  symmetry. This M.O. treatment identifies the visible bands with the transition  $a_{2u} \rightarrow e_g$  and the Soret band with  $a_{1u} \rightarrow e_g$ . Because the transition dipoles are almost exactly equal the visible and Soret bands are predicted to be of equal intensity. In Gouterman's development of the four-orbital model, the  $a_{2u}$  and  $a_{1u}$  orbitals are assumed to be degenerate. The singly excited configurations ( $a_{2u}^1 e_g^1$ ) and ( $a_{1u}^1 e_g^1$ ) have the same symmetry and undergo configuration interaction to produce the excited states that correspond to the B and Q transitions. For the B state, the transition dipoles are additive hence the strong Soret absorption and in the Q state the transition dipoles subtract, leading to the weakly allowed visible bands.

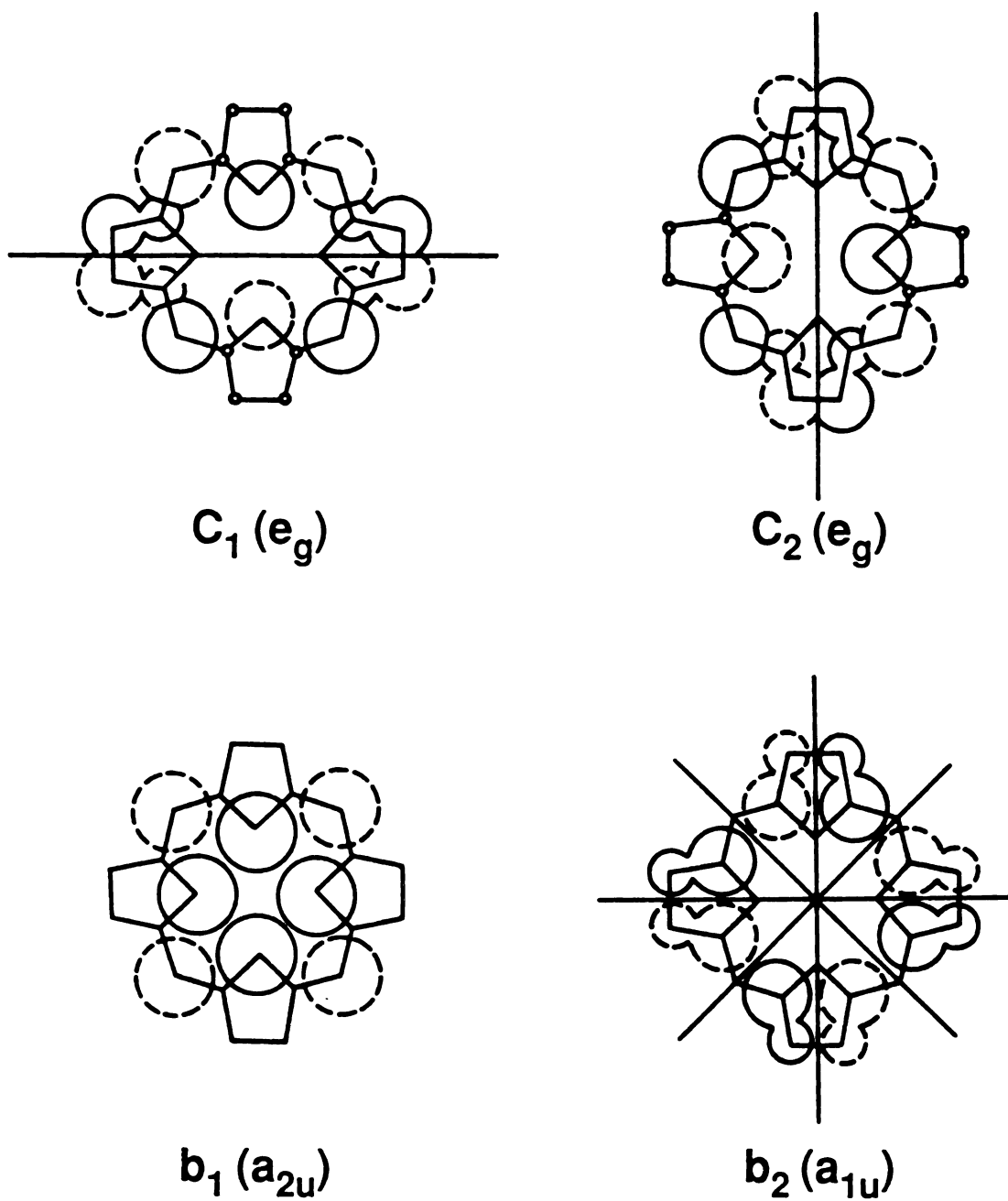


Figure 1.5 Porphyrin M.O.'s comprising the Gouterman four-orbital model (from ref. 42)

The nature of the central metal ion influences the energy and intensity of the B and Q transitions. The metal  $\pi$  orbital can conjugate with the  $\pi$  electron system of the porphyrin macrocycle. The  $a_{2u}$  orbital, with electron density on the pyrrole nitrogens, has the appropriate symmetry for such interaction, but the  $a_{1u}$  orbital does not. As the metal becomes more electropositive the energy of the  $a_{2u}$  orbital is raised. This results in a red-shift of the electronic absorption spectrum and, for alkyl-substituted porphyrins, a decrease in the relative intensity of the Q band compared to the Soret.

Reduction of a metalloporphyrin to a metallochlorin lowers the molecular symmetry from  $D_{4h}$  to  $C_2$ , taking into account  $S_1$  ruffling, where the x,y degeneracy has been removed. Configuration interaction produces four states, two of which comprising the Soret band are accidentally degenerate and strongly allowed (44). The other two states are  $Q_x$  and  $Q_y$ . The  $Q_y$  transition is at lower energy and is weakly allowed whereas the  $Q_x$  band is almost exactly forbidden. The  $Q_y$  band of a metallochlorin is stronger and red-shifted compared to the corresponding Q band in a metalloporphyrin. These effects are clearly seen in the electronic absorption spectrum of copper octaethylchlorin in  $CH_2Cl_2$  solution (Figure 1.6).

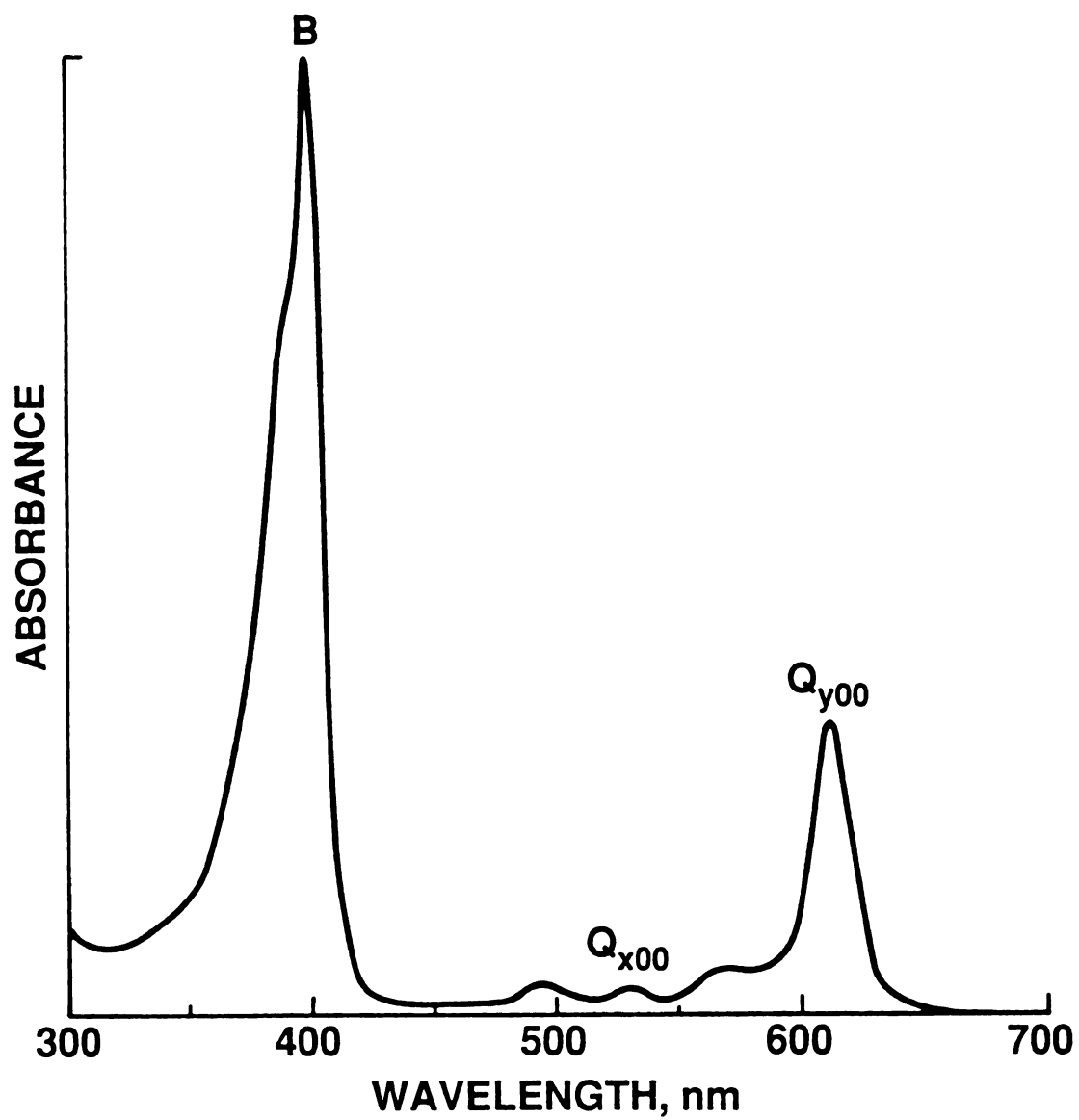


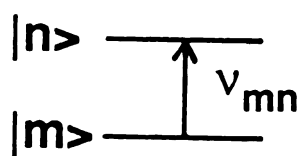
Figure 1.6 Electronic absorption spectrum of copper octaethylchlorin (CuOEC) in  $\text{CH}_2\text{Cl}_2$  solution

#### 4. Infrared and Raman Spectroscopy

Molecular vibrations fall into the frequency region between 100 and 4000  $\text{cm}^{-1}$ . Two techniques available for the characterization of the vibrational modes of a molecule are infrared (IR) and Raman spectroscopy. The molecular processes involved in these two methods are depicted in Figure 1.7 where  $|m\rangle$  and  $|n\rangle$  denote different quantum states of a vibrational mode in the ground electronic state of the molecule. The energy separation between the states  $|m\rangle$  and  $|n\rangle$  corresponds to the vibrational frequency  $\nu_{mn}$  of that particular vibrational mode. In IR spectroscopy, direct absorption of a quantum of frequency  $\nu_{mn}$  can promote the transition from state  $|m\rangle$  to  $|n\rangle$ . The vibrational mode is IR active if there is a change in the molecular dipole moment during the vibration.

When a beam of light impinges on a sample of molecules, some is absorbed, some is transmitted and some is scattered. Most of the scattered light is unchanged in frequency (Rayleigh scattering). In Raman scattering, incident light of frequency  $\nu_L$  is scattered by a molecule with a concomitant increase or decrease in frequency by an amount corresponding to the vibrational quantum  $\nu_{mn}$ . The process depicted in Figure 1.7(b) is referred to as Stokes (Raman) scattering because the transition from  $|m\rangle$  to  $|n\rangle$  results in a decrease in the frequency of the scattered light. The state  $|e\rangle$  in Figure 1.7(b) is a virtual state representing a sum over all excited

a) IR



b) Raman

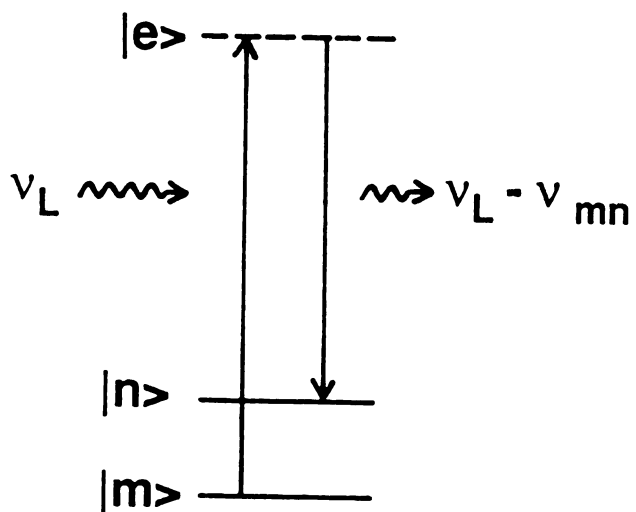


Figure 1.7 Molecular processes associated with a) Infrared and b) Raman spectroscopy (from ref. 45)

electronic states of the molecule. The Raman scattering event can be envisioned as two simultaneous transitions; absorption from  $|m\rangle$  to  $|e\rangle$  and emission from  $|e\rangle$  to  $|n\rangle$ . Anti-Stokes (Raman) scattering is associated with the transition  $|n\rangle$  to  $|m\rangle$  where the molecule has lost a vibrational quantum of energy and the scattered light has a higher frequency. At room temperature, most molecules are in the ground vibrational state so that Stokes scattering is more intense than anti-Stokes scattering. A vibrational mode is Raman active if there is a change in the molecular polarizability during the vibration.

The intensity of scattered radiation,  $I_{mn}$ , in photons per molecule per second for the Raman transition  $|m\rangle$  to  $|n\rangle$  is given by (45-48):

$$I_{mn} = \frac{128\pi^5}{9c^4} \nu_s^4 I_L \sum_{\rho\sigma} |(\alpha_{\rho\sigma})_{mn}|^2$$

where  $\nu_s$  is the frequency of the scattered radiation (for Stokes scattering,  $\nu_s = \nu_L - \nu_{mn}$ ),  $I_L$  is the intensity of the incident radiation in photons per second and  $(\alpha_{\rho\sigma})_{mn}$  is the  $\rho\sigma$ th component ( $\rho, \sigma = x, y, z$ ) of the polarizability tensor.

From second-order perturbation theory, the Kramers-Heisenberg dispersion formula shows the polarizability tensor to have the form:

$$(\alpha_{\rho\sigma})_{mn} = \frac{1}{h} \sum_e \frac{\langle n | \mu_\sigma | e \rangle \langle e | \mu_\rho | m \rangle}{\nu_{em} - \nu_L + i\Gamma_e} + \frac{\langle n | \mu_\sigma | e \rangle \langle e | \mu_\rho | m \rangle}{\nu_{em} + \nu_L + i\Gamma_e}$$

where  $|m\rangle$ ,  $|n\rangle$  and  $|e\rangle$  correspond to the states in Figure 1.7(b),  $\nu_{em}$  is the energy of the transition from  $|m\rangle$  to  $|e\rangle$ ,  $\mu_\sigma$  is the  $\sigma$ th component of the dipole moment operator and  $\Gamma_e$  is the homogeneous linewidth of the excited state  $|e\rangle$ . The summation is carried out over all excited states  $|e\rangle$  of the molecule. In this expression, the first part corresponds to a resonant term whereas the second part corresponds to a non-resonant term. As the incident laser frequency,  $\nu_L$  approaches the energy of an electronic transition,  $\nu_{em}$  the sum-over-states will be dominated by that single electronic state. The contribution of the first term to the scattering intensity increases as the energy separation  $|\nu_{em} - \nu_L|$  is minimized. This resonance condition results in an enormous enhancement of the intensity of Raman scattering compared to non-resonance (or normal) Raman scattering. The key, therefore, to a resonance Raman experiment is to match the frequency of the incident laser radiation to an electronic absorption band of the molecule under study. Vibrations associated with the chromophore of the molecule will be enhanced.



Resonance Raman spectroscopy is particularly suitable for the study of molecules of biological interest (49-51). Selective enhancement of the resonance Raman spectrum of a protein-bound chromophore is possible by excitation into an electronic absorption band of the chromophore. Additional advantages are that samples may be studied at low concentration and in aqueous solution.

IR and Raman spectroscopy can be used to determine the vibrational frequencies of a molecule in its ground electronic state. For a molecule with a center of symmetry, the selection rules prohibit the vibrational modes from being simultaneously IR and Raman active. The IR active modes are antisymmetric with respect to inversion but the Raman active modes are symmetric. The vibrational intensities are usually different in the IR and Raman spectra so that both techniques are required for full characterization of the vibrational modes of a molecule.

## 5. Vibrational Mode Assignments for Metalloporphyrins

Metalloporphyrins and hemoproteins have been studied widely by resonance Raman spectroscopy (45,52-54). The system of vibrational mode assignments for porphyrins currently in use is based on the normal coordinate analysis of NiOEP (55,56). The choice of NiOEP for the normal coordinate

analysis was made for several reasons: 1) the complex is stable and experimental data are available not only for NiOEP but also for its methine-deuterated (NiOEP-d<sub>4</sub>) (57-59) and <sup>15</sup>N-substituted (NiOEP-<sup>15</sup>N<sub>4</sub>) (59) derivatives; 2) the X-ray crystal structure of NiOEP is known (60); 3) the symmetrical structure of NiOEP simplifies the symmetry classification and assignment of the observed vibrational bands; and 4) the internal vibrations of the ethyl groups, which are not conjugated with the  $\pi$  electron system of the porphyrin macrocycle, do not appear in the resonance Raman spectra so that assignment of the porphyrin skeletal vibrations is made easier.

In the normal coordinate calculation of the in-plane vibrations, the structural parameters used are based on the X-ray crystal structure of the triclinic form of NiOEP (60), which have been slightly modified to maintain D<sub>4h</sub> symmetry. The peripheral ethyl group is treated as a point mass of 15 amu. In this model, the in-plane vibrations are factorized into 35 gerade (9A<sub>1g</sub> + 9B<sub>1g</sub> + 8A<sub>2g</sub> + 9B<sub>2g</sub>) resonance Raman active modes and 18 ungerade (E<sub>u</sub>) IR active modes. The A<sub>1g</sub> and A<sub>2g</sub> modes produce polarized (p) and anomalously polarized (ap) bands, respectively. The B<sub>1g</sub> and B<sub>2g</sub> modes produce depolarized (dp) bands. Table 1.1 lists the observed and calculated frequencies of NiOEP for modes in the region from 900 to 1700 cm<sup>-1</sup> (55). The observed resonance Raman frequencies are for NiOEP in CH<sub>2</sub>Cl<sub>2</sub> (59) solution. The frequencies of the E<sub>u</sub> modes are obtained from the IR spectrum of NiOEP in a CsI disk (58).

Table 1.1 Observed and calculated frequencies of NiOEP for modes in the region from 900 to 1700  $\text{cm}^{-1}$  (from ref. 55)

Symmetry	No.	Obs.	Calc.	Potential energy distribution (%)
$A_{1g}$	$\nu_2$	1602	1591	$\nu(C_bC_b)$ 60, $\nu(C_b-Et)$ 19
	$\nu_3$	1519	1517	$\nu(C_aC_m)$ 41, $\nu(C_aC_b)$ 35
	$\nu_4$	1383	1386	$\nu(C_aN)$ 53, $\delta(C_a-C_m)$ 21
	$\nu_5$	1025	1048	$\nu(C_b-Et)$ 38, $\nu(C_aC_b)$ 23
$B_{1g}$	$\nu_{10}$	1655	1656	$\nu(C_aC_m)$ 49, $\nu(C_aC_b)$ 17
	$\nu_{11}$	1576	1587	$\nu(C_bC_b)$ 57, $\nu(C_b-Et)$ 16
	$\nu_{12}$	1348*	1351	$\nu(C_aN)$ 63, $\nu(C_bC_b)$ 13
	$\nu_{13}$	1220	1262	$\delta(C_mH)$ 67, $\nu(C_aC_b)$ 22
	$\nu_{14}$	1151*	1095	$\nu(C_aC_b)$ 31, $\nu(C_b-Et)$ 30
$A_{2g}$	$\nu_{19}$	1603	1600	$\nu'(C_aC_m)$ 67, $\nu'(C_aC_b)$ 18
	$\nu_{20}$	1397	1409	$\nu'(C_aN)$ 29, $\nu'(C_b-Et)$ 24
	$\nu_{21}$	1308	1281	$\delta'(C_mH)$ 53, $\nu'(C_aC_b)$ 18
	$\nu_{22}$	1121	1118	$\nu'(C_aN)$ 37, $\nu'(C_b-Et)$ 26
	$\nu_{23}$	1022*	1022	$\nu'(C_aC_b)$ 26, $\nu'(C_b-Et)$ 20
$B_{2g}$	$\nu_{28}$	1475*	1469	$\nu'(C_aC_m)$ 52, $\nu'(C_aC_b)$ 21
	$\nu_{29}$	1409	1409	$\nu'(C_aC_b)$ 47, $\nu'(C_b-Et)$ 26
	$\nu_{30}$	1159	1157	$\nu'(C_b-Et)$ 49, $\nu'(C_aN)$ 28
	$\nu_{31}$	1019*	1016	$\delta'(C_a-C_m)$ 25, $\delta'(C_aC_mC_a)$ 23
$E_u$	$\nu_{37}$	1604	1634	$\nu(C_aC_m)$ 34, $\nu'(C_aC_m)$ 24
	$\nu_{38}$	1557	1588	$\nu(C_bC_b)$ 56, $\nu(C_b-Et)$ 16
	$\nu_{39}$	1487	1486	$\nu'(C_aC_m)$ 36, $\nu'(C_aC_b)$ 17
	$\nu_{40}$	1443	1411	$\nu'(C_aC_b)$ 30, $\nu'(C_b-Et)$ 24
	$\nu_{41}$	1389	1368	$\nu(C_aN)$ 56, $\delta(C_aC_m)$ 14
	$\nu_{42}$	1224	1275	$\delta(C_mH)$ 59, $\nu(C_aC_b)$ 9
	$\nu_{43}$	1127	1133	$\nu'(C_b-Et)$ 35, $\nu'(C_aN)$ 33
	$\nu_{44}$	1113	1080	$\nu(C_b-Et)$ 29, $\nu(C_aC_b)$ 26
	$\nu_{45}$	993	997	$\nu'(C_aC_m)$ 21, $\delta(C_aC_mC_a)$ 12

\* not observed as a fundamental

 $\nu$  = stretch,  $\delta$  = in-plane deformation

Assignments of the resonance Raman active modes are based on the observed polarization properties of the bands and support for the assignments comes from comparison with the isotopic frequency shifts for NiOEP-d<sub>4</sub> and NiOEP-<sup>15</sup>N<sub>4</sub>. The frequencies marked with an asterisk in Table 1.1 are not observed as fundamentals but are inferred from a study of the overtone and combination resonance Raman bands (59). The potential energy distribution (P.E.D.) represents the percentage contribution of a particular type of force constant to the total energy of the vibrational mode. For example, C<sub>b</sub>C<sub>b</sub> stretching is calculated to comprise 60% of the energy for the  $\nu_2$  vibrational mode. On the basis of the P.E.D., modes are classified as C<sub>b</sub>C<sub>b</sub> stretching modes ( $\nu_2$ ,  $\nu_{11}$ ), C<sub>a</sub>C<sub>m</sub> stretching modes ( $\nu_3$ ,  $\nu_{10}$ ,  $\nu_{19}$ ), C<sub>a</sub>N stretching modes ( $\nu_4$ ,  $\nu_{12}$ ), C<sub>m</sub>H bending modes ( $\nu_{13}$ ,  $\nu_{21}$ ), etc. (55). The vibrational motion is more complicated than the P.E.D. would suggest. A better representation of the vibrational mode is given by the Cartesian displacements of the atoms in the vibration. Figure 1.8 shows the form of the  $\nu_2$  vibrational mode.

With the vibrational mode assignments for NiOEP it is possible to interpret the resonance Raman data for other metalloporphyrins and hemoproteins. Prior to the normal coordinate analysis, Spaulding *et al.* (61) had noticed that the frequency of the anomalously polarized mode in metalloporphyrins corresponding to the 1603 cm<sup>-1</sup> mode of NiOEP in CH<sub>2</sub>Cl<sub>2</sub> solution (now identified as  $\nu_{19}$ ) exhibited an inverse

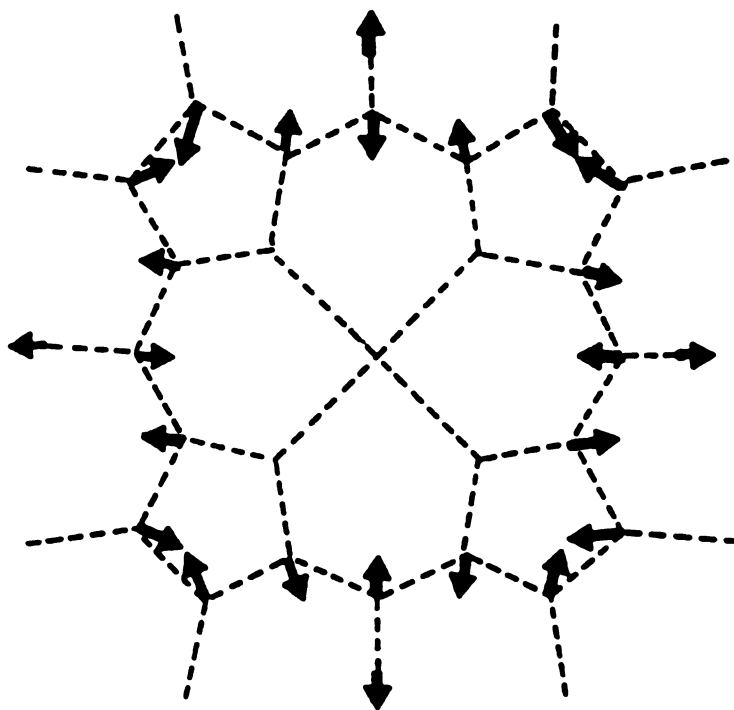


Figure 1.8 Atomic displacements in the  $\nu_2$  vibrational mode of NiOEP (from ref. 55)

linear correlation with the core-size of the metalloporphyrin. A similar correlation was observed for two modes labelled  $\nu_a$  and  $\nu_b$  of metallotetraphenylporphyrins by Huong and Pommier (62) who expressed the relationship between the vibrational frequency and core-size by the equation:

$$\nu = K ( A - d )$$

where  $\nu$  is the vibrational frequency in  $\text{cm}^{-1}$ ,  $d$  is the core-size of the metalloporphyrin in Å,  $A$  is the intercept and  $K$  is the slope. The vibrational modes of metalloporphyrins between 1450 and 1700  $\text{cm}^{-1}$  are collectively referred to as the core-size sensitive modes. The frequencies of the resonance Raman modes  $\nu_2$ ,  $\nu_3$ ,  $\nu_{10}$ ,  $\nu_{11}$  and  $\nu_{19}$  have been shown to exhibit a linear correlation with core-size (63-66). The slope or  $K$  value is proportional to the amount of  $\text{C}_a\text{C}_m$  stretching character in the P.E.D. of the vibrational mode. Expansion of the core produces a deformation of the  $\text{C}_a\text{C}_m\text{C}_a$  bond angles while the pyrrole rings maintain their structural integrity (67). Weakening of the  $\text{C}_a\text{C}_m$  bonds is reflected by a lowering of the vibrational frequency. Modes with  $\text{C}_a\text{C}_m$  stretching character ( $\nu_3$ ,  $\nu_{10}$  and  $\nu_{19}$ ) are more sensitive to core-size changes than are the  $\text{C}_b\text{C}_b$  stretching modes ( $\nu_2$  and  $\nu_{11}$ ). Determination of the core-size sensitivity thus provides a useful means of assigning vibrational modes in related metalloporphyrin systems.

## 6. The Application of Resonance Raman Spectroscopy to the Study of Chlorophyll

From the discussion of the role of chlorophyll in photosynthesis, it is apparent that plants have adapted a single type of chromophore (chlorophyll a) to serve distinctly different functions in the reaction center and antenna complexes. The spectral and redox properties of the chlorophylls are determined by the specific interaction with their protein environment. These interactions are possible through ligation of the central magnesium atom or through the peripheral substituents on the chlorophyll macrocycle. In principle, resonance Raman spectroscopy with its ability to probe the molecular structure of a chromophore within a protein environment provides an attractive means for the investigation of chlorophyll-protein interactions in vivo.

The application of resonance Raman spectroscopy to the study of chlorophylls in vitro and in the antenna complexes of higher plants has been pioneered by Lutz (68-76). The reaction center chlorophylls in higher plants are more difficult to study because of their low concentration relative to the antenna chlorophylls. Improvements in the biochemical procedures for the isolation of the reaction center protein complexes (77-79) offer promise that resonance Raman spectroscopy will be successful in establishing the structures of the reaction center chlorophylls (79).





## 7. Aim and Scope of this Work

In the work to be presented, three systems of increasing complexity from synthetic metallo-octaethylchlorins to chlorophylls to chlorophyll-binding proteins have been studied. As described in Chapter 3, resonance Raman and IR data on MOEC and selectively methine-deuterated CuOEC have been obtained to characterize the vibrational modes of metallochlorins. These results provide the basis for the interpretation of the resonance Raman spectra of metallochlorin  $\pi$  cation radicals (Chapter 4) and metallochlorophylls (Chapter 5). In turn, it is shown in Chapter 6 how the study of the isolated chlorophylls in solution can be used to understand the resonance Raman spectra of chlorophyll-binding proteins.

## CHAPTER 2

### MATERIALS AND METHODS

#### 1. Materials

##### i. Preparation of Chlorins

trans-H<sub>2</sub>OEC was prepared by the reduction of Fe<sup>III</sup>(OEP)Cl (Aldrich Chemical Company) with sodium metal in iso-amyl alcohol under nitrogen (80). Chromatography on alumina (Grade I) with benzene/ether (9:1, v/v) was used to eliminate residual H<sub>2</sub>OEP (81). CuOEC and ZnOEC were prepared from H<sub>2</sub>OEC by standard metal-insertion procedures (82). Chromatography on silica gel with benzene was used to remove any traces of unreacted H<sub>2</sub>OEC. NiOEC was prepared by refluxing nickel acetate with H<sub>2</sub>OEC in glacial acetic acid/CH<sub>2</sub>Cl<sub>2</sub> (5:1, v/v) under nitrogen (83). Chromatography on magnesium oxide with hexane/benzene (9:1, v/v) followed by chromatography on silica gel with benzene was used for purification.

Methine-deuterated H<sub>2</sub>OEC-d<sub>4</sub>, H<sub>2</sub>OEC- $\alpha,\beta$ -d<sub>2</sub>, and H<sub>2</sub>OEC- $\gamma,\delta$ -d<sub>2</sub> were prepared from H<sub>2</sub>OEC by Asaad Salehi (Michigan State University). H<sub>2</sub>OEC-d<sub>4</sub> was prepared by treatment of H<sub>2</sub>OEC with

$D_2SO_4/D_2O$  (9:1, v/v) (84). Reduction of the  $D_2SO_4/D_2O$  ratio to 6:1 (v/v) afforded  $H_2OEC-\gamma,\delta-d_2$  (85). Re-exchange at the  $\gamma$  and  $\delta$  positions of  $H_2OEC-d_4$  with  $H_2SO_4/H_2O$  (6:1, v/v) produced  $H_2OEC-\alpha,\beta-d_2$  (85). The proton NMR spectrum (A. Salehi, ref. 85) of trans- $H_2OEC$  shows two peaks at 9.7 and 8.9 ppm, corresponding to the  $\alpha,\beta$  and  $\gamma,\delta$  methine hydrogens, respectively. Deuteration at the  $\alpha,\beta$  methine positions is seen in the disappearance of the 9.7 ppm peak and at the  $\gamma,\delta$  methine positions by disappearance of the 8.9 ppm peak. In  $H_2OEC-d_4$ , both signals are completely absent. Deuterium substitution is quantitative for  $H_2OEC-d_4$  and  $H_2OEC-\gamma,\delta-d_2$ .  $H_2OEC-\alpha,\beta-d_2$  showed 90% deuteration at the  $\alpha,\beta$  positions and complete proton recovery at the  $\gamma,\delta$  positions.

Oxidation of  $CuOEC-\gamma,\delta-d_2$  with 2,3-dichloro-5,6-dicyanoquinone in benzene yielded  $CuOEP-d_2$  (86), which was purified by chromatography on silica gel with  $CH_2Cl_2$ .

## ii. Preparation of Chlorophyll a and b

Chlorophyll a and b were prepared from fresh spinach leaves according to the procedure of Omata and Murata (87). Chromatography on DEAE-Sephadex CL-6B (Pharmacia) with acetone removed carotenoids and pheophytins. Separation of chlorophyll a and b was achieved by chromatography on Sephadex CL-6B with hexane/2-propanol (20:1, v/v) to elute

chlorophyll a followed by hexane/2-propanol (10:1, v/v) to elute chlorophyll b. All operations were carried out under dim light in a cold box (10°C).

### iii. Preparation of Metal-Substituted Chlorophyll a

Chlorophylls were extracted from spinach leaves by treatment with acetone. Dioxane and water were added to precipitate the chlorophylls which were then collected by centrifugation (88). The crude chlorophyll extract was dissolved in ether and 1 N HCl added to convert the chlorophylls to pheophytins. The ether extract was washed with water, dried over  $\text{Na}_2\text{SO}_4$  and then evaporated. Pheophytin a was separated from pheophytin b by the use of the Girard 'T' reagent ((carboxymethyl)tri-methylammoniumchloridehydrazide) (89). Chromatography on alumina with  $\text{CH}_2\text{Cl}_2$  yielded pure pheophytin a free of carotenoids (as confirmed by TLC on alumina). Nickel, copper and zinc-substituted chlorophyll a were prepared from pheophytin a following the procedure of Boucher and Katz (90) by using the metal acetate in chloroform/acetic acid under nitrogen.

#### iv. Isolation of Chlorophyll-Binding Proteins

The light-harvesting chlorophyll a/b protein complex (LHC) was isolated from pea leaves by the procedure of Burke et al. (21). Thylakoid membranes with a chlorophyll concentration of 0.8 mg/ml were solubilized in 0.78% Triton X-100 and then fractionated on a 0.1 to 1.0 M sucrose gradient. The LHC fraction was identified as a deep red fluorescent band when illuminated from behind. This fraction was removed and aggregated by the addition of  $\text{MgCl}_2$  (to give a  $\text{Mg}^{2+}$  concentration of 7 mM) so that purified LHC could be collected by centrifugation. The chlorophyll a/b ratio and total chlorophyll concentration were determined by the procedure of Mackinney (91).

LHC, the 28 kDa chlorophyll a-binding protein and the LHC-depleted Photosystem II reaction center complex from spinach were isolated from Photosystem II membranes and supplied by Demetrios Ghanotakis (University of Michigan) (92).

## 2. Spectroscopic Techniques

### i. Electronic Absorption Spectroscopy

Electronic absorption spectra were recorded for solutions of metallochlorins, chlorophylls and chlorophyll-binding proteins on a Perkin Elmer Lambda 5 UV/vis spectrometer. Spectra were routinely recorded before and after Raman experiments to ensure that the laser beam had not induced decomposition of the sample.

### ii. Infrared Spectroscopy

Infrared spectra were recorded on a Perkin Elmer model 1750 FTIR spectrometer with  $2\text{ cm}^{-1}$  resolution. Spectra in  $\text{CCl}_4$  solution were obtained by using a 0.2 mm pathlength cell with KBr windows and the pure solvent as reference. Samples pressed into KBr discs were recorded with an air reference.

### iii. Resonance Raman Spectroscopy

Resonance Raman spectra were obtained on a computer-controlled Spex 1401 double monochromator equipped with a cooled RCA C31034 photomultiplier tube and photon-counting electronics (93). Data were collected at  $1\text{ cm}^{-1}$  intervals with

a 1 s dwell time and  $5 \text{ cm}^{-1}$  resolution. The measured Raman frequencies are accurate to  $\pm 1 \text{ cm}^{-1}$ . Laser powers employed are noted in the figure captions. Generally, the lowest power consistent with maintaining an acceptable signal to noise ratio was used. Excitation at 406.7 and 413.1 nm was provided by a Coherent model 90K krypton ion laser; at 441.6 nm by a Liconix model 4240 He-Cd laser; at 454.5, 457.9, 465.8, 472.7, 476.5, 488.0, 496.5, 501.7 and 514.5 nm by a Spectra Physics model 165 argon ion laser and at 615.0 nm from Rhodamine 590 in an argon ion pumped Spectra Physics model 375 dye laser.

Collection of the Raman scattered radiation was achieved with either a  $90^\circ$  scattering or  $180^\circ$  backscattering geometry. The  $90^\circ$  scattering geometry permits measurement of the depolarization ratio of the Raman bands. The depolarization ratio,  $\rho$  is defined as  $\rho = I_{\perp} / I_{\parallel}$ , where  $I_{\perp}$  and  $I_{\parallel}$  are the intensities of light scattered perpendicular and parallel, respectively, to the polarization of the incident laser beam. For polarized Raman bands,  $\rho < 3/4$ ; depolarized bands,  $\rho = 3/4$ ; and for anomalously polarized bands,  $\rho > 3/4$ . The measured depolarization ratios are accurate to  $\pm 0.1$ . Samples were contained in a spinning cylindrical quartz cell to avoid photodecomposition. As a rule, the concentration of the sample was adjusted to give an optical absorbance of 2.0 in a 0.5 mm pathlength cuvette at the excitation wavelength. The  $180^\circ$  backscattering geometry was used for concentrated samples. These could be de-gassed and sealed under argon in quartz EPR

tubes. This method was particularly suited to highly fluorescent compounds (eg. ZnOEC). Attachment of a low temperature Dewar enabled Raman spectra to be collected at temperatures down to  $-140^{\circ}\text{C}$  (93). Backscattering was also used for samples pressed into KBr discs. Figure 2.1 shows a diagram of the apparatus designed and built for use with KBr disc samples.



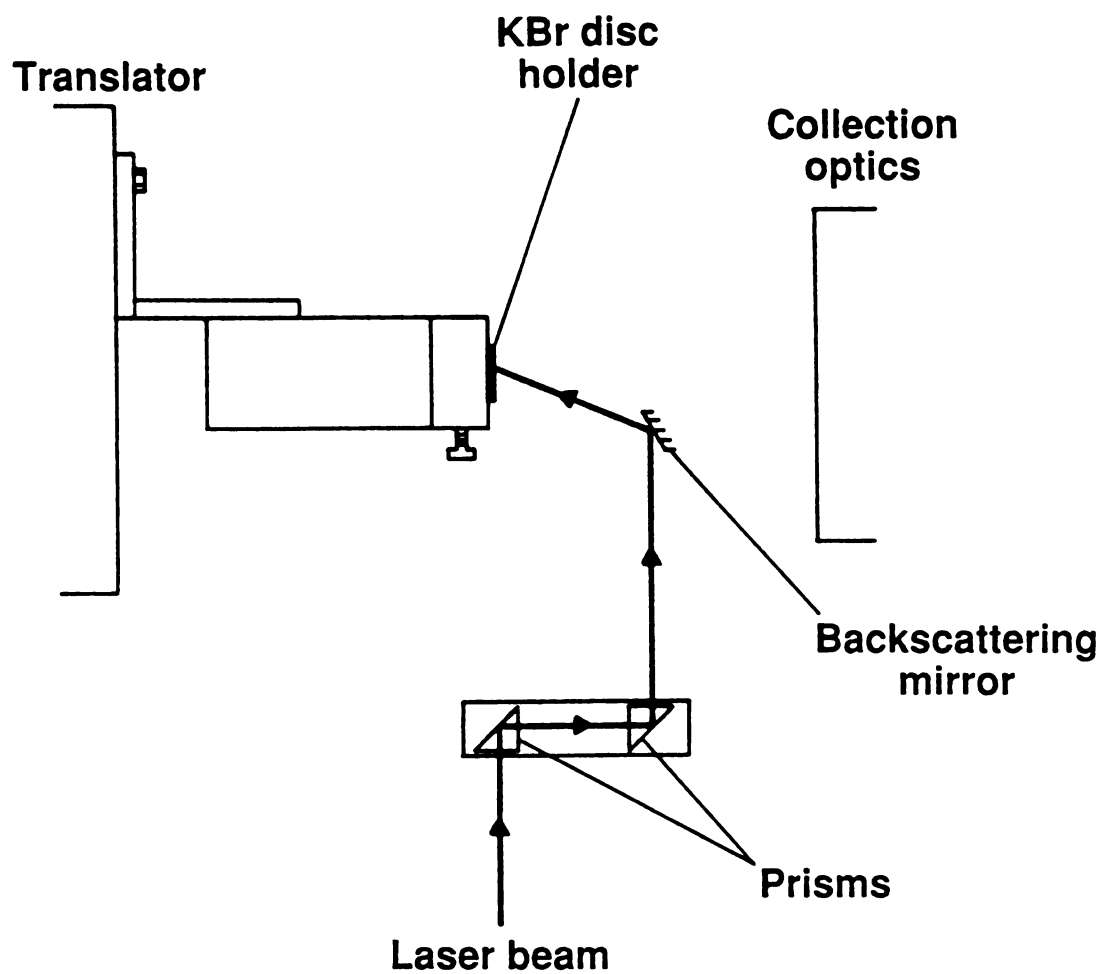


Figure 2.1 Diagram of the apparatus used for the collection of Raman spectra of KBr disc samples

## CHAPTER 3

### VIBRATIONAL PROPERTIES OF METALLOCHLORINS

#### 1. Introduction

The presence of a chlorin macrocycle is a characteristic structural feature of chlorophylls. Knowledge of the vibrational properties of simpler metallochlorin model compounds is essential to the successful interpretation of the more complex resonance Raman spectra of chlorophyll. Resonance Raman spectroscopic studies of metalloporphyrins and hemo-proteins (45,52-54) have benefitted greatly from the availability of a consistent set of vibrational mode assignments based on the normal coordinate analysis of NiOEP (55,56). In contrast, metallochlorins have received less attention and a consensus on their characteristic vibrational properties has yet to emerge.

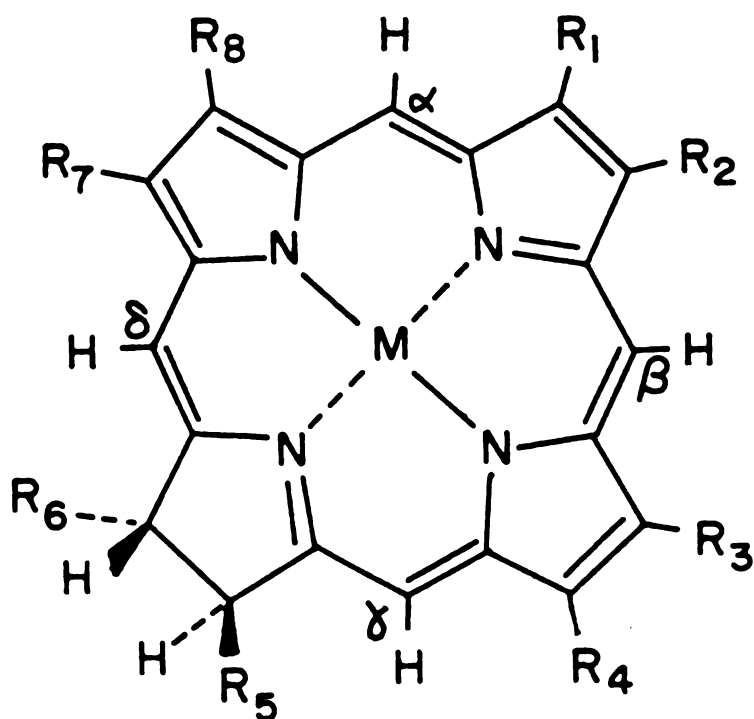
Metallo-octaethylchlorins (MOEC), (Figure 1.2(b)) with their highly symmetric structure are particularly suitable as metallochlorin model compounds. IR spectra of ZnOEC, CuOEC, NiOEC, Mg(OEC)py<sub>2</sub> (py = pyridine) and Fe<sup>III</sup>(OEC)X (where X = F, Cl, Br and I) were first reported by Ogoshi et al. (94) in

1975. The spectra were similar to those of the corresponding metallo-octaethylporphyrin (MOEP) complexes except for the appearance of new bands in the 1500 to 1700  $\text{cm}^{-1}$  region that were observed to be metal sensitive. Resonance Raman spectra of metallochlorins were reported in 1979 by Ozaki *et al.* (95) for CuOEC, CuOEC- $\gamma,\delta\text{-d}_2$ , CuOEC- $^{15}\text{N}_4$ , NiOEC,  $\text{Fe}^{\text{III}}(\text{OEC})\text{X}$  ( $\text{X} = \text{F}, \text{Cl}$ ) and  $\text{Fe}^{\text{III}}(\text{OEC})\text{Im}_2$  ( $\text{Im} = \text{imidazole}$ ) in  $\text{CH}_2\text{Cl}_2$  solution with  $\text{Q}_x$  excitation at 488.0 nm. Based on the isotopic frequency shifts for the CuOEC complexes, metallochlorin mode assignments were proposed for some the high frequency bands by direct comparison with NiOEP. These assignments were later extended to include low frequency modes from a study of iron OEC and OEP complexes in a variety of spin, oxidation and ligation states (66,96). Andersson and co-workers reported resonance Raman spectra of  $\text{Fe}^{\text{III}}\text{pPP}$  (pPP = photoproteoporphyrin IX dimethyl ester) and  $\text{Fe}^{\text{III}}\text{DC}$  (DC = deuteriochlorin IX dimethyl ester) with Soret,  $\text{Q}_x$  and  $\text{Q}_y$  excitation (97). Mode assignments were again proposed by comparison with the analogous iron protoporphyrin and deuteroporphyrin complexes.

As pointed out by Boldt *et al.* (83), such an approach assumes that the form of the normal modes are unchanged. In their resonance Raman study of NiOEC, which was supported by normal coordinate calculations, the latter authors concluded that the metallochlorin normal modes were substantially altered. A number of modes in the reduced ring macrocycle appear to be localized rather than delocalized over the whole

macrocycle as occurs in the case of metalloporphyrins. Support for their assignments came from comparison with the resonance Raman spectra of Cu diol chlorin- $d_4$  (diol chlorin = cis-3',4'-dihydroxy-2,4-dimethyl-deuterochlorin IX dimethyl ester) in KBr recorded by Andersson et al. (98).

In this Chapter, the IR and resonance Raman spectra of ZnOEC, CuOEC, NiOEC, CuECI (ECI = etiochlorin I) (Figure 3.1) and selectively methine-deuterated CuOEC complexes obtained with Soret,  $Q_x$  and  $Q_y$  excitation are presented. Both the IR and resonance Raman spectra are necessary to characterize fully the metallochlorin vibrational modes. By using the symmetric MOEC complexes the reliance on a single metal and the complications introduced by other peripheral substituents are avoided. Metal substitution with Zn, Cu and Ni covers a wide range of core-sizes without introducing the ligand, spin and oxidation-state effects associated with the Fe complexes. The amounts of  $C_aC_m$  and  $C_bC_b$  stretching character in the core-size sensitive modes are distinguished by the sensitivity of the vibrational frequency to metal substitution. Comparison of the spectra of CuOEC and CuECI identifies those modes with a contribution from  $C_bC_b$  and  $C_bC_s$  ( $s$  = substituent) stretching and  $C_bC_s$  bending coordinates as in the case with the analogous porphyrin species (99). The frequency shifts observed for CuOEC upon  $d_4$  as well as  $\alpha,\beta$ - $d_2$  and  $\gamma,\delta$ - $d_2$  methine deuteration confirm the mode assignments and permit an assessment of the extent of localization for a given mode. The results obtained



MOEC:  $R_1-R_8 = C_2H_5$      $M = Zn, Cu, Ni$

MECI:  $R_1, R_3, R_5, R_7 = CH_3$      $M = Cu$

$R_2, R_4, R_6, R_8 = C_2H_5$

Figure 3.1 Structure and labelling scheme for metallochlorin model compounds. MOEC = trans-metallo-octaethylchlorin and MECI = trans-metallo-etiochlorin I

support the concept of mode localization introduced by Boldt et al. although the mode composition for several prominent modes differs from that deduced in their analysis.

## 2. Results

### i. Electronic Absorption Spectra

Figure 3.2 shows the electronic absorption spectra of ZnOEC, CuOEC and NiOEC in benzene solution. The spectra display the characteristic features of metallochlorins namely, separate  $Q_x$  and  $Q_y$  transitions with the peak absorbance of the  $Q_{y00}$  band about half that of the Soret absorption band. The absorption maxima are listed in Table 3.1 together with the ratio of the  $Q_{y00}$  to Soret oscillator strength,  $r$  for each complex. The oscillator strength ratios were determined by measuring the areas under the Soret and  $Q_{y00}$  bands for the absorption spectra plotted on a wavenumber scale. The energies of the Soret and  $Q_x$  transitions follow the order  $Ni > Cu > Zn$ . Also, the ratio of the  $Q_{y00}$  to Soret oscillator strength decreases from Ni to Cu to Zn.

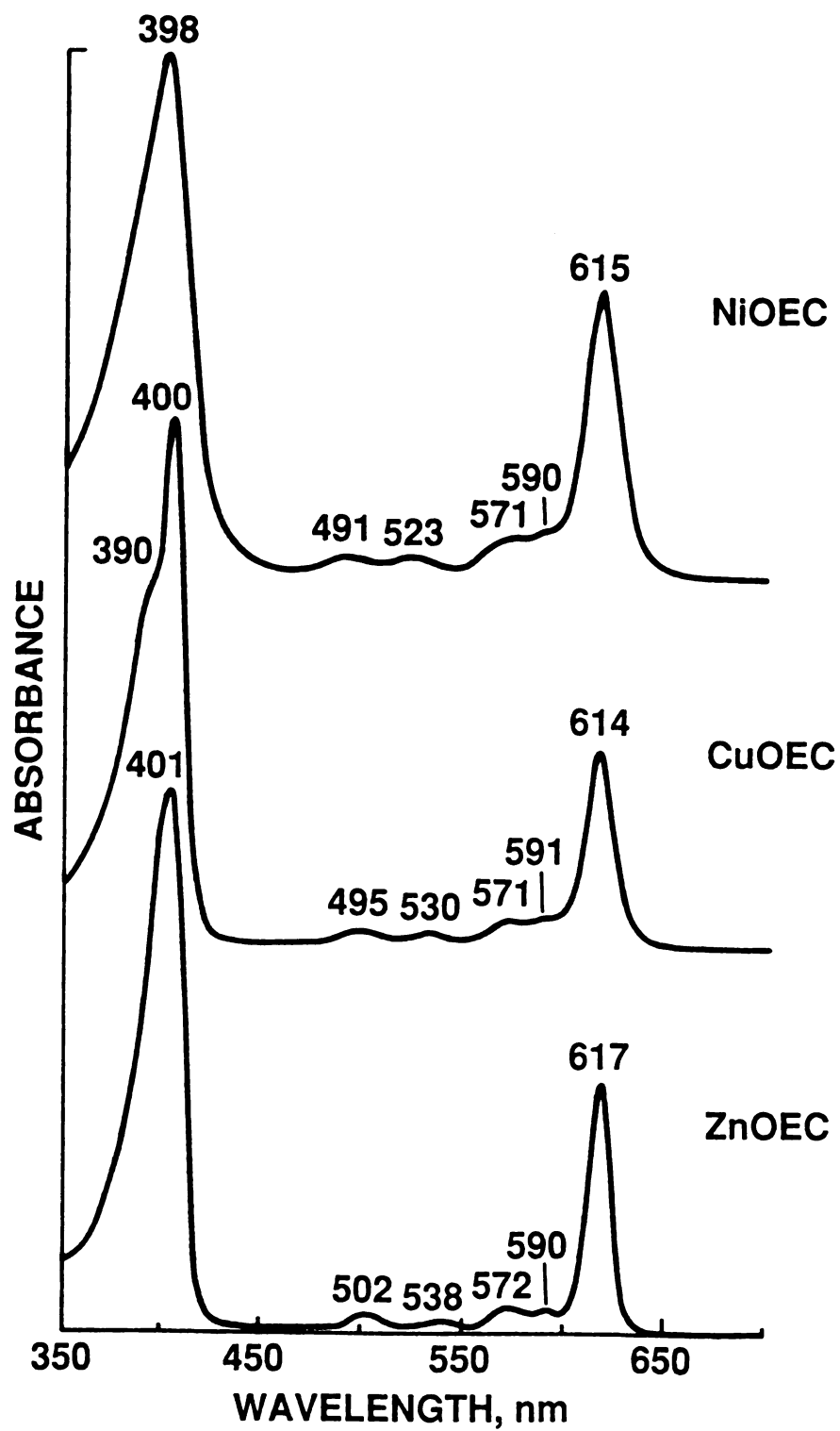


Figure 3.2 Electronic absorption spectra of ZnOEC, CuOEC and NiOEC in benzene solution

Table 3.1 Electronic absorption maxima (nm) for MOEC complexes in benzene solution

	Soret	Q <sub>x01</sub>	Q <sub>x00</sub>	Q <sub>y02</sub>	Q <sub>y01</sub>	Q <sub>y00</sub>	r
ZnOEC	401	502	538	572	590	617	0.08
CuOEC	400	495	530	571	591	614	0.09
NiOEC	398	491	523	571	590	615	0.13

$$r = f_{Q_{y00}}/f_{Soret}$$

These observations are in accord with the Gouterman four-orbital model (41,42). For alkyl-substituted complexes the  $a_{2u}$  orbital is lower in energy than the  $a_{1u}$  orbital. As the metal becomes more electropositive, the energy of the  $a_{2u}$  orbital is raised relative to the  $a_{1u}$  orbital. This effect is manifested in the electronic absorption spectrum as a red-shift of the Soret and Q bands and a decrease in the ratio of the  $Q_{00}$  to Soret oscillator strength. Table 3.2 summarizes electronic absorption spectral data for MOEP complexes in benzene solution. The Soret and Q bands red-shift and the oscillator strength ratio decreases in the order  $Ni > Cu > Zn$ . The oscillator strength ratios for the MOEC complexes are larger than the respective MOEP complexes reflecting the allowed nature of the  $Q_{y00}$  transition in metallochlorins.



Table 3.2 Electronic absorption maxima (nm) for MOEP complexes in benzene solution

	Soret	Q <sub>01</sub>	Q <sub>00</sub>	r
ZnOEP	404	533	569	0.04
CuOEP	400	527	563	0.05
NiOEP	393	518	552	0.07

$$r = f_{Q00}/f_{Soret}$$

#### ii. Resonance Raman Spectra of MOEC

The resonance Raman spectra of ZnOEC, CuOEC and NiOEC in CH<sub>2</sub>Cl<sub>2</sub> solution obtained with Soret excitation at 406.7 nm are shown in Figure 3.3. The vibrational frequencies for these species and the depolarization ratios for CuOEC are listed in Table 3.3. Five modes in the frequency region from 1490 to 1700 cm<sup>-1</sup> corresponding to the 1644, 1602, 1584, 1545 and 1507 cm<sup>-1</sup> modes of CuOEC are observed to be metal dependent. Inspection of the polarized resonance Raman spectra of CuOEC at 406.7 nm (not shown) reveals that the 1545 cm<sup>-1</sup> band consists of a 1547 cm<sup>-1</sup> polarized mode and a 1543 cm<sup>-1</sup> anomalously polarized mode.

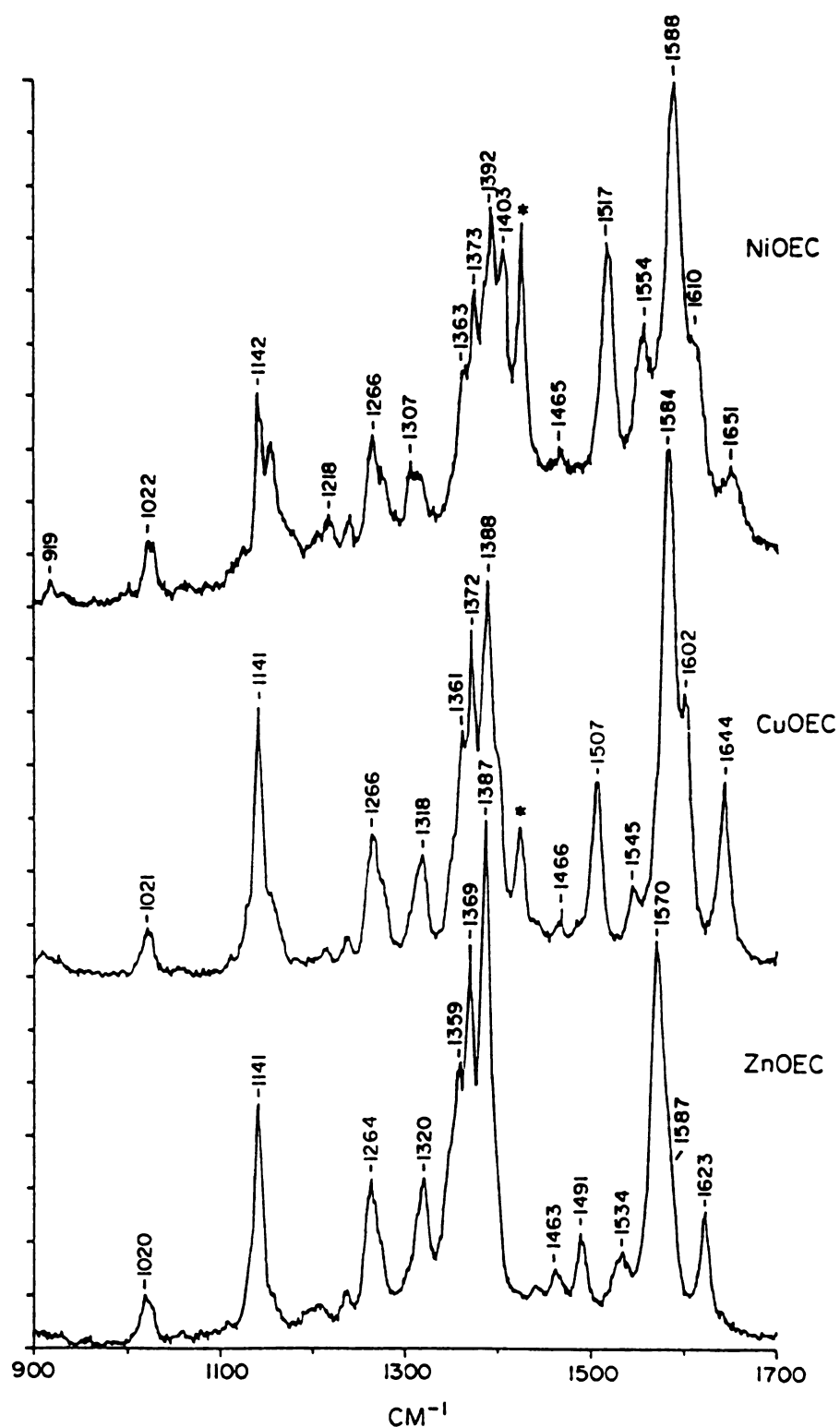


Figure 3.3 Resonance Raman spectra of ZnOEC, CuOEC and NiOEC in  $\text{CH}_2\text{Cl}_2$  solution obtained with Soret excitation at 406.7 nm. Laser powers: 5, 7 and 20 mW, respectively

Table 3.3 Vibrational frequencies ( $\text{cm}^{-1}$ ) and Raman depolarization ratios of MOEC

NiOEC				CuOEC				ZnOEC		
406.7	488.0	615.0	IR	406.7	$\rho$	488.0	$\rho$	615.0	$\rho$	IR
--	--	--	1740	--		--		--		1741
--	--	--	1712	--		--		--		1708
1651	1652	1652	1652	1644	0.8dp	1643	0.5p	1644	0.4p	1644
1610	1613	1613	1611	1602	0.6p	1601	1.0ap	1602	0.5p	1602
1588	1592	1589	1591	1584	0.4p	1584	0.7dp	1583	0.7dp	1584
1554	1554	1554	1553	1547	0.3p	1546	0.6p	1548	0.4p	1547
--	--	--	--	1543	1.6ap	--		--		1543
1517	1517	1517	--	1507	0.2p	1506	0.3p	1507	0.4p	1504
--	--	1502	1499	--		--		1486	0.3p	1484
--	1483	--	--	--		--		--		--
1465	1466	1466	1464	1466	0.7dp	1465	1.0ap	1465	0.5p	1464
--	--	--	1457	--		--		--		--
--	--	--	1453	--		--		--		1452
--	--	--	--	--		--		--		1443
1403	1404	1401	--	1399	0.6p	1402	0.7dp	1401	0.5p	--
--	--	--	1397	--		--		--		1396
1392	--	--	--	1388	0.3p	1391		1392	0.4p	--
--	1383	--	--	--		--		--		1384
--	--	--	1378	--		--		--		1375
1373	1373	1372	--	1372	0.3p	1372	0.3p	1373	0.3p	--
1363	1363	--	1365	1361	0.3p	1361	0.3p	--		--

Table 3.3 (cont'd.)

NiOEC				CuOEC				ZnOEC				
406.7	488.0	615.0	IR	406.7	$\rho$	488.0	$\rho$	615.0	$\rho$	IR	406.7	IR
1349	1351	--	--	1352	0.2p	1350	0.3p	--	--	--	1349	--
1316	--	--	1315	1318	0.6p	1318	1.4ap	1318	0.7dp	1318	1320	1320
1307	1306	1308	--	--	--	--	--	1310	0.6p	--	--	--
--	--	--	1303	--	--	--	--	--	--	1301	--	1301
1275	1275	1276	1274	1276	0.3p	1275	0.7dp	1277	0.4p	1273	1275	1272
1266	1264	1266	1269	1266	0.3p	1265	0.8dp	1267	--	1262	1264	1266
1241	--	1239	--	1238	0.4p	--	--	1238	0.4p	--	1237	--
--	--	--	1233	--	--	--	--	--	--	1235	--	1235
1218	1219	1219	1217	1216	0.6p	1212	0.6p	1215	0.4p	1211	1207	1205
1204	1202	1202	1200	--	--	1199	0.3p	1198	0.3p	1197	1198	1194
--	1180	--	1180	--	--	1182	0.5p	--	--	1183	--	1183
1154*	1154*	--	--	1155*	--	1157*	--	1154*	--	--	1158	--
--	--	--	1144	--	--	--	--	--	--	1146	--	1147
1142	--	1140	--	1141	0.3p	--	--	1141	0.4p	--	1141	--
1125	1123	1124	1123	1129	--	1128	0.5p	1128	0.5p	1128	--	1132
--	--	--	--	--	--	--	--	--	--	1119	--	1118
--	--	--	--	--	--	--	--	--	--	--	--	1111
--	--	--	1109	--	--	--	--	--	--	1107	--	1106
--	--	--	1094	--	--	--	--	--	--	1095	--	1094
--	--	--	1084	--	--	--	--	--	--	1086	--	--
--	--	--	1063	--	--	--	--	--	--	1064	--	1063

Table 3.3 (cont'd.)

NiOEC				CuOEC				ZnOEC	
406.7	488.0	615.0	IR	406.7	$\rho$	488.0	$\rho$	615.0	IR
--	1059	--	1058	--	--	--	--	--	1058
1028	1027	--	--	1026	0.3p	1206	0.3p	--	1025
1022	1022	1020	--	1021	0.5p	1020	0.4p	1021	0.4p
--	--	--	1014	--	--	--	--	1015	--
--	--	994	996	--	--	--	--	988	--
--	960	961	--	--	--	960	--	961	0.4p
--	--	--	957	--	--	--	--	956	--
932	932	--	932	--	--	932	--	932	--
919	921	922	921	--	--	--	--	923	--
--	--	--	--	909	0.3p	--	--	--	--

406.7, 488.0 and 615.0 refer to laser wavelengths (nm) used for Soret,  $Q_x$  and  $Q_y$  excitation, respectively.

$\rho$  = depolarization ratio; p = polarized, dp = depolarized, ap = anomalously polarized.

\* overlapped by  $\text{CH}_2\text{Cl}_2$  solvent band

Resonance Raman spectra of CuOEC (Figure 3.4) and NiOEC (Figure 3.5) in  $\text{CH}_2\text{Cl}_2$  solution were obtained with  $Q_x$  excitation at 488.0 nm and with  $Q_y$  excitation at 615.0 nm. The intense fluorescence of ZnOEC prohibited the measurement of its resonance Raman spectra with visible excitation. The frequencies are listed in Table 3.3 along with the depolarization ratios for CuOEC. The 488.0 nm excitation spectra agree with those reported by Ozaki *et al.* (95). For CuOEC, bands that are not seen with Soret excitation are observed at 1199, 960 and 932  $\text{cm}^{-1}$  with  $Q_x$  and  $Q_y$  excitation; at 1182  $\text{cm}^{-1}$  with  $Q_x$  excitation only; and at 1486, 1310 and 923  $\text{cm}^{-1}$  with  $Q_y$  excitation only. The 1486  $\text{cm}^{-1}$  band of CuOEC is metal sensitive, corresponding to the 1502  $\text{cm}^{-1}$  band of NiOEC observed with  $Q_y$  excitation.

### iii. IR Spectra of MOEC

For a metallochlorin of  $C_2$  symmetry, the resonance Raman active modes are also IR active. The IR spectra of ZnOEC, CuOEC and NiOEC in  $\text{CCl}_4$  solution are shown in Figure 3.6 and the vibrational frequencies are listed in Table 3.3. The total number of bands observed by IR spectroscopy is greater than with resonance Raman spectroscopy as a result of IR activity of the internal vibrations of the ethyl groups. These modes can be identified by comparison with the IR spectrum of NiOEP reported by Kincaid *et al.* (100). The two closely spaced modes

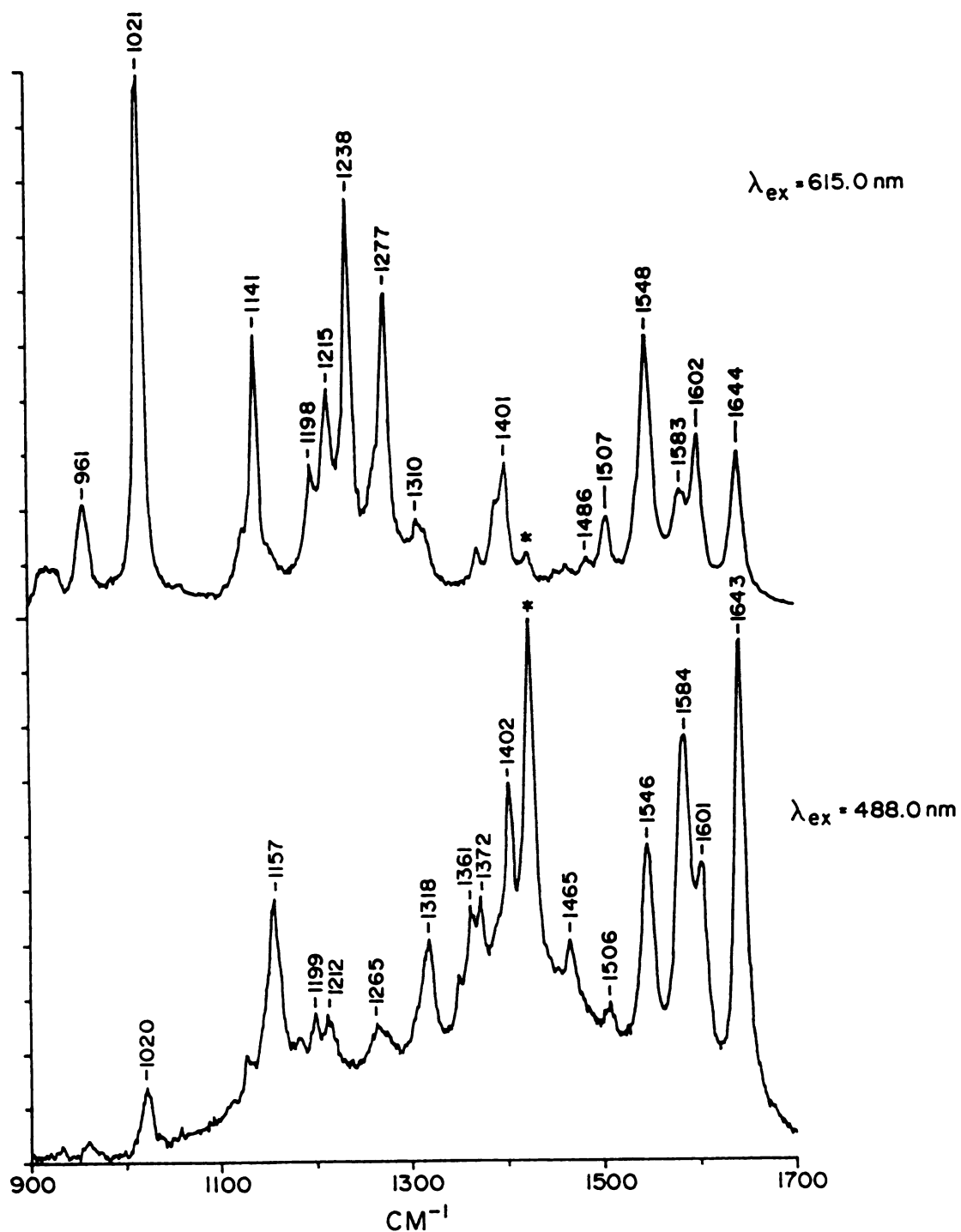


Figure 3.4 Resonance Raman spectra of CuOEC in  $\text{CH}_2\text{Cl}_2$  solution obtained with  $Q_x$  excitation at 488.0 nm and  $Q_y$  excitation at 615.0 nm. Laser powers: 100 and 35 mW, respectively

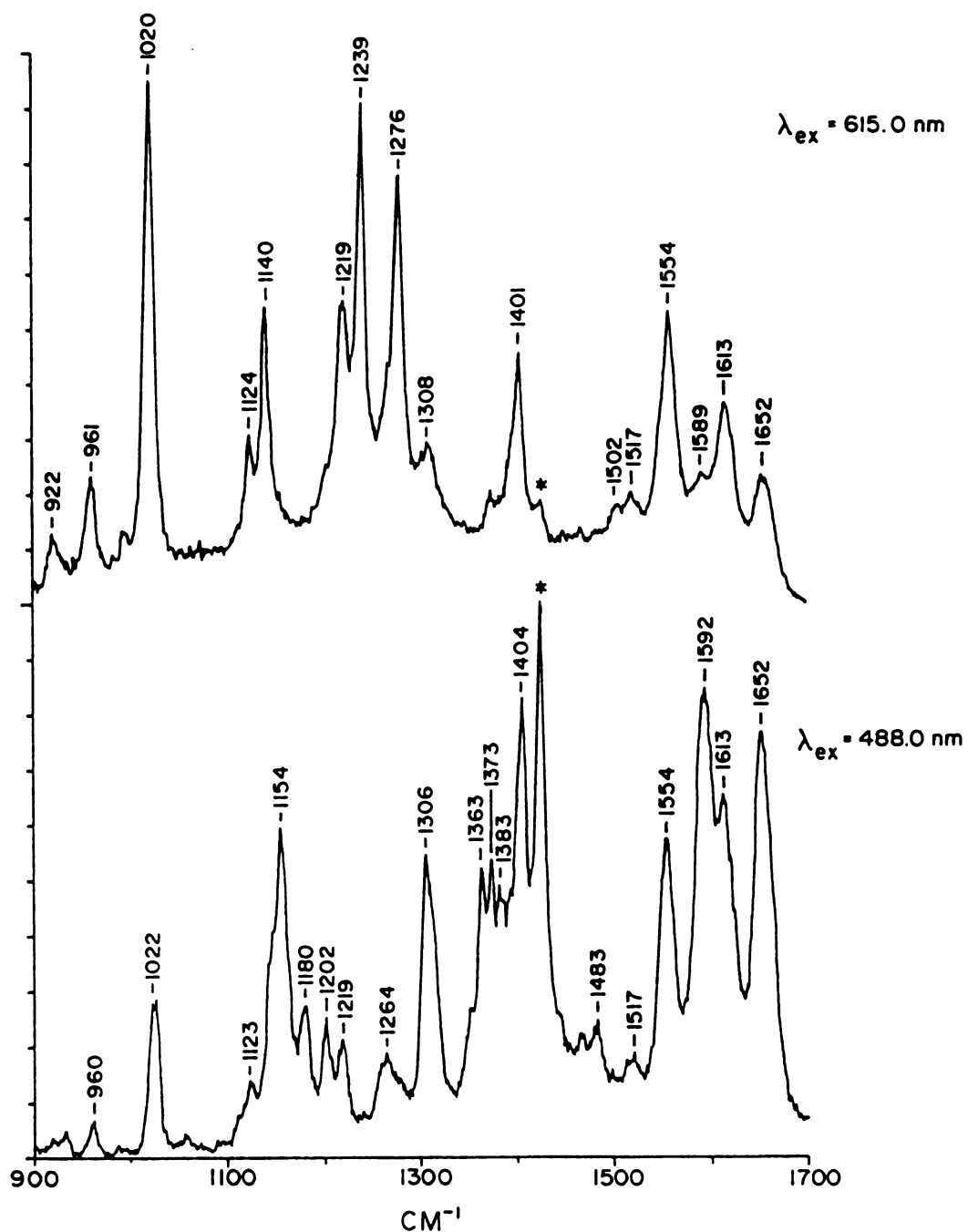


Figure 3.5 Resonance Raman spectra of NiOEC in  $\text{CH}_2\text{Cl}_2$  solution obtained with  $Q_x$  excitation at 488.0 nm and  $Q_y$  excitation at 615.0 nm. Laser powers: 70 and 40 mW, respectively



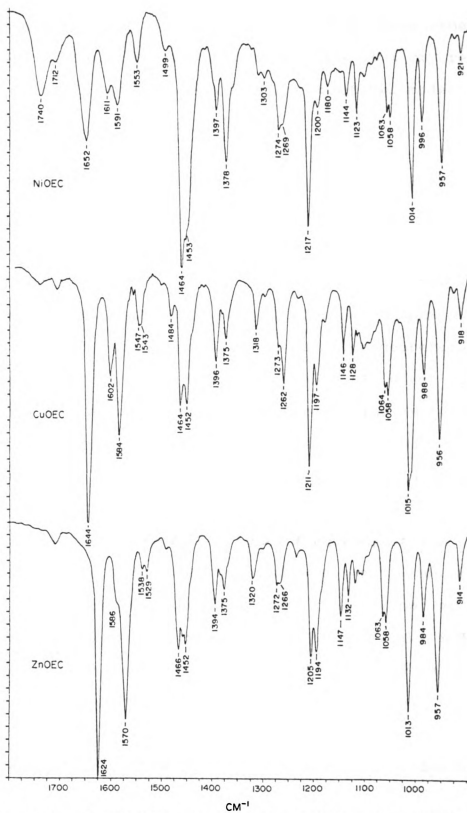


Figure 3.6 IR spectra of ZnOEC, CuOEC and NiOEC in  $\text{CCl}_4$  solution

at 1547 and 1543  $\text{cm}^{-1}$  of CuOEC that can be resolved in the Raman spectrum by depolarization ratio measurement are apparent in the IR spectrum; similarly the 1534  $\text{cm}^{-1}$  resonance Raman mode of ZnOEC is seen to consist of two modes at 1538 and 1529  $\text{cm}^{-1}$ .

#### iv. Effects of Methine Deuteration

Figure 3.7 shows the IR spectra of CuOEC- $\gamma,\delta\text{-d}_2$ , CuOEC- $\alpha,\beta\text{-d}_2$  and CuOEC- $\text{d}_4$  in  $\text{CCl}_4$  solution and Figure 3.8 shows the resonance Raman spectra of the methine-deuterated CuOEC complexes obtained with  $Q_y$  excitation at 615.0 nm. Different patterns of frequency shifts are observed for deuteration at the  $\gamma,\delta$  and  $\alpha,\beta$  positions. The 1644, 1602, 1584, 1507 and 1486  $\text{cm}^{-1}$  modes of CuOEC exhibit frequency shifts upon both  $\alpha,\beta$  and  $\gamma,\delta$  deuteration that are additive for CuOEC- $\text{d}_4$ . Only the 1584 and 1507  $\text{cm}^{-1}$  modes show equal frequency shifts upon  $\alpha,\beta$  and  $\gamma,\delta$  deuteration. The 1644 and 1486  $\text{cm}^{-1}$  modes are more sensitive to  $\gamma,\delta$  deuteration whereas the 1602  $\text{cm}^{-1}$  mode shows a large shift upon  $\alpha,\beta$  deuteration. The 1543  $\text{cm}^{-1}$  mode shows no shift upon  $\alpha,\beta$  deuteration but a shift of -17  $\text{cm}^{-1}$  upon  $\gamma,\delta$  and  $\text{d}_4$  methine deuteration.

Below 1350  $\text{cm}^{-1}$ , many of the vibrational modes of CuOEC are sensitive to methine deuteration. However, the complicated pattern of frequency shifts observed for CuOEC- $\alpha,\beta\text{-d}_2$ ,

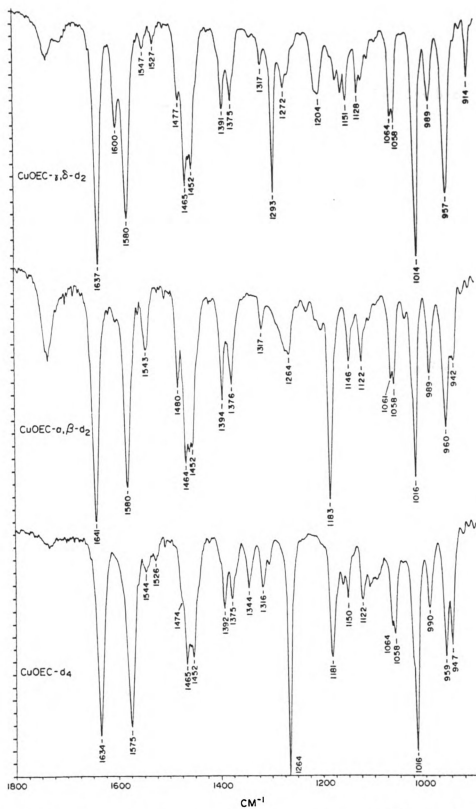


Figure 3.7 IR spectra of CuOEC- $\gamma,\delta\text{-d}_2$ , CuOEC- $\alpha,\beta\text{-d}_2$  and CuOEC- $\text{d}_4$  in  $\text{CCl}_4$  solution

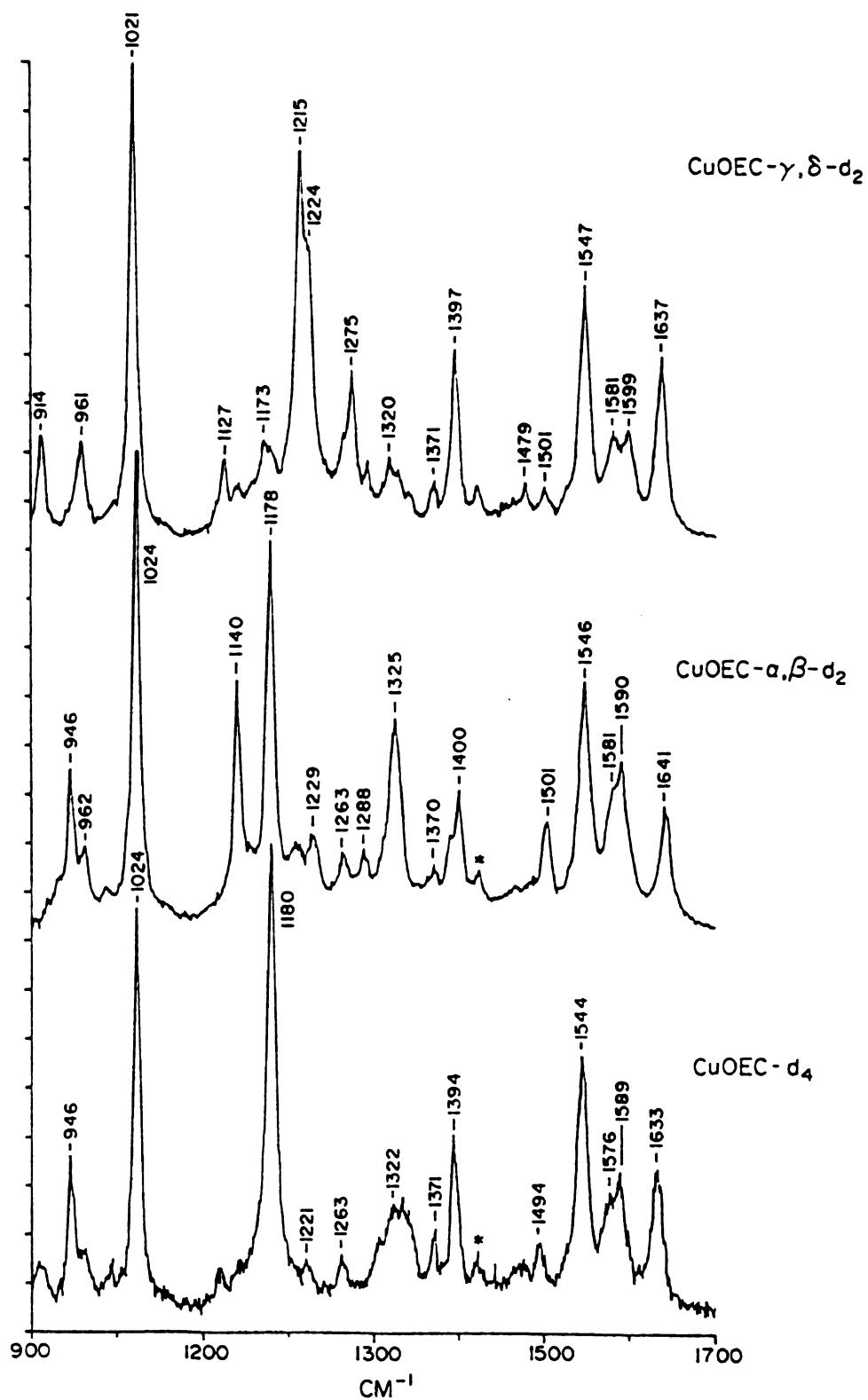


Figure 3.8 Resonance Raman spectra of CuOEC- $\gamma,\delta\text{-d}_2$ , CuOEC- $\alpha,\beta\text{-d}_2$  and CuOEC- $\text{d}_4$  in  $\text{CH}_2\text{Cl}_2$  solution obtained with  $Q_y$  excitation at 615.0 nm. Laser power: 40 mW

CuOEC- $\gamma,\delta$ -d<sub>2</sub> and CuOEC-d<sub>4</sub> does not permit a one-to-one correlation of these modes in the various CuOEC complexes. Nevertheless, it is possible to recognize several modes that clearly show  $\alpha,\beta$  or  $\gamma,\delta$  localization in this frequency region.

In order to interpret the frequency shifts for the methine-deuterated copper chlorin complexes, two methine-deuterated copper porphyrin compounds were prepared. In the CuOEP-d<sub>4</sub> species, all four methine carbons are deuterated; in the CuOEP-d<sub>2</sub> complex, only two of the four bridging carbons are deuterium substituted at adjacent methine positions. These compounds allow assessment of the effect of full and partial deuteration on modes that are delocalized throughout the macrocycle. Resonance Raman spectra of CuOEP, CuOEP-d<sub>2</sub> and CuOEP-d<sub>4</sub> were recorded with Soret excitation at 406.7 nm (Figure 3.9) and with visible excitation at 514.5 nm (Figure 3.10). The C<sub>a</sub>C<sub>m</sub> stretching modes  $\nu_{10}$ ,  $\nu_{19}$  and  $\nu_3$  of CuOEP show frequency shifts of -13, -22 and -10 cm<sup>-1</sup> in CuOEP-d<sub>4</sub>. For CuOEP-d<sub>2</sub>, the frequency shifts of the  $\nu_{10}$  and  $\nu_3$  modes are half of those observed for CuOEP-d<sub>4</sub>. The  $\nu_{19}$  mode shows a -14 cm<sup>-1</sup> shift for CuOEP-d<sub>2</sub> but only a further -8 cm<sup>-1</sup> shift for CuOEP-d<sub>4</sub>. The frequencies of the C<sub>b</sub>C<sub>b</sub> stretching modes  $\nu_2$  and  $\nu_{11}$  are not shifted upon d<sub>2</sub> or d<sub>4</sub> methine deuteration (101). The results for the  $\nu_{10}$  and  $\nu_3$  modes indicate that the vibrational mode is delocalized over the porphyrin macrocycle and that the mode composition is not altered by methine deuteration. The  $\nu_{19}$  mode, although delocalized, is mixed with

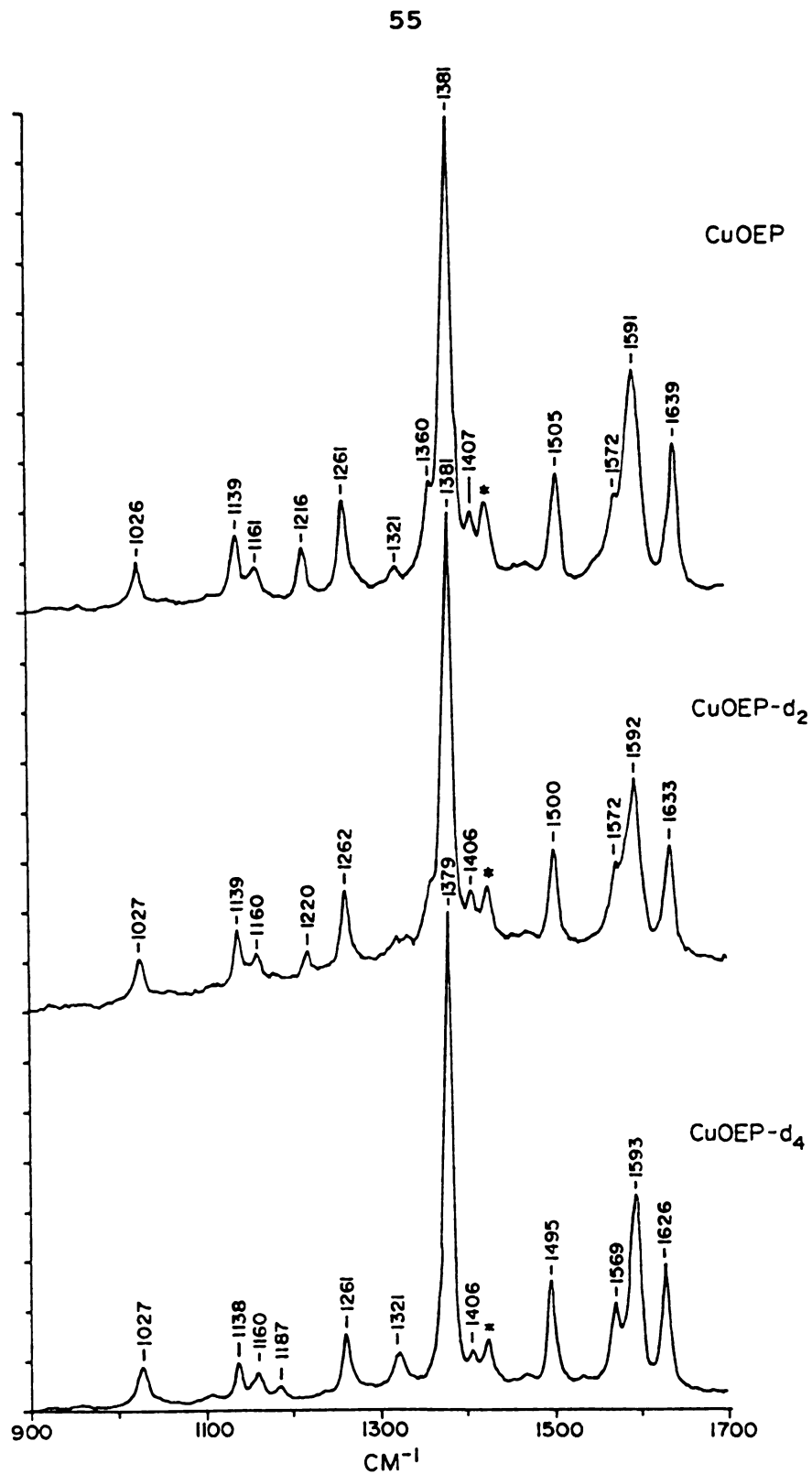


Figure 3.9 Resonance Raman spectra of CuOEP, CuOEP-d<sub>2</sub> and CuOEP-d<sub>4</sub> in CH<sub>2</sub>Cl<sub>2</sub> solution obtained with Soret excitation at 406.7 nm. Laser power: 10 mW

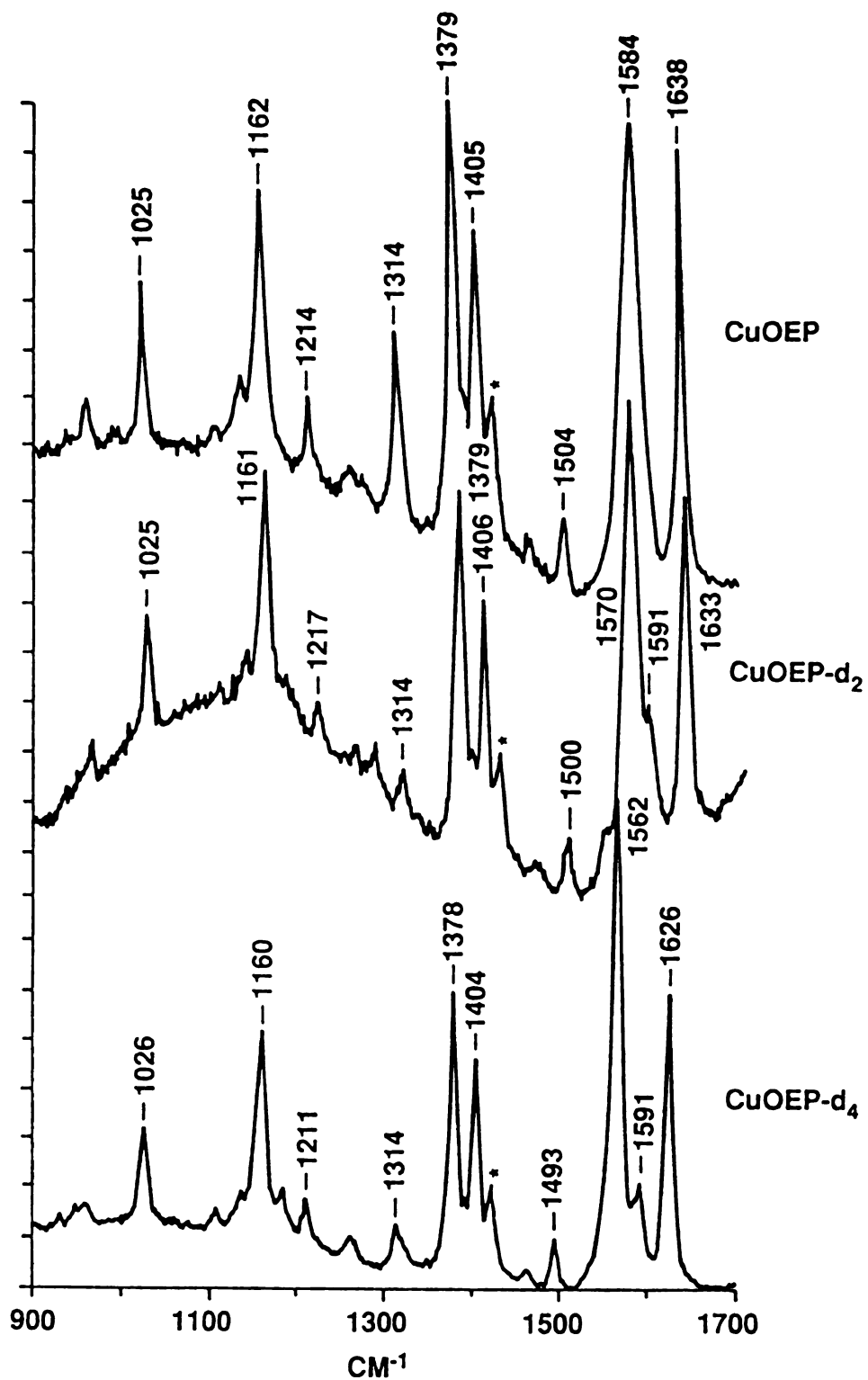


Figure 3.10 Resonance Raman spectra of CuOEP, CuOEP-d<sub>2</sub> and CuOEP-d<sub>4</sub> in CH<sub>2</sub>Cl<sub>2</sub> solution obtained with visible excitation at 514.5 nm. Laser power: 50 mW

$C_mH$  bending character (56) and most likely changes in mode composition upon deuteration. Taken together, these results for partially and fully methine-deuterated metallo-octaethylporphyrins provide a basis for the analysis of the corresponding metallo-octaethylchlorin complexes. Most importantly, they show that for a delocalized mode, methine  $d_2$  deuteration can be expected to produce roughly half of the  $d_4$  shift.

#### v. Resonance Raman Spectra of CuECI

For metalloporphyrins, the change in peripheral substituents that occurs upon going from CuOEP to CuEPI (Figure 3.1) affects those modes with a contribution from  $C_bC_b$  and  $C_bC_s$  stretching and  $C_bC_s$  bending coordinates (99). A similar dependence of the frequency of the analogous modes on peripheral substituents is expected for the metallochlorins and provides a means by which these modes may be identified. Figure 3.11 shows the resonance Raman spectra of CuECI in  $CH_2Cl_2$  solution obtained with Soret excitation at 406.7 nm,  $Q_x$  excitation at 488.0 nm and  $Q_y$  excitation at 615.0 nm. The 1584, 1547 and 1543  $cm^{-1}$  modes of CuOEC show increases in frequency of +4, +4 and +3  $cm^{-1}$ , respectively, as a result of the change in peripheral substituents on going to CuECI. In addition, the 1238, 1215 and 1198  $cm^{-1}$  modes of CuOEC also exhibit increases in frequency. The change in peripheral



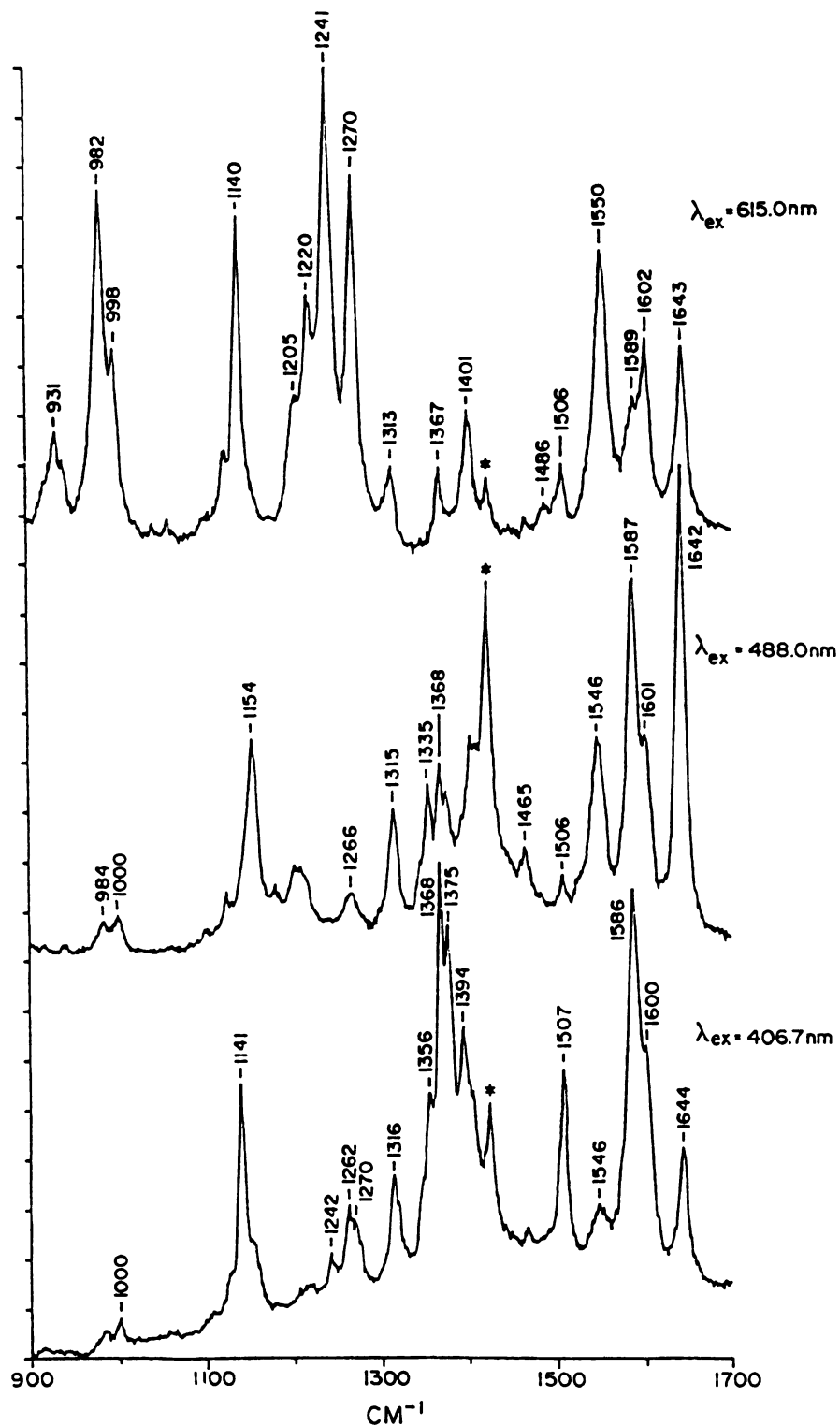


Figure 3.11 Resonance Raman spectra of CuECI in CH<sub>2</sub>Cl<sub>2</sub> solution obtained with Soret excitation at 406.7 nm, Q<sub>x</sub> excitation at 488.0 nm and Q<sub>y</sub> excitation at 615.0 nm. Laser powers: 6, 70 and 40 mW, respectively

substituents lowers the frequencies of the 1372, 1361, 1350 and 1277  $\text{cm}^{-1}$  modes of CuOEC by -4, -5, -3 and -7  $\text{cm}^{-1}$ , respectively, and the 1021  $\text{cm}^{-1}$  mode appears to split into two components at 998 and 982  $\text{cm}^{-1}$  in CuECI.

#### vi. Solid State Spectra

For their normal coordinate analysis of NiOEC, Boldt et al. (83) obtained resonance Raman spectra of NiOEC pressed into  $\text{Na}_2\text{SO}_4$  pellets. However, differences occur in the number and frequencies of the resonance Raman modes of NiOEC in  $\text{Na}_2\text{SO}_4$  and in  $\text{CH}_2\text{Cl}_2$  solution. In order to compare the results obtained here with those of Boldt et al., solid state resonance Raman spectra were recorded for NiOEC (Figure 3.12) and CuOEC (Figure 3.13) in KBr pellets. The high frequency modes of NiOEC and CuOEC are shifted to lower frequencies in KBr. Additionally, the high frequency bands of NiOEC display an altered pattern of relative intensities with 406.7 nm Soret excitation for the KBr sample and Boldt's  $\text{Na}_2\text{SO}_4$  sample compared to NiOEC in  $\text{CH}_2\text{Cl}_2$  solution. Resonance Raman spectra of CuOEC in KBr on the other hand, showed the same pattern of relative intensities as in  $\text{CH}_2\text{Cl}_2$  solution with Soret,  $Q_x$  and  $Q_y$  excitation. The 1572  $\text{cm}^{-1}$  band in the NiOEC spectrum appears to be an artifact of the solid state since its relative intensity increased as the ratio of NiOEC to KBr in the pellet was lowered. No evidence for this mode could be found in the

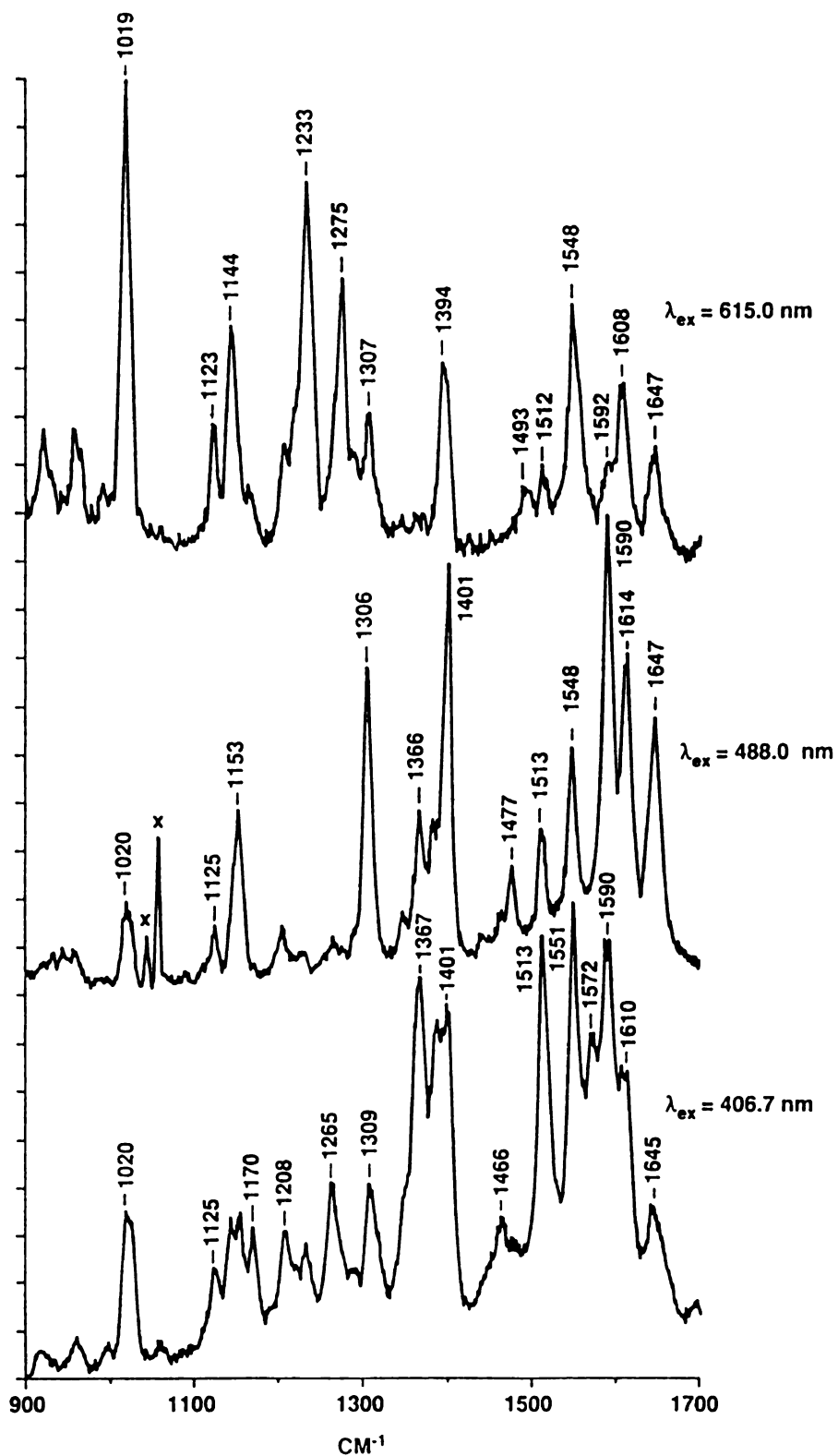


Figure 3.12 Resonance Raman spectra of NiOEC in KBr obtained with Soret excitation at 406.7 nm,  $Q_x$  excitation at 488.0 nm and  $Q_y$  excitation at 615.0 nm. Laser powers: 20, 70 and 50 mW, respectively

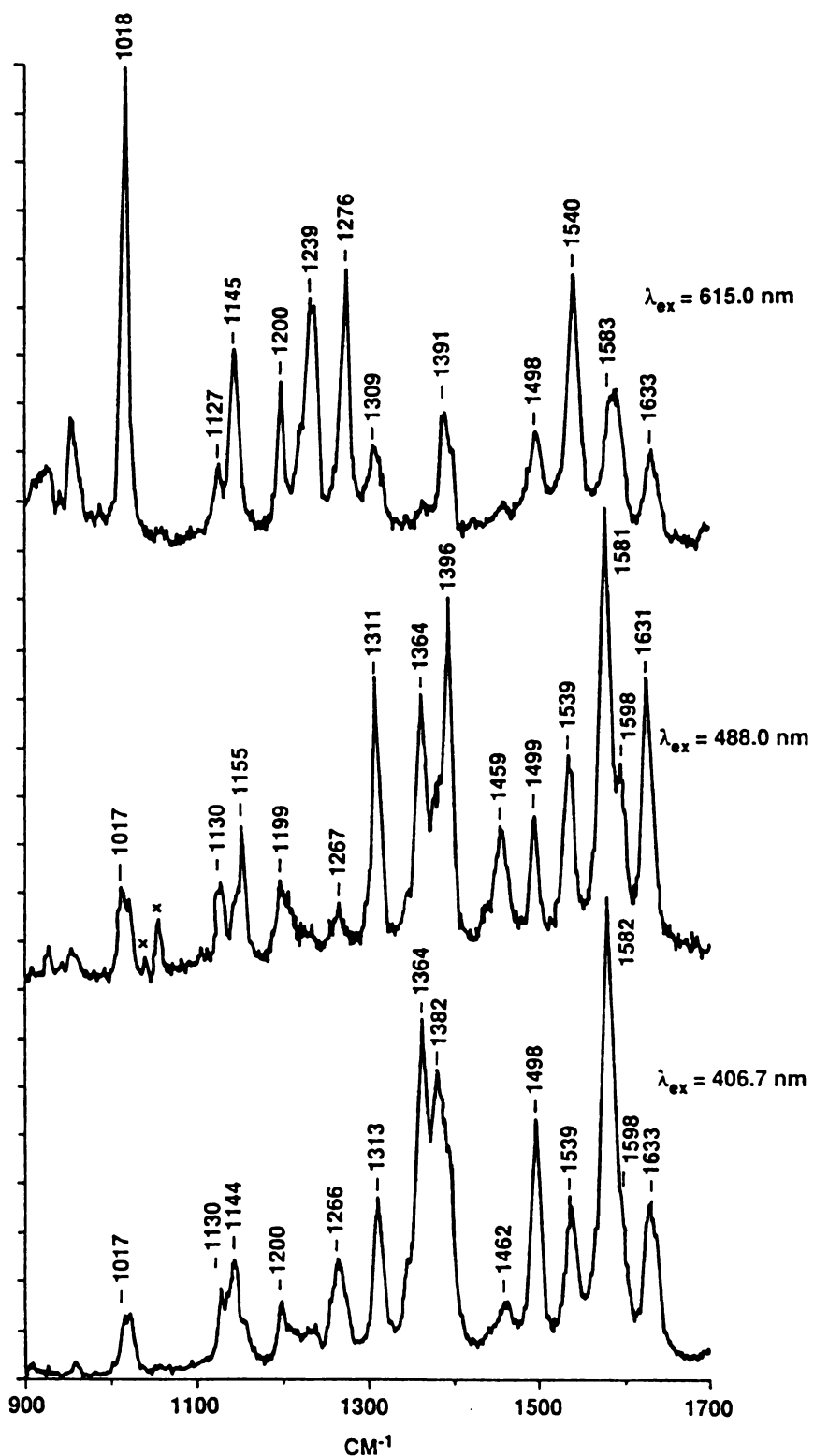


Figure 3.13 Resonance Raman spectra of CuOEC in KBr obtained with Soret excitation at 406.7 nm,  $Q_x$  excitation at 488.0 nm and  $Q_y$  excitation at 615.0 nm. Laser powers: 20, 75 and 50 mW, respectively

IR spectrum of NiOEC in KBr or for an analogous mode in the resonance Raman spectra or IR spectrum of CuOEC in KBr.

### 3. Discussion

#### i. $C_aC_m$ and $C_bC_b$ Modes

Upon reduction of a  $C_bC_b$  bond in a metalloporphyrin to form a metallochlorin, the molecular symmetry is lowered from  $D_{4h}$  to  $C_2$ . For  $C_2$  symmetry, the resonance Raman active and IR active vibrational modes belong to the A and B symmetry species. The resonance Raman active polarized  $A_{1g}$  and depolarized  $B_{1g}$  modes of  $D_{4h}$  symmetry are expected to produce polarized modes of A symmetry in  $C_2$ . The anomalously polarized  $A_{2g}$  and depolarized  $B_{2g}$  modes correlate with depolarized B modes. The IR active  $E_u$  modes split into A and B. The A and B modes are both IR and Raman active. Under  $C_2$  symmetry, eight  $C_aC_m$  stretching ( $4A + 4B$ ) and four  $C_bC_b$  stretching ( $2A + 2B$ ) modes are predicted. Four of the  $C_aC_m$  and two of the  $C_bC_b$  stretching modes are derived from  $E_u$  modes.

In their initial study, Ozaki et al. (95) assigned the resonance Raman modes of CuOEC at 1643 (p), 1584 (dp) (see 102) and 1506 (p)  $\text{cm}^{-1}$  as corresponding to the  $\nu_{10}$  ( $B_{1g}$ , dp),  $\nu_{19}$  ( $A_{2g}$ , ap) and  $\nu_3$  ( $A_{1g}$ , p) modes of NiOEP, respectively. The observed polarizations of these three modes with 488.0 nm

excitation are consistent with the  $D_{4h}$  to  $C_2$  symmetry correlation. The  $1546\text{ cm}^{-1}$  mode was presumed to consist of a polarized and an anomalously polarized component. The ap mode that shifts to  $1527\text{ cm}^{-1}$  on  $\gamma,\delta$  deuteration was assigned to the other  $C_sC_m$  mode. If this mode is not derived from an  $E_u$  mode it would have to correspond to  $\nu_{28}$  ( $B_{2g}$ , dp) of NiOEP calculated at  $1469\text{ cm}^{-1}$  (55). The  $1602$  (ap) and  $1546$  (p)  $\text{cm}^{-1}$  modes of CuOEC, which are unshifted upon  $\gamma,\delta$  deuteration, were assigned as corresponding to  $\nu_2$  ( $A_{1g}$ , p) and  $\nu_{11}$  ( $B_{1g}$ , dp). However, the anomalous polarization of the  $1602\text{ cm}^{-1}$  mode is inconsistent with this mode being derived from a porphyrin  $A_{1g}$  mode.

Such a symmetry-lowering approach does not adequately account for the vibrational mode assignments for the metallo-chlorins. For these compounds our results indicate that there is mixing of  $C_sC_m$  and  $C_bC_b$  stretching character in the high frequency modes that is not predicted by direct comparison with the normal modes of NiOEP. This is apparent in the frequency region from  $1475$  to  $1700\text{ cm}^{-1}$  where seven modes, corresponding to the  $1644$ ,  $1602$ ,  $1584$ ,  $1547$ ,  $1543$ ,  $1507$  and  $1486\text{ cm}^{-1}$  modes of CuOEC, are observed to be metal, and hence core-size, dependent.

The relationship between vibrational frequency and core-size of a metalloporphyrin often follows the empirical expression (62):

$$\nu = K ( A - d )$$

where  $\nu$  is the vibrational frequency in  $\text{cm}^{-1}$ ,  $d$  is the center to nitrogen distance or core-size of the metalloporphyrin in Å, and  $K$  ( $\text{cm}^{-1}/\text{Å}$ ) and  $A$  (Å) are parameters characteristic of the macrocycle. The physically useful parameter is the slope or  $K$  value, which is proportional to the amount of  $C_aC_m$  stretching character in the vibrational mode. Ozaki *et al.* (66) have previously applied this kind of analysis to metallochlorins; they achieved core-size variation by working with iron complexes in different spin and oxidation states. The iron chlorins, however, are susceptible to the same sorts of difficulties in such an analysis as are encountered with the corresponding iron porphyrins (63,65) and for this reason our analysis has been carried out for metals other than iron. The correlations between vibrational frequency and core-size for the high frequency modes of the Ni, Cu and Zn complexes of OEC and OEP are shown in Figures 3.14 and 3.15. The same core-sizes are assumed for the porphyrin and chlorin complexes, namely Ni (1.958 Å) (60), Cu (2.000 Å) (103) and Zn (2.047 Å) (104). The core-size correlation parameters,  $K$  and  $A$ , are listed in Table 3.4 for MOEC and in Table 3.5 for MOEP. From the chlorin  $K$  values, the 1644, 1602, 1543, 1507 and 1486

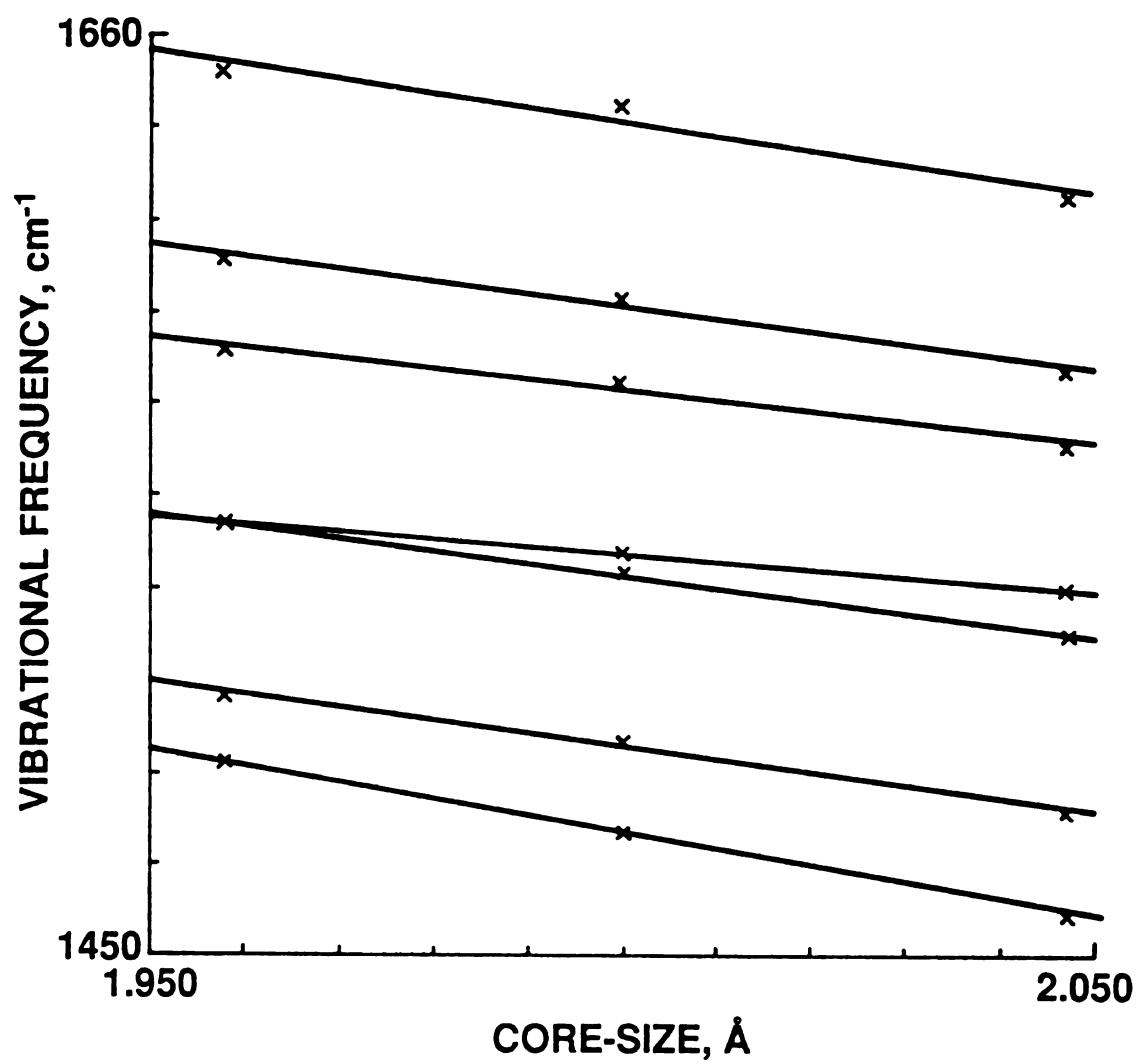


Figure 3.14 Core-size correlation for the high frequency modes of MOEC



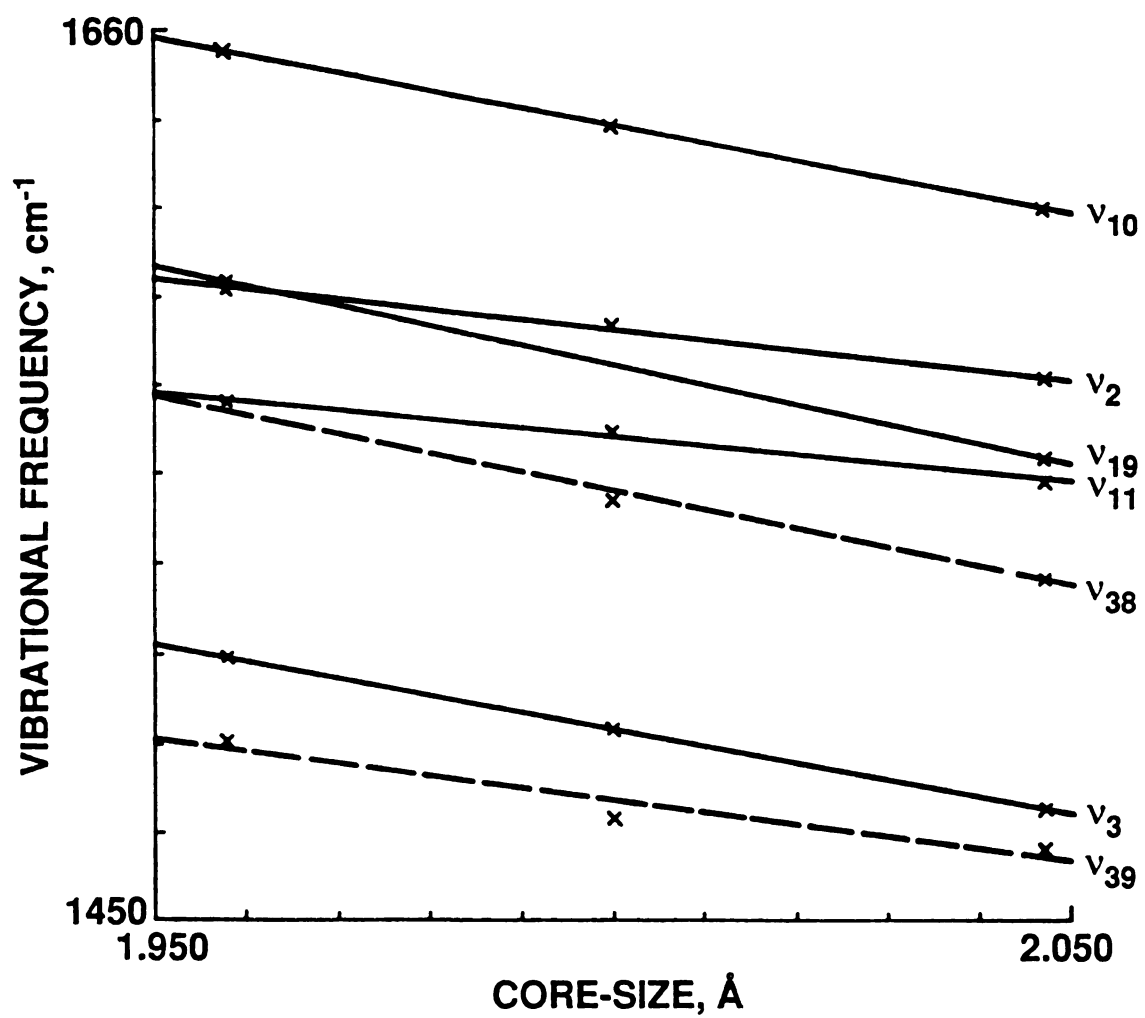


Figure 3.15 Core-size correlation for the resonance Raman active (—) and IR active (- -) high frequency modes of MOEP

Table 3.4 Vibrational frequencies ( $\text{cm}^{-1}$ ), isotope shifts ( $\text{cm}^{-1}$ ) and core-size correlation parameters for metallochlorin  $\text{C}_6\text{C}_8$  and  $\text{C}_6\text{C}_9$  normal modes

NiOEC	$\Delta\nu$ CuOEC	$\Delta\nu$ $\alpha, \beta - d_2$	$\Delta\nu$ $\gamma, \delta - d_2$	$\Delta\nu$ $d_4$	$\Delta\nu^a$ subst	$K$ ( $\text{cm}^{-1}/\text{\AA}$ )	$A$ ( $\text{\AA}$ )	Assignment	Normal coordinate analysis results for NiOEC <sup>b</sup>
									No. Obs. Calc. Assignment
1652	1644	-3	-7	-10	0	317	7.17	$\nu\text{C}_6\text{C}_8(\gamma, \delta)$ , $\nu\text{C}_6\text{C}_8(\alpha, \beta)$	1 1648 1649 $\nu\text{C}_6\text{C}_8(\gamma, \delta)$
									2 1644 1637 $\nu\text{C}_6\text{C}_8(\gamma, \delta)$
1613	1602	-12	-2	-13	0	282	7.67	$\nu\text{C}_6\text{C}_8(\alpha, \beta)$	3 1614 1618 $\nu\text{C}_6\text{C}_8(\alpha, \beta)$
									4 1608 1561 $\nu\text{C}_6\text{C}_8(\text{I, III})$
1589	1584	-4	-4	-9	+4	237	8.67	$\nu\text{C}_6\text{C}_8$ , $\nu\text{C}_6\text{C}_8(\alpha, \beta, \gamma, \delta)$	5 1590 1607 $\nu\text{C}_6\text{C}_8(\alpha, \beta)$
									6 1572 1557 $\nu\text{C}_6\text{C}_8(\text{I, III})$
1554	1547	-1	0	-3	+4	169	11.15	$\nu\text{C}_6\text{C}_8$	7 1546 1532 $\nu\text{C}_6\text{C}_8(\text{II})$ , $\nu\text{C}_6\text{C}_8(\alpha, \beta)$
--	1543	0	-17	-17	+3	270	7.71	$\nu\text{C}_6\text{C}_8(\gamma, \delta)$ , $\nu\text{C}_6\text{C}_8$	-
									8 -- 1540 $\nu\text{C}_6\text{C}_8(\text{II})$ , $\nu\text{C}_6\text{C}_8(\text{I, III})$
1517	1507	-6	-6	-13	0	293	7.14	$\nu\text{C}_6\text{C}_8(\alpha, \beta, \gamma, \delta)$	9 1512 1489 $\nu\text{C}_6\text{C}_8(\alpha, \beta, \gamma, \delta)$ , $\nu\text{C}_6\text{C}_8(\text{I, II, III})$
1502	1486	-4	-7	-10	0	381	6.90	$\nu\text{C}_6\text{C}_8(\gamma, \delta)$ , $\nu\text{C}_6\text{C}_8(\alpha, \beta)$	10 1492 1498 $\nu\text{C}_6\text{C}_8(\text{I, II, III})$
1483	--								11 1478 1506 $\nu\text{C}_6\text{C}_8(\alpha, \beta, \gamma, \delta)$ , $\nu\text{C}_6\text{N}(\text{I, II})$

<sup>a</sup>  $\Delta\nu$  subst: frequency shift on change of peripheral substituents from CuOEC to CuECI.

<sup>b</sup> from ref. 83.

Table 3.5 Vibrational frequencies ( $\text{cm}^{-1}$ ), isotope shifts ( $\text{cm}^{-1}$ ) and core-size correlation parameters for metalloporphyrin  $\text{C}_a\text{C}_m$  and  $\text{C}_b\text{C}_b$  normal modes

Mode <sup>a</sup>	CuOEP	$\Delta\nu$ $d_2$	$\Delta\nu$ $d_4$	$\Delta\nu$ subst <sup>b</sup>	$K^c$ ( $\text{cm}^{-1}/\text{\AA}$ )	$A^c$ ( $\text{\AA}$ )	P.E.D. <sup>a</sup>
$\nu_{10}$	1639	-6	-13	+3	405	6.05	$\nu(\text{C}_a\text{C}_m) 49$ , $\nu(\text{C}_b\text{C}_b) 17$
$\nu_2$	1591	+1	0	+6	236	8.74	$\nu(\text{C}_b\text{C}_b) 60$ , $\nu(\text{C}_b\text{-Et}) 19$
$\nu_{19}$	1584	-14	-22	--	449	5.53	$\nu'(\text{C}_a\text{C}_m) 67$ , $\nu'(\text{C}_b\text{C}_b) 18$
$\nu_{11}$	1572	0	-3 <sup>d</sup>	+6	203	9.73	$\nu(\text{C}_b\text{C}_b) 57$ , $\nu(\text{C}_b\text{-Et}) 16$
$\nu_3$	1505	-5	-10	+2	382	5.94	$\nu(\text{C}_a\text{C}_m) 41$ , $\nu(\text{C}_b\text{C}_b) 35$
$\nu_{37}$	--	--	--	--	---	----	$\nu(\text{C}_b\text{C}_b) 57$ , $\nu\text{C}_b\text{-Et}) 16^*$
$\nu_{38}$	1554 <sup>f</sup>	--	--	--	426	5.66	$\nu(\text{C}_a\text{C}_m) 34$ , $\nu'(\text{C}_a\text{C}_m) 24^*$
$\nu_{39}$	1483 <sup>f</sup>	--	--	--	278	7.34	$\nu'(\text{C}_a\text{C}_m) 36$ , $\nu'(\text{C}_a\text{N}) 17$

<sup>a</sup> Mode designation and P.E.D. from the normal coordinate analysis of NiOEP (55).

<sup>b</sup>  $\Delta\nu$  subst: frequency shift on change of peripheral substituents from CuOEP to CuEPI (99).

<sup>c</sup> calculated for ZnOEP, CuOEP and NiOEP using data from ref. 105.

<sup>d</sup> see ref. 101.

<sup>e</sup> P.E.D. for  $\nu_{37}$  and  $\nu_{38}$  have been interchanged (100).

<sup>f</sup> from ref. 100.

$\text{cm}^{-1}$  modes of CuOEC have substantial  $\text{C}_a\text{C}_m$  stretching, but for the 1584 and 1547  $\text{cm}^{-1}$  modes, contribution from the  $\text{C}_b\text{C}_b$  stretching coordinate is more apparent. The 1486  $\text{cm}^{-1}$  mode of CuOEC shows the highest K value. Significantly, the K values for the other chlorin  $\text{C}_a\text{C}_m$  stretching modes are all lower than the porphyrin K values for the Raman active  $\text{C}_a\text{C}_m$  stretching modes:  $\nu_{10}$  (K=405),  $\nu_{19}$  (K=449) and  $\nu_3$  (K=382) and the IR active  $\nu_{38}$  (K=426). The chlorin K values are close to the K value for the porphyrin IR active  $\nu_{39}$  (K=278), which has 36%  $\text{C}_a\text{C}_m$  stretching character in the calculated P.E.D. for NiOEP. Of the two chlorin  $\text{C}_b\text{C}_b$  stretching modes, the K value of the 1584  $\text{cm}^{-1}$  mode is virtually identical to that of  $\nu_2$  (K=236) whereas the K value of the 1547  $\text{cm}^{-1}$  mode is lower than that of  $\nu_{11}$  (K=203) (106). The different K values that we observe for the chlorins indicate altered mode compositions compared to the MOEP complexes; in particular, they suggest that there is mixing of  $\text{C}_a\text{C}_m$  and  $\text{C}_b\text{C}_b$  stretching coordinates in the high frequency normal modes.

To characterize further the high-frequency modes we have examined their sensitivity to methine deuteration and to a change in peripheral substituents upon going from OEC to ECI. The frequency shifts observed for CuOEC- $\text{d}_4$  and CuECI (Table 3.4) can be compared to CuOEP- $\text{d}_4$  and CuEPI (Table 3.5). In methine-deuterated CuOEP- $\text{d}_4$ , the  $\text{C}_a\text{C}_m$  stretching modes  $\nu_{10}$ ,  $\nu_{19}$  and  $\nu_3$  exhibit frequency shifts of -13, -22 and -10  $\text{cm}^{-1}$  compared to CuOEP but the  $\text{C}_b\text{C}_b$  stretching modes  $\nu_2$  and  $\nu_{11}$  are

unaffected. In addition, Kincaid et al. observed -11 and -7  $\text{cm}^{-1}$  shifts for the  $\text{C}_a\text{C}_m$  stretching modes  $\nu_{38}$  and  $\nu_{39}$  from the IR spectra of NiOEP and NiOEP- $\text{d}_4$  (100). The 1644, 1602, 1584, 1543, 1507 and 1486  $\text{cm}^{-1}$  modes of CuOEC show substantial frequency shifts of -10, -13, -9, -17, -13 and -10  $\text{cm}^{-1}$  upon  $\text{d}_4$  methine deuteration. The magnitude of the frequency shifts indicates that these modes contain  $\text{C}_a\text{C}_m$  stretching character. Comparison of the resonance Raman spectra of CuOEP with CuEPI showed that a change in peripheral substituents resulted in an increase in frequency of the  $\text{C}_b\text{C}_b$  stretching modes  $\nu_2$  and  $\nu_{11}$  by +6  $\text{cm}^{-1}$  (99). For CuOEC, we observe that the 1584, 1547 and 1543  $\text{cm}^{-1}$  modes increase in frequency by +4, +4 and +3  $\text{cm}^{-1}$  in CuECI. These modes are therefore predicted to contain  $\text{C}_b\text{C}_b$  stretching character. The mode characters deduced from  $\text{d}_4$  methine deuteration and the change in peripheral substituents (Table 3.4) are in good agreement with those predicted from the K values for MOEC. The results of the core-size correlation together with the analysis of the wavenumber shifts incurred upon methine deuteration clearly demonstrate that there is mixing of the  $\nu(\text{C}_a\text{C}_m)$  and  $\nu(\text{C}_b\text{C}_b)$  internal coordinates in the high frequency normal modes.

The above results show that the mode characters observed for the high-frequency modes of CuOEC cannot be assigned by direct comparison with the normal modes of NiOEP. The resonance Raman spectrum of CuOEC- $\gamma,\delta\text{-d}_2$  reported by Ozaki et al. (95) showed no shift of the 1602  $\text{cm}^{-1}$  mode of CuOEC upon

$\gamma, \delta$  deuteration and led these authors to conclude that the  $1602\text{ cm}^{-1}$  mode corresponded to the porphyrin  $\nu_2$   $C_bC_b$  stretching mode. We observe that the  $1602\text{ cm}^{-1}$  mode shifts to  $1589\text{ cm}^{-1}$  in CuOEC- $d_4$  indicating substantial  $C_aC_m$  stretching character. To reconcile these deuteration effects the frequency shifts for CuOEC- $\gamma, \delta$ - $d_2$ , CuOEC- $\alpha, \beta$ - $d_2$  and CuOEC- $d_4$  were compared. As seen in Figures 3.7 and 3.8 and Table 3.4, the high-frequency modes exhibit different shifts upon  $\alpha, \beta$  and  $\gamma, \delta$  deuteration. The large ( $-13\text{ cm}^{-1}$ ) frequency shift of the  $1602\text{ cm}^{-1}$  mode results from deuteration at the  $\alpha, \beta$  positions but deuteration at the  $\gamma, \delta$  positions has little effect on the frequency of this mode. On the other hand, the  $1543\text{ cm}^{-1}$  mode of CuOEC is shifted by  $-17\text{ cm}^{-1}$  upon  $\gamma, \delta$  deuteration and is unaffected by deuteration at the  $\alpha, \beta$  positions. Both the  $1644$  and  $1486\text{ cm}^{-1}$  modes of CuOEC show unequal frequency shifts upon  $\alpha, \beta$  and  $\gamma, \delta$  deuteration with the larger shift resulting from  $\gamma, \delta$  deuteration. The frequency shifts upon deuteration that we observe for CuOEC support the idea of mode localization in metallochlorins as proposed by Boldt et al. (83) from their study of NiOEC.

In Table 3.4 our results are compared with the assignments of Boldt et al. for NiOEC. Before proceeding to our analysis, we note that differences occur in the number and frequencies of the resonance Raman modes of NiOEC in  $\text{Na}_2\text{SO}_4$  and in  $\text{CH}_2\text{Cl}_2$  solution reported here. The  $1644$ ,  $1608$  and  $1572\text{ cm}^{-1}$  modes of NiOEC in  $\text{Na}_2\text{SO}_4$  pellets are not observed in

either the resonance Raman or IR spectra of NiOEC in solution and appear to be artifacts of the solid state spectra of NiOEC. These modes are not considered further in this analysis.

The 1648, 1614 and 1512  $\text{cm}^{-1}$  modes of NiOEC in  $\text{Na}_2\text{SO}_4$  were assigned by Boldt et al. to  $\text{C}_\alpha\text{C}_\beta$  stretching modes that are  $\gamma,\delta$  localized,  $\alpha,\beta$  localized, and delocalized, respectively. In CuOEC, we observe the analogous modes at 1644, 1602 and 1507  $\text{cm}^{-1}$ . From their methine  $d_\alpha$  shifts and apparent insensitivity to changes in peripheral substituents at the  $\text{C}_\beta$  positions, these modes are assigned to  $\text{C}_\alpha\text{C}_\beta$  stretching vibrations in agreement with Boldt et al. Furthermore, the observation of equal and additive frequency shifts upon  $\alpha,\beta$  and  $\gamma,\delta$  deuteration shows that the 1507  $\text{cm}^{-1}$  mode is delocalized over the chlorin macrocycle. Our deuteration shifts also confirm that the 1602  $\text{cm}^{-1}$  mode is  $\alpha,\beta$  localized. The 1644  $\text{cm}^{-1}$  mode shows both  $\alpha,\beta$  and  $\gamma,\delta$   $\text{C}_\alpha\text{C}_\beta$  stretching character but with a greater localization in the  $\gamma,\delta$  methines than in the  $\alpha,\beta$  methines. This is a slight alteration from the assignment of Boldt et al. who represented this mode as a 50/50 in-phase linear combination of the  $\nu_{10}$  and  $\nu_{37a}$  modes of NiOEP. Since we observe frequency shifts upon both  $\alpha,\beta$  and  $\gamma,\delta$  deuteration, a more accurate representation of this mode could be derived from a 50/20 in-phase combination of  $\nu_{10}$  and  $\nu_{37a}$ . The 1644 and 1507  $\text{cm}^{-1}$  modes of CuOEC retain much of the character of the  $\nu_{10}$  and  $\nu_3$  modes of NiOEP.





The compositions deduced for the 1584 and 1486  $\text{cm}^{-1}$  modes of CuOEC do not agree with those proposed by Boldt et al. The 1584  $\text{cm}^{-1}$  mode exhibits mixed  $\text{C}_b\text{C}_b$  and  $\text{C}_a\text{C}_m$  stretching character as judged by the intermediate K value, the +4  $\text{cm}^{-1}$  shift upon change of peripheral substituents and the -9  $\text{cm}^{-1}$  shift upon  $d_a$  methine deuteration. The equal -4  $\text{cm}^{-1}$  shifts upon  $\alpha,\beta$  and  $\gamma,\delta$  deuteration indicate a delocalized mode. Boldt et al. assigned the analogous 1590  $\text{cm}^{-1}$  mode of NiOEC in  $\text{Na}_2\text{SO}_4$  to  $\text{C}_a\text{C}_m$  stretching localized in the  $\alpha,\beta$  methines. Disagreement is also found for the 1492  $\text{cm}^{-1}$  mode of NiOEC in  $\text{Na}_2\text{SO}_4$  which was assigned by Boldt et al. to  $\text{C}_a\text{C}_b$  stretching localized in rings I, II and III. We observe the corresponding mode at 1486  $\text{cm}^{-1}$  for CuOEC in  $\text{CH}_2\text{Cl}_2$  solution with  $Q_y$  excitation. The high K value and -10  $\text{cm}^{-1}$  shift upon  $d_a$  methine deuteration indicate  $\text{C}_a\text{C}_m$  stretching rather than  $\text{C}_a\text{C}_b$  stretching character. The frequency shifts upon  $\alpha,\beta$  and  $\gamma,\delta$  deuteration show a greater  $\gamma,\delta$  localization for this mode.

For CuOEC, we assign the 1547  $\text{cm}^{-1}$  mode to  $\text{C}_b\text{C}_b$  stretching and the 1543  $\text{cm}^{-1}$  mode to a mixture of  $\text{C}_b\text{C}_b$  stretching and  $\gamma,\delta$  localized  $\text{C}_a\text{C}_m$  stretching. The observation of these two modes in CuOEC is interesting since the normal coordinate analysis of Boldt et al. predicts four modes in this region at 1561, 1557, 1540 and 1532  $\text{cm}^{-1}$ . Two of the modes (calculated at 1561 and 1557  $\text{cm}^{-1}$ ) are predicted to have  $\text{C}_b\text{C}_b$  stretching character while the calculated 1540  $\text{cm}^{-1}$  mode is predicted to have  $\text{C}_a\text{C}_b$  stretching character. In their resonance Raman spectra of

NiOEC in  $\text{Na}_2\text{SO}_4$ , only a single mode at  $1546\text{ cm}^{-1}$  was observed and this mode did not shift in NiOEC- $\gamma,\delta\text{-d}_2$ . This  $1546\text{ cm}^{-1}$  mode of NiOEC was assigned by Boldt *et al.* to  $\text{C}_b\text{C}_b$  and  $\alpha,\beta$  localized  $\text{C}_a\text{C}_m$  stretching calculated at  $1532\text{ cm}^{-1}$ . The  $\text{C}_b\text{C}_b$  stretching character seen in the  $1547$  and  $1543\text{ cm}^{-1}$  modes supports the normal coordinate analysis although the  $\text{C}_a\text{C}_m$  stretching character in the  $1543\text{ cm}^{-1}$  mode has  $\gamma,\delta$  localization and not  $\alpha,\beta$  localization.

## ii. $\text{C}_a\text{N}$ Modes

Under  $\text{C}_2$  symmetry, six  $\text{C}_a\text{N}$  stretching modes would be expected for a metallochlorin (107). The resonance Raman spectrum of CuOEC- $^{15}\text{N}_4$ , recorded by Ozaki *et al.* (95) showed that the  $1402$ ,  $1372$ ,  $1361$ ,  $1318$ ,  $1157$  (see 108) and  $1128\text{ cm}^{-1}$  modes of CuOEC shifted by  $-1$ ,  $-6$ ,  $-5$ ,  $-5$ ,  $-9$  and  $-19\text{ cm}^{-1}$ , respectively, upon  $^{15}\text{N}_4$  substitution. These modes are therefore assigned to  $\text{C}_a\text{N}$  stretching. In Table 3.6, we have summarized the Raman active modes observed for CuOEC and NiOEC in  $\text{CH}_2\text{Cl}_2$  solution and for NiOEC in  $\text{Na}_2\text{SO}_4$ , along with the assignments proposed by Boldt *et al.* (83) from their normal coordinate analysis. In this region, solution spectra gave somewhat better resolution than pellet data as the  $1367\text{ cm}^{-1}$  mode of NiOEC in  $\text{Na}_2\text{SO}_4$  (and in our spectra in KBr, Figure 3.12) has two components in  $\text{CH}_2\text{Cl}_2$  solution at  $1373$  and  $1363\text{ cm}^{-1}$ . Similarly, for CuOEC in KBr (Figure 3.13), we observe a single

Table 3.6 Vibrational frequencies ( $\text{cm}^{-1}$ ) and isotope shifts ( $\text{cm}^{-1}$ ) for metallochlorin C<sub>a</sub>N modes

NiOEC	CuOEC	$\Delta\nu$ $^{15}\text{N}_i^a$	$\Delta\nu$ subst.	No.	Normal coordinate analysis results for NiOEC <sup>b</sup>		
					Obs.	Calc.	Assignment
1404	1402	-1	0	14	1402	1489	$\nu\text{C}_a\text{C}_b(\text{I, II, III}),$ $\nu\text{C}_a\text{N}(\text{I, III, IV})$
1373	1372	-6	-4	--			
1363	1361	-5	-5	17	1367	1339	$\nu\text{C}_a\text{N}(\text{I, II, III, IV}),$ $\nu\text{C}_b\text{C}_b(\text{I, II, III})$
1306	1318	-5	-3	20	1308	1301	$\delta\text{C}_m\text{H}(\alpha, \beta),$ $\nu\text{C}_a\text{C}_b(\text{I, III})$
1154	1157	-9	-3	27	1152	1147	$\nu\text{C}_b\text{Et}(\text{I, II, III}),$ $\nu\text{C}_a\text{N}$
1123	1128	-19	-3	29	1124	1083	$\nu\text{C}_b\text{Et}(\text{I, II, III}),$ $\delta\text{C}_m\text{C}_a\text{N}(\text{IV})$

<sup>a</sup> from ref. 95.

<sup>b</sup> from ref. 83.

1364  $\text{cm}^{-1}$  mode that corresponds to the 1372 and 1361  $\text{cm}^{-1}$  bands of CuOEC in solution.

The normal coordinate analysis of NiOEC indicates that there is mixing of the  $\text{C}_\alpha\text{N}$  character with  $\text{C}_\alpha\text{C}_\beta$ ,  $\text{C}_\beta\text{C}_\beta$  and  $\text{C}_\beta\text{Et}$  stretching coordinates. The involvement of the  $\text{C}_\beta$  atoms in these vibrational modes can be seen from the sensitivity of four of the modes to a change of peripheral substituents in CuECI (Table 3.6). The 1308 and 1124  $\text{cm}^{-1}$  modes of NiOEC in  $\text{Na}_2\text{SO}_4$  were assigned to modes 20 and 29, respectively, but the P.E.D.'s have no contribution from  $\text{C}_\alpha\text{N}$  stretching. In order to account for the observed  $^{15}\text{N}_4$  frequency shifts it would perhaps be better to assign the 1318  $\text{cm}^{-1}$  mode of CuOEC to mode number 19 ( $\nu\text{C}_\alpha\text{N}(\text{I,III,IV})$ ,  $\delta\text{C}_\alpha\text{H}(\gamma,\delta)$ ) and the 1128  $\text{cm}^{-1}$  mode to number 28 ( $\nu\text{C}_\beta\text{Et}(\text{I,II,III})$ ,  $\nu\text{C}_\alpha\text{N}(\text{I,III})$ ).

### iii. $\text{C}_\alpha\text{H}$ Modes

The normal coordinate calculations of Boldt et al. (83) indicate that the  $\alpha,\beta$  and  $\gamma,\delta$  hydrogen motions of NiOEC are mixed with porphyrin skeletal modes and furthermore, that the  $\gamma,\delta$  hydrogen motions are mixed with  $\text{C}_\beta\text{H}$  deformations on ring IV. Table 3.7 collects our information on the more prominent modes that have  $\text{C}_\alpha\text{H}$  contributions. As was found for the skeletal modes, the  $\text{C}_\alpha\text{H}$  modes can be divided into three classes: a) those that are localized to the  $\alpha,\beta$  porphyrin-like

Table 3.7 Vibrational frequencies ( $\text{cm}^{-1}$ ) for CuOEC normal modes in the frequency region below  $1350 \text{ cm}^{-1}$

CuOEC	$\alpha, \beta\text{-d}_2$	$\gamma, \delta\text{-d}_2$	$\text{d}_4$	NiOEP mode #
1. $\alpha, \beta$ localized				
1277	--	1275	--	--
1215	946	1215	946	$\nu_{13}$
--	1325	--	1322	$\nu_{12}$
--	1178	--	1180	$\nu_{14}$
2. $\gamma, \delta$ localized				
1238	--	1224	--	
1198		--		
--		1173		
1141	1140	914	914	

part of the molecule, b) those that are  $\gamma, \delta$  localized, and c) those that are substantially delocalized throughout the macrocycle.

The  $\alpha, \beta$   $C_mH$  deformations show clear porphyrin-like behavior. Comparison of the spectra of CuOEC and CuOEC- $\alpha, \beta$ -d<sub>2</sub> (Figure 3.8) reveals that the mode at 1215 cm<sup>-1</sup> shifts to 946 cm<sup>-1</sup> and an intense band at 1178 cm<sup>-1</sup> appears upon deuteration. This behavior is analogous to that exhibited by the  $\nu_{13}$  and  $\nu_{14}$  modes of NiOEP (55,56,59). Moreover, the appearance of the 1325 cm<sup>-1</sup> mode in the CuOEC- $\alpha, \beta$ -d<sub>2</sub> spectrum reflects that of  $\nu_{12}$  in NiOEP, which is usually not observed in the natural abundance spectrum (55). Boldt et al. predicted an  $\alpha, \beta$  localized mode at 1277 cm<sup>-1</sup> and the spectra in Figure 3.8 confirm this. However, this vibration does not have a corresponding metalloporphyrin normal mode. The vibrational coordinates of the above four modes are  $\alpha, \beta$  localized as they are unperturbed by  $\gamma, \delta$ -d<sub>2</sub> deuteration and their frequencies in the  $\alpha, \beta$ -d<sub>2</sub> species persist virtually unchanged in CuOEC-d<sub>4</sub>. Some indication that the  $\alpha, \beta$   $C_mH$  bending deformations contribute to more delocalized modes can be seen in the behavior of the cluster of modes in the 1190-1250 cm<sup>-1</sup> region, which shows complicated intensity and frequency shifts in all three of the deuterated complexes relative to CuOEC.

The  $\gamma, \delta$   $C_m$  deformations were suggested by Boldt et al. to be extensively mixed with ring modes and thus to exhibit

complex behavior. Nonetheless, the data of Figure 3.8 provide several key insights into the characteristics of these motions. Upon  $\gamma,\delta$ -d<sub>2</sub> deuteration the mode at 1141 cm<sup>-1</sup> disappears and new modes at 914 and 1173 cm<sup>-1</sup> become apparent. The 1238 cm<sup>-1</sup> mode apparently downshifts to 1224 cm<sup>-1</sup> upon the same substitution. The behavior of the 1141 and 914 cm<sup>-1</sup> modes indicates that these motions are strongly localized as their frequencies carry through essentially unchanged in the  $\alpha,\beta$ -d<sub>2</sub> and d<sub>4</sub> species, respectively. A judgement as to the extent of localization of the 1173 cm<sup>-1</sup> mode is rendered difficult since this region is obscured by the strong  $\alpha,\beta$  localized 1180 cm<sup>-1</sup> mode in CuOEC- $\alpha,\beta$ -d<sub>2</sub> and CuOEC-d<sub>4</sub>. Soret excitation data (not shown), however, suggest that this mode is also  $\gamma,\delta$  localized.

#### iv. Ethyl Group Vibrations

The IR spectrum of CuOEC shows seven modes at 1464, 1452, 1375, 1064, 1058, 1015 and 956 cm<sup>-1</sup> that are insensitive to metal substitution, methine deuteration and a change in peripheral substituents and are therefore assigned to ethyl group vibrations. These modes are not observed in the resonance Raman spectra except for the 1464 cm<sup>-1</sup> mode that is present in nearly all of the resonance Raman spectra of the chlorin complexes that we have examined. The chlorin macrocycle does not influence the internal vibrations of the ethyl groups since the frequencies are all close to the values

reported by Kincaid et al. (100) from the IR spectrum of NiOEP in an argon matrix.

#### 4. Conclusions

From our analysis of the resonance Raman and IR spectra of the MOEC complexes we have shown that the high frequency vibrational modes of metallochlorins cannot be assigned by direct comparison with the normal modes of metalloporphyrins. The normal coordinate analysis of NiOEC performed by Boldt et al. therefore represents the starting point for the description of the vibrational modes of metallochlorins. In the work presented here, the mode compositions deduced for metallochlorins by metal substitution, methine deuteration and a change in the peripheral substituents of OEC have been compared with the assignments proposed by Boldt et al. The overall agreement is fairly good although several mode assignments need to be modified in the normal coordinate analysis.

The agreement between our results and the normal coordinate analysis of Boldt et al. is especially gratifying considering that it is the first normal coordinate treatment of a metallochlorin. The wealth of information obtained from the resonance Raman spectra of metalloporphyrins and hemoproteins has been possible largely because of the accepted



set of mode assignments based on the normal coordinate analysis of NiOEP published by Abe et al. in 1978 (55). However, several other groups have also performed normal coordinate treatments for metalloporphyrins (109-116): the first, by Ogoshi et al. (109) appearing in 1972. Even now there is not complete agreement on metalloporphyrin normal mode assignments, especially for the IR active  $E_u$  modes. Recent years have seen new normal coordinate analyses that have attempted to include the peripheral substituents in the calculations (115,116). Similarly, further normal coordinate treatments for metallochlorins can be expected. We hope that our results for CuOEC and the methine-deuterated CuOEC complexes will provide the basis for a new normal coordinate analysis to improve the vibrational mode assignments for metallochlorins.

## CHAPTER 4

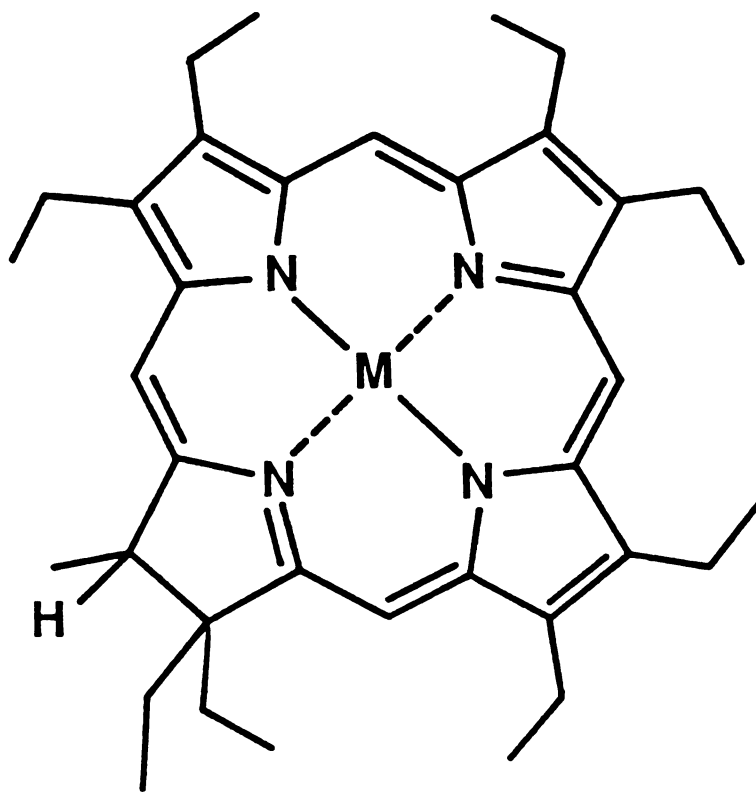
### VIBRATIONAL PROPERTIES OF METALLOCHLORIN $\pi$ CATION RADICALS

#### 1. Introduction

In photosynthesis, the primary charge separation event occurs at the reaction center chlorophylls P-700 of Photosystem I (4) and P-680 of Photosystem II (5). In this process, an electron is removed from the  $\pi$  system of the chlorophyll macrocycle resulting in the formation of a chlorophyll  $\pi$  cation radical. P-700 is thought to have a dimeric structure in the ground neutral state but in the oxidized state, P-700<sup>+</sup> the unpaired electron appears to be localized on one of the two chlorophylls (11-14). Lutz compared the resonance Raman spectra of the bacteriochlorophyll a cation radical in solution and in the reaction center, P-870 of Rhodopseudomonas sphaeroides (117). It was concluded that the positive charge is localized on one of the two bacteriochlorophylls of P-870<sup>+</sup> on the time scale of the resonance Raman effect ( $\sim 10^{-13}$  s). Establishment of the vibrational properties of metallochlorin  $\pi$  cation radicals is essential if resonance Raman spectroscopy is to be used to characterize the reaction center chlorophylls.

The vibrational properties of metalloporphyrin  $\pi$  cation radicals have been characterized by resonance Raman spectroscopy in this lab by T. Oertling and A. Salehi (99, 118-120). The results from these studies showed similar potential energy distributions in the normal modes for both the neutral and oxidized MOEP species. In other words, the mode compositions do not change upon oxidation of the porphyrin macrocycle. The frequencies of the  $C_bC_b$  stretching modes were observed to increase, while those of the  $C_aC_m$  and  $C_aN$  stretching modes decreased. In collaboration with these authors, preliminary results of the investigation into the resonance Raman spectral characteristics of metallochlorin  $\pi$  cation radicals have been reported (121).

The  $\pi$  cation radicals of metallo-methyloctaethylchlorin (MMeOEC) (Figure 4.1) were chosen for the initial resonance Raman study. These compounds do not have vicinal protons on the reduced ring (122) so that oxidative dehydrogenation back to the porphyrin is not possible. The resonance Raman spectra of the Cu, Co and Ni complexes of MeOEC show two modes in the 1500-1520 and 1620-1650  $\text{cm}^{-1}$  regions that appeared to be analogous to the  $C_aC_m$  stretching modes  $\nu_3$  and  $\nu_{10}$ , respectively of metalloporphyrins (121). Upon oxidation of the chlorin ring, the  $\nu_{10}$ -like mode shifted by  $-10 \text{ cm}^{-1}$  but the  $\nu_3$ -like mode exhibited a slight increase in frequency. The K values for the  $\nu_{10}$ -like mode indicated  $C_aC_m$  stretching character in both MMeOEC ( $K=385$ ) and  $\text{MMeOEC}^+$  ( $K=375$ ). The decrease in frequency



**MMeOEC**  
**M = Co, Cu, Ni**

**Figure 4.1 Structure of metallo-methyloctaethylchlorin (MMeOEC)**

upon oxidation for the  $\nu_{10}$ -like mode is consistent with the results of Oertling *et al.* (120) for a  $C_4C_{10}$  mode of MOEP. The lower K value and increase in frequency upon oxidation suggested that the  $\nu_3$ -like mode of MMeOEC consisted of mixed  $C_4C_{10}$  and  $C_bC_b$  stretching character. In MMeOEC<sup>+</sup> it was proposed that the frequency increase from the  $C_bC_b$  character offsets the frequency decrease from the  $C_4C_{10}$  character (121).

The study of the  $\pi$  cation radicals of MMeOEC was performed before the analysis of the vibrational mode characteristics of the MOEC complexes had been completed. To explore further the vibrational properties of metallochlorin  $\pi$  cation radicals, the resonance Raman spectra of the  $\pi$  cation radicals of CuOEC, CuECI (Figure 3.1) and the methine-deuterated CuOEC complexes (CuOEC- $\alpha,\beta$ -d<sub>2</sub>, CuOEC- $\gamma,\delta$ -d<sub>2</sub> and CuOEC-d<sub>4</sub>) are presented in this Chapter. Comparison of the spectra of the  $\pi$  cation radicals with those of the neutral species shows that our initial interpretation requires modification and that unlike the situation in metalloporphyrins, changes in mode composition occur upon oxidation of metallochlorins.

## 2. Results

Metallochlorins were oxidized chemically at room temperature by using the  $\text{AgClO}_4/\text{CH}_2\text{Cl}_2$  method described by Salehi *et al.* (118). The electronic absorption spectrum of  $\text{CuOEC}^+$  in  $\text{CH}_2\text{Cl}_2$  solution is shown in Figure 4.2. The spectrum displays a split Soret band and a disappearance of the visible bands.

Resonance Raman spectra of  $\text{CuOEC}$ ,  $\text{CuECI}$ ,  $\text{CuOEC-}\alpha,\beta\text{-d}_2$ ,  $\text{CuOEC-}\gamma,\delta\text{-d}_2$  and  $\text{CuOEC-d}_4$  and their  $\pi$  cation radicals were obtained with Soret excitation by using the 363.8 nm line from a Coherent Innova 100-20  $\text{Ar}^+$  laser. Spectra were recorded by T. Oertling on a Spex 1877 triple monochromator equipped with OMA III electronics. Figure 4.3 shows the resonance Raman spectra of the neutral copper chlorin complexes in  $\text{CH}_2\text{Cl}_2$  solution. The resonance Raman spectra of the corresponding  $\pi$  cation radicals are shown in Figure 4.4. In the high frequency region, the 1642, 1601, 1582, 1547 and 1507  $\text{cm}^{-1}$  modes of  $\text{CuOEC}$  are replaced by another set of modes at 1632, 1611, 1605, 1560 and 1511  $\text{cm}^{-1}$  in  $\text{CuOEC}^+$ .

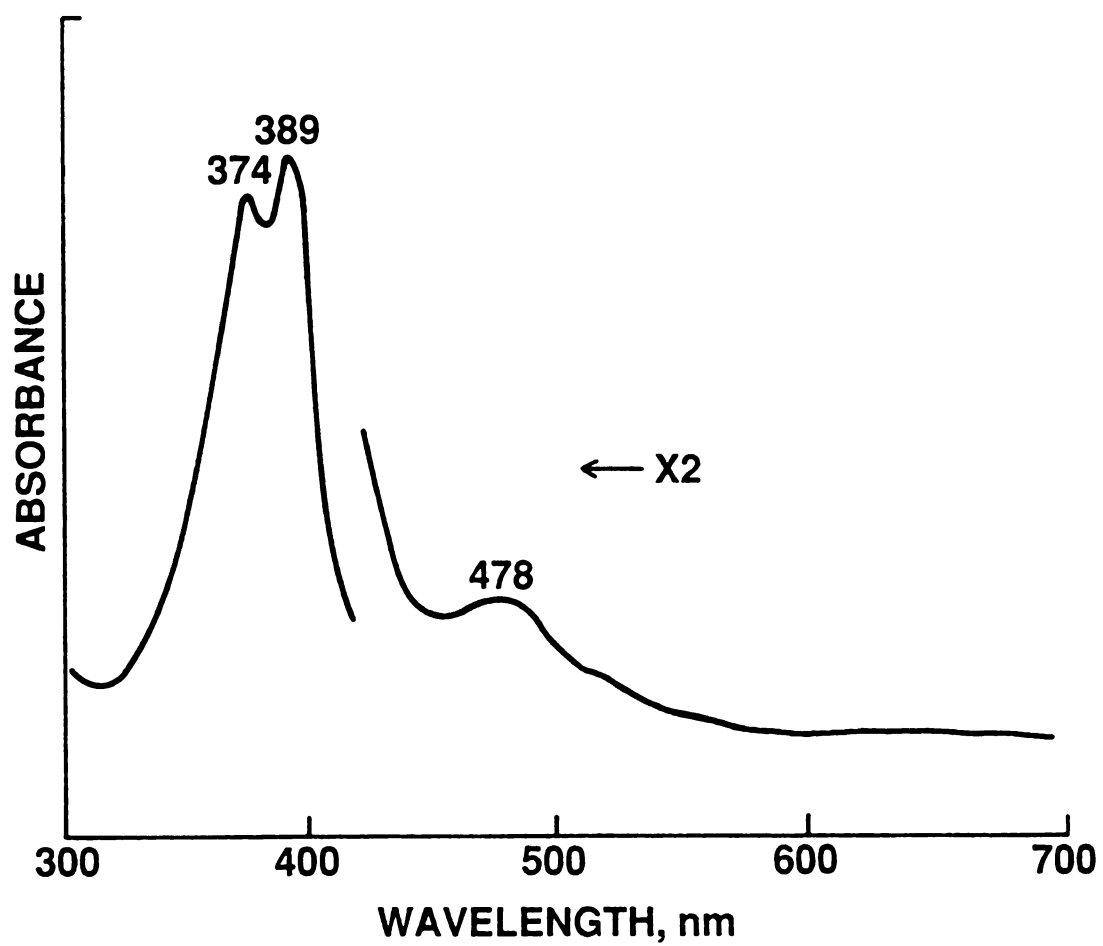


Figure 4.2 Electronic absorption spectrum of  $\text{CuOEC}^+$  in  $\text{CH}_2\text{Cl}_2$  solution

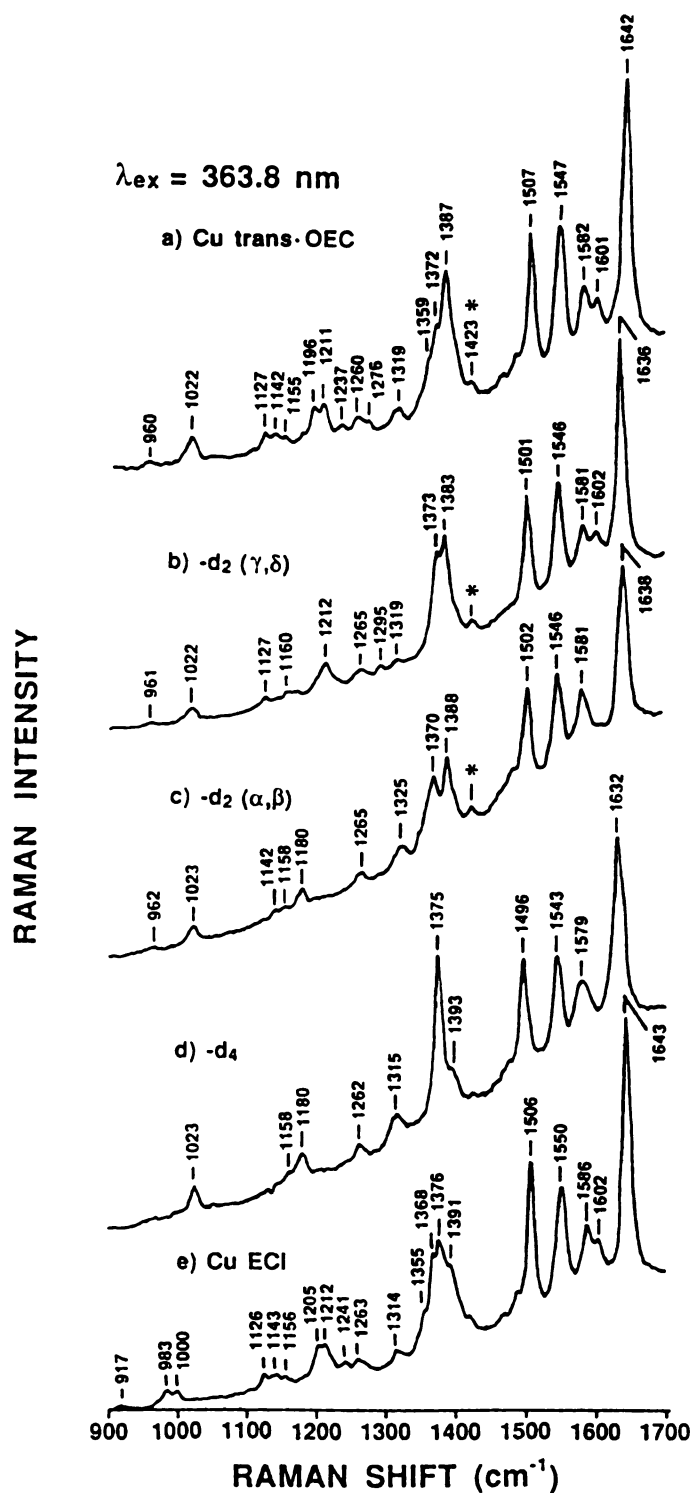


Figure 4.3 Resonance Raman spectra of CuOEC, CuOEC- $\gamma, \delta$ -d<sub>2</sub>, CuOEC- $\alpha, \beta$ -d<sub>2</sub>, CuOEC-d<sub>4</sub>, and CuECI in CH<sub>2</sub>Cl<sub>2</sub> solution obtained with Soret excitation at 363.8 nm



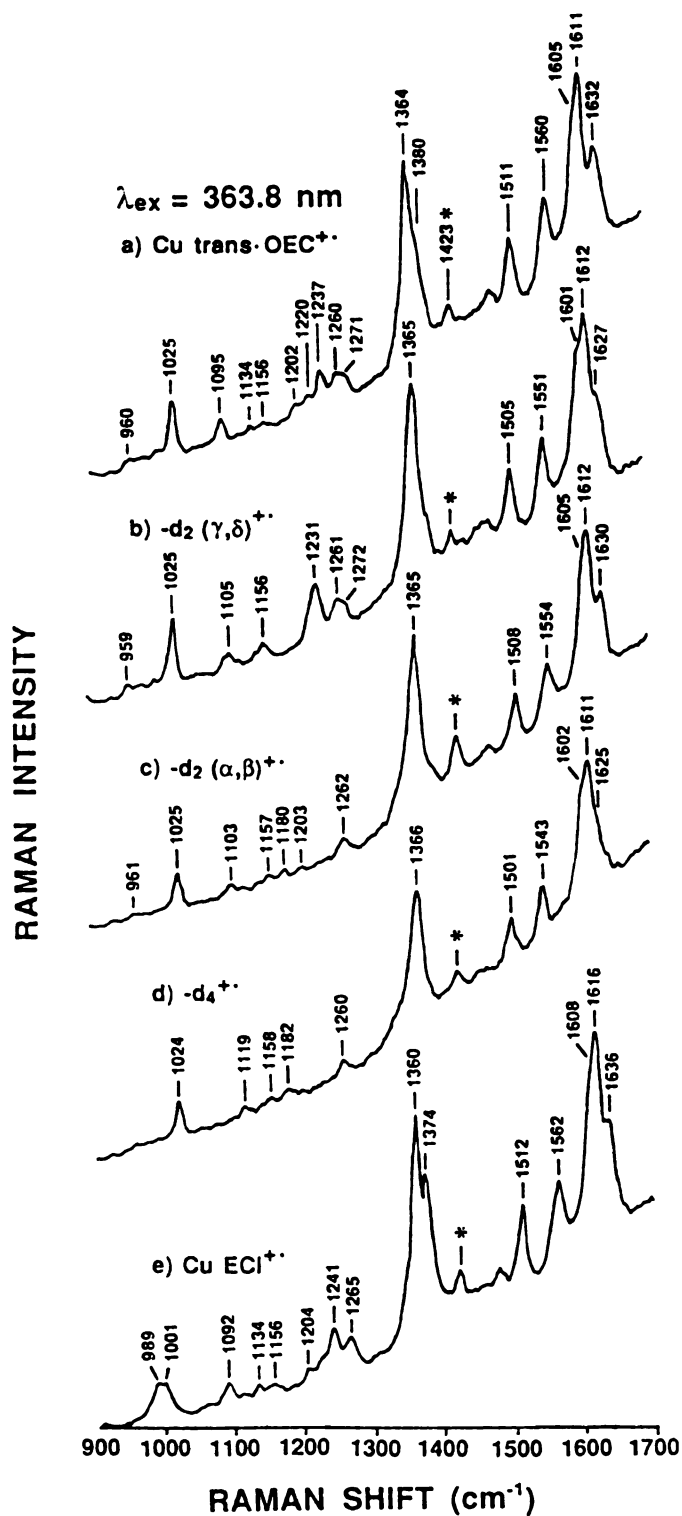


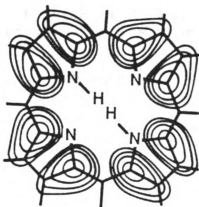
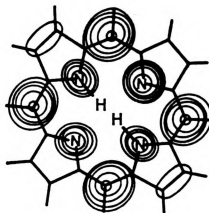
Figure 4.4 Resonance Raman spectra of CuOEC<sup>+</sup>, CuOEC- $\gamma, \delta$ -d<sub>2</sub><sup>+</sup>, CuOEC- $\alpha, \beta$ -d<sub>2</sub><sup>+</sup>, CuOEC-d<sub>4</sub><sup>+</sup> and CuECI<sup>+</sup> in CH<sub>2</sub>Cl<sub>2</sub> solution obtained with Soret excitation at 363.8 nm

### 3. Discussion

In their study of metalloporphyrin  $\pi$  cation radicals, Oertling et al. were able to directly correlate the resonance Raman modes of MOEP with those of MOEP<sup>+</sup>. The K values for the  $\nu_2$ ,  $\nu_3$ ,  $\nu_{10}$  and  $\nu_{11}$  modes in MOEP and MOEP<sup>+</sup> are very close indicating similar mode compositions in both the neutral and oxidized species (120). Assignments of the other high frequency modes of MOEP<sup>+</sup> were achieved by comparison of the frequency shifts following methine deuteration and a change of peripheral substituents from OEP to EPI (99).

The HOMO's of metalloporphyrins consist of an  $a_{1u}$  orbital and an  $a_{2u}$  orbital (41,42). Figure 4.5(a) shows the electron density contour maps for the  $a_{1u}$  and  $a_{2u}$  orbitals of free base porphine from the M.O. calculations by Spangler et al. (123). In the  $a_{1u}$  orbital, electron density is located on the  $C_aC_b$  bonds whereas in the  $a_{2u}$  orbital, electron density is centered on the  $C_m$  and nitrogen atoms. From these diagrams, Oertling et al. predicted that formation of the  ${}^2A_{1u}$  state metalloporphyrin  $\pi$  cation radical (by removal of an electron from the  $a_{1u}$  orbital) should result in decreased frequencies of the  $C_aC_m$ ,  $C_aC_b$  and  $C_aN$  stretching modes and increased frequencies of the  $C_bC_b$  stretching modes (Table 4.1). On the other hand, formation of the  ${}^2A_{2u}$  state  $\pi$  cation radicals would produce lower frequencies for the  $C_aC_m$  and  $C_bC_b$  modes and higher frequencies for the  $C_aC_b$  and  $C_aN$  modes. The pattern of

## a) Free Base Porphine

 $a_{1u}$  $a_{2u}$ 

## b) Free Base Chlorin

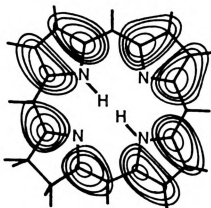
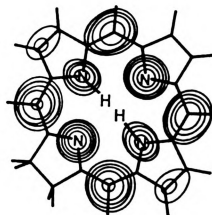
 $a_{1u}$  $a_{2u}$ 

Figure 4.5 Electron density contour maps for the  $a_{1u}$  and  $a_{2u}$  orbitals of a) free base porphine and b) free base chlorin (from ref. 123)

frequency shifts observed for MOEP upon oxidation is consistent with the  $^2A_{1u}$  ground state for MOEP $^{+}$ .

Table 4.1 Predicted and observed frequency shifts for porphyrin normal modes upon oxidation (from ref.99)

	Predicted		Observed	$\Delta\nu_{ox}$
	$^2A_{1u}$	$^2A_{2u}$	for MOEP	CuOEP
$\nu C_a C_m$	-	-	-	$\nu_{10}(-6), \nu_3(-4)$
$\nu C_a C_b$	-	+	-	$\nu_{29}(-14)$
$\nu C_a N$	-	+	-	$\nu_4(-17)$
$\nu C_b C_b$	+	-	+	$\nu_2(+24), \nu_{11}(+34)$

The  $a_{1u}$  and  $a_{2u}$  orbitals of free base chlorin (Figure 4.5) are almost identical to those of porphine except for the region around ring IV in the  $a_{1u}$  orbital. Electron density shifts from the  $C_a C_b$  bonds in the  $a_{1u}$  orbital of porphine onto the  $\gamma, \delta$   $C_a C_m$  bonds adjacent to ring IV of chlorin. EPR measurements show that chlorin  $\pi$  cation radicals have unpaired spin density at the  $C_a$  positions as a result of removal of an electron from the  $a_{1u}$  orbital (124). Therefore, metallochlorin resonance Raman modes are expected to show the same pattern of frequency shifts as for MOEP, namely, decreases in frequency for the  $C_a C_m$ ,  $C_a C_b$  and  $C_a N$  modes and increases in frequency for the  $C_b C_b$  modes. In addition, metallochlorin  $\gamma, \delta$  localized  $C_a C_m$  stretching modes are predicted to show a larger decrease in frequency compared to metalloporphyrins since the

$C_aC_m$  interactions are non-bonding in the porphyrin  $a_{1u}$  orbital but bonding in the ring IV  $\gamma, \delta$  methines of the chlorin  $a_{1u}$  orbital.

If it is assumed that the resonance Raman modes of  $CuOEC^{+ \cdot}$  can be directly correlated with those of CuOEC then the high frequency modes of CuOEC/ $CuOEC^{+ \cdot}$  may be assigned as in Table 4.2. The  $1642\text{ cm}^{-1}$  mode of CuOEC decreases in frequency by  $10\text{ cm}^{-1}$  upon oxidation and is therefore predicted to have  $C_aC_m$  stretching character. The 1601, 1582 and  $1547\text{ cm}^{-1}$  modes of CuOEC all show substantial frequency shifts of +10, +23 and  $+13\text{ cm}^{-1}$ , respectively, in  $CuOEC^{+ \cdot}$ .  $C_bC_b$  stretching character is predicted for these three modes. Compared to CuOEP, the decrease in frequency of the  $1642\text{ cm}^{-1}$   $C_aC_m$  stretching mode of CuOEC is larger whereas the frequency increases for the  $C_bC_b$  stretching modes of CuOEC are smaller. Using the same argument as for MMeOEC, the slight  $4\text{ cm}^{-1}$  increase in frequency of the  $1507\text{ cm}^{-1}$  mode of CuOEC can be attributed to mixed  $C_aC_m$  and  $C_bC_b$  stretching character (121). However, for the 1601 and  $1507\text{ cm}^{-1}$  modes of CuOEC the mode characters predicted from the oxidation shifts do not agree with the previously determined mode assignments.

Table 4.2 Mode characters predicted for CuOEC/CuOEC<sup>+</sup>.

CuOEC	CuOEC <sup>+</sup>	Predicted character	Assignment*
1642	1632	$\nu C_a C_m$	$\nu C_a C_m(\gamma, \delta), \nu C_a C_m(\alpha, \beta)$
1601	1611	$\nu C_b C_b$	$\nu C_a C_m(\alpha, \beta)$
1582	1605	$\nu C_b C_b$	$\nu C_b C_b, \nu C_a C_m(\alpha, \beta, \gamma, \delta)$
1547	1560	$\nu C_b C_b$	$\nu C_b C_b$
1507	1511	$\nu C_a C_m, \nu C_b C_b$	$\nu C_a C_m(\alpha, \beta, \gamma, \delta)$

\* From Table 3.4

The frequency shifts resulting from selective methine deuteration and a change in peripheral substituents of the  $\pi$  cation radicals may be compared to those of the neutral species. A shift to lower frequency upon methine deuteration is indicative of  $C_a C_m$  stretching character in a given mode and the use of selective methine deuteration at the  $\alpha, \beta$  and  $\gamma, \delta$  positions reveals the extent of mode localization.  $C_b C_b$  stretching character is indicated by an increase in frequency for a given mode upon the change of peripheral substituents from OEC to ECI. Table 4.3 summarizes the shifts for the high frequency resonance Raman modes of CuOEC and CuOEC<sup>+</sup>. The 1642/1632  $\text{cm}^{-1}$  pair of modes of CuOEC/ CuOEC<sup>+</sup> show a change from  $C_a C_m$  stretching with an unequal localization in the  $\gamma, \delta$  and  $\alpha, \beta$  methines in the neutral species to mixed  $\gamma, \delta$  localized  $C_a C_m$  and  $C_b C_b$  stretching upon oxidation. Similarly, the 1582/1605 and 1507/1511  $\text{cm}^{-1}$  pairs show reduced  $\alpha, \beta$  localized  $C_a C_m$

Table 4.3 Vibrational frequencies ( $\text{cm}^{-1}$ ) and isotope shifts ( $\text{cm}^{-1}$ ) for the high frequency resonance Raman modes of CuOEC and CuOEC<sup>+</sup>.

CuOEC	CuOEC <sup>+</sup>	$\Delta\nu$ $\alpha, \beta$	$\Delta\nu$ $\gamma, \delta$	$\Delta\nu$ $d_4$	$\Delta\nu$ subst	Assignment
1642		-4	-6	-10	+1	$\nu C_s C_m(\gamma, \delta), \nu C_s C_m(\alpha, \beta)$
	1632	-2	-5	-7	+4	$\nu C_s C_m(\gamma, \delta), \nu C_b C_b$
1601		-11	+1	-15	+1	$\nu C_s C_m(\alpha, \beta)$
	1611	+1	+1	0	+5	$\nu C_b C_b$
1582		-1	-1	-3	+4	$\nu C_b C_b, \nu C_s C_m(\alpha, \beta, \gamma, \delta)$
	1605	0	-4	-3	+3	$\nu C_b C_b, \nu C_s C_m(\gamma, \delta)$
1547		-1	-1	-4	+3	$\nu C_b C_b$
	1560	-6	-9	-17	+2	$\nu C_s C_m(\alpha, \beta, \gamma, \delta), \nu C_b C_b$
1507		-5	-6	-11	-1	$\nu C_s C_m(\alpha, \beta, \gamma, \delta)$
	1511	-3	-6	-10	+1	$\nu C_s C_m(\gamma, \delta), \nu C_s C_m(\alpha, \beta), \nu C_b C_b$

stretching character with an increased contribution from  $C_bC_b$  stretching. Substantial changes in mode composition occur for the 1601/1611 and 1547/1560  $\text{cm}^{-1}$  pair so that it is unlikely that a direct correlation exists between these modes in the neutral and oxidized species. The 1601  $\text{cm}^{-1}$  mode of CuOEC is an  $\alpha, \beta$  localized  $C_aC_m$  stretching mode for which a frequency shift of approximately  $-5 \text{ cm}^{-1}$  would be predicted in the  $\pi$  cation by analogy with the results for MOEP. If the 1601  $\text{cm}^{-1}$  mode is compared to the 1560  $\text{cm}^{-1}$  mode of  $\text{CuOEC}^{+\cdot}$  then the same trend of reduction of  $\alpha, \beta$  localized  $C_aC_m$  character and gain of  $C_bC_b$  character is maintained but the  $-40 \text{ cm}^{-1}$  shift is much larger than any shift previously observed. This would leave the 1547  $\text{cm}^{-1}$   $C_bC_b$  stretching mode of CuOEC to correlate with the 1611  $\text{cm}^{-1}$   $C_bC_b$  mode of  $\text{CuOEC}^{+\cdot}$ : an increase of  $+64 \text{ cm}^{-1}$ . However, what is probably more important here is not direct correlation of modes but the overall pattern of increased  $\gamma, \delta$  localized  $C_aC_m$  and  $C_bC_b$  character in  $\text{CuOEC}^{+\cdot}$ .



#### 4. Conclusions

Significant differences exist between the vibrational properties of metallochlorins and metalloporphyrins. Reduction of a  $C_bC_b$  bond in a metalloporphyrin to form a metallochlorin has a far greater effect than a mere lowering of molecular symmetry. Unlike metalloporphyrins, the neutral MOEC complexes show mode localization and mixing of  $C_aC_a$  and  $C_bC_b$  stretching character. The structural changes in metallochlorins prevent a direct correlation of the normal modes of MOEP with those of MOEC. Now, in the metallochlorin  $\pi$  cation radicals, changes in mode composition occur upon ring oxidation.

From their study of the  $\pi$  cation radicals of MOEP, Oertling et al. concluded that the mode compositions of metalloporphyrins did not change upon oxidation. These authors also concluded that there were no significant changes in ring geometry for metalloporphyrins and their  $\pi$  cation radicals in solution (125). It is possible that the altered mode compositions of  $CuOEC^+$  result from a further change in molecular geometry. Unfortunately, X-ray crystal structures of metallochlorin  $\pi$  cation radicals are not available to support this idea. In addition, with a crystal structure it would be possible to perform a normal coordinate analysis to assign the vibrational modes of metallochlorin  $\pi$  cation radicals.

The preponderance of  $\gamma, \delta$  localized  $C_\alpha C_\beta$  stretching modes in the chlorin  $\pi$  cation radicals is puzzling. The M.O. diagrams of the  $a_{1u}$  orbitals of porphine and chlorin would suggest similar behavior for the  $\alpha, \beta$  localized  $C_\alpha C_\beta$  modes in chlorin and delocalized porphyrin  $C_\alpha C_\beta$  modes but there are no  $\alpha, \beta$  localized modes observed in  $CuOEC^+$ . Chlorin  $\pi$  cation radicals are presumed to have  $a_{1u}$  orbital character but the radicals may result from a mixture of the  $a_{1u}$  and  $a_{2u}$  orbitals. Further EPR and ENDOR studies of metallochlorin  $\pi$  cation radicals would help to establish the distribution of spin density in these species.

## CHAPTER 5

### VIBRATIONAL PROPERTIES OF METALLOCHLOROPHYLLS

#### 1. Introduction

The study of the IR and resonance Raman spectra of metallo-octaethylchlorin model compounds is part of a broader effort to interpret the spectra of naturally-occurring metallochlorins. Chlorophylls are metallochlorins that play a crucial role in the process of photosynthesis in higher plants. The structural complexities introduced into the chlorophyll molecule by the chlorin macrocycle, the additional ring V and the peripheral substituents require the use of the simpler symmetric MOEC complexes in order to understand the resonance Raman spectra of chlorophyll.

The first resonance Raman spectra of chlorophyll a and chlorophyll b were reported by Lutz in 1972 (68). This is the same year in which resonance Raman spectra of several hemoglobin derivatives were published (131-133). Throughout the 1970's and 80's resonance Raman studies by many groups have greatly advanced the area of metalloporphyrin and hemoprotein chemistry. However, it was not until 1979 that the

first resonance Raman spectra of metallochlorin model compounds were reported (95) and 1986 before serious attempts were made to determine the characteristics of the vibrational modes of the chlorophylls (83,134,135). Table 5.1 lists the chlorophylls and chlorophyll-derivatives for which resonance Raman spectra have been reported. In addition to the chlorophylls listed in Table 5.1, resonance Raman spectra of the chlorophyll a cation radical (136), bacteriochlorophyll a (117,137-140) and its cation radical (117,138,139), and chlorophylls  $c_1 + c_2$  (141) have been reported.

Approximately 50 modes are observed in the 50-1750  $\text{cm}^{-1}$  region in the resonance Raman spectra of chlorophyll with Soret excitation. By comparison with the IR spectra of chlorophyll a and chlorophyll b, Lutz identified the resonance Raman bands for the keto carbonyl stretching vibration of both molecules at 1690  $\text{cm}^{-1}$  and the formyl carbonyl stretching vibration of chlorophyll b at 1670  $\text{cm}^{-1}$  (70). No evidence for a vinyl stretching mode was found: the resonance Raman spectrum of chlorophyll d (where the vinyl group has been oxidized to a formyl group) showed no difference between those of chlorophyll a and chlorophyll b in the 1620  $\text{cm}^{-1}$  region (71). Resonance Raman modes involving motion of the central magnesium and pyrrole nitrogen atoms in chlorophyll a and chlorophyll b were identified by Lutz et al. in the low frequency region around 300  $\text{cm}^{-1}$  by  $^{26}\text{Mg}$  and  $^{15}\text{N}$  isotopic substitution (72). However, the majority of the vibrational

Table 5.1 Chlorophylls and chlorophyll-derivatives for which resonance Raman spectra have been reported

Chlorophyll	M	R <sub>2</sub> <sup>a</sup>	R <sub>3</sub> <sup>a</sup>	R <sub>10</sub> <sup>a</sup>	R <sub>7c</sub> <sup>a</sup>	ref.
chl a	Mg	CH=CH <sub>2</sub>	CH <sub>3</sub>	CO <sub>2</sub> CH <sub>3</sub>	C <sub>20</sub> H <sub>39</sub>	76, *
pheo a	H <sub>2</sub>	CH=CH <sub>2</sub>	CH <sub>3</sub>	CO <sub>2</sub> CH <sub>3</sub>	C <sub>20</sub> H <sub>39</sub>	76
chl b	Mg	CH=CH <sub>2</sub>	CHO	CO <sub>2</sub> CH <sub>3</sub>	C <sub>20</sub> H <sub>39</sub>	76, *
pheo b	H <sub>2</sub>	CH=CH <sub>2</sub>	CHO	CO <sub>2</sub> CH <sub>3</sub>	C <sub>20</sub> H <sub>39</sub>	76
chl d	Mg	CHO	CH <sub>3</sub>	CO <sub>2</sub> CH <sub>3</sub>	C <sub>20</sub> H <sub>39</sub>	76
pheo d	H <sub>2</sub>	CHO	CH <sub>3</sub>	CO <sub>2</sub> CH <sub>3</sub>	C <sub>20</sub> H <sub>39</sub>	76
pyrochl a	Mg	CH=CH <sub>2</sub>	CH <sub>3</sub>	H	C <sub>20</sub> H <sub>39</sub>	76
2-acetylchl a	Mg	CH <sub>3</sub> CO	CH <sub>3</sub>	CO <sub>2</sub> CH <sub>3</sub>	C <sub>20</sub> H <sub>39</sub>	76
3-oximechl b	Mg	CH=CH <sub>2</sub>	C=NOH	CO <sub>2</sub> CH <sub>3</sub>	C <sub>20</sub> H <sub>39</sub>	76
M chl a	Cu	CH=CH <sub>2</sub>	CH <sub>3</sub>	CO <sub>2</sub> CH <sub>3</sub>	C <sub>20</sub> H <sub>39</sub>	134-5, *
	Ni					134-5, *
	Zn					134-5, *
	Ag					135
Ni MPPh	Ni	C <sub>2</sub> H <sub>5</sub>	CH <sub>3</sub>	H	CH <sub>3</sub>	83
Ni PPh	Ni	CH=CH <sub>2</sub>	CH <sub>3</sub>	H	CH <sub>3</sub>	83

<sup>a</sup> R<sub>2</sub>, R<sub>3</sub>, R<sub>10</sub> and R<sub>7c</sub> are the substituents at the 2, 3, 10 and 7c carbon atoms, respectively, of chlorophyll (see Figure 1.1).

\* This work.

modes involving the chlorophyll macrocycle were not assigned.

Metal substitution of chlorophyll a has been used to identify the core-size sensitive modes (134,135). The results of these studies support the observation that the frequencies of three bands in the 1510-1620  $\text{cm}^{-1}$  region of the resonance Raman spectrum of chlorophyll a could be used to determine the coordination number of the Mg atom (142). In various solvents, bands of chlorophyll a at 1527-1529, 1551-1554 and 1606-1612  $\text{cm}^{-1}$  for 5-coordinated Mg shifted to lower frequency at 1518-1521, 1545-1548 and 1596-1599  $\text{cm}^{-1}$ , respectively, for 6-coordinated Mg.

A second approach to the characterization of the vibrational modes of chlorophyll was undertaken by Boldt et al. who examined a series of nickel chlorins in which the structural complexities of the chlorophyll molecule are added in a stepwise fashion (83). Resonance Raman spectra were recorded for NiOEC, NiDMPPh (DMPPh = 9-deoxo-methylmesopyropheophorbide a), NiMPPh (MPPh = methylmesopyropheobide a) and NiPPh (PPh = methylpyropheophorbide a). In this series of molecules, the chlorin macrocycle, the ring V, the 9-keto carbonyl and the 2-vinyl group are systematically introduced. Normal coordinate calculations showed that the  $\text{C}_\alpha\text{C}_\beta$  and  $\text{C}_\beta\text{C}_\gamma$  stretching modes increase in frequency upon addition of ring V and that many of the modes below 1500  $\text{cm}^{-1}$  retained the same character as in NiOEC.

In this Chapter, the resonance Raman spectra obtained with Soret excitation of chlorophyll a as well as Zn, Cu and Ni-substituted chlorophyll a are presented. The MOEC analysis provides the basis for the interpretation of the resonance Raman spectra of the metallochlorophylls (M chl a). Comparison of the K values for the high frequency modes reveals changes in mode composition on going from MOEC to chlorophyll. The identification of the core-size sensitive modes of M chl a provides a means of distinguishing between 5 and 6-coordination of the Mg of chlorophyll a in different solvents and in vivo.

## 2. Results

### i. Electronic Absorption Spectra

The electronic absorption spectra of chlorophyll a and Zn, Cu and Ni-substituted chlorophyll a in diethyl ether solution are shown in Figure 5.1. The absorption maxima are listed in Table 5.2 together with the ratio of the  $Q_{y00}$  to Soret oscillator strength,  $r$  for each complex. The energies of the transitions follow the order  $Ni > Cu > Zn \approx Mg$  which is the same trend observed for the MOEC complexes. Conjugation of the keto carbonyl on ring V causes a further red-shift of the absorption bands compared to the respective MOEC complex. The oscillator strength ratios, although much higher than for

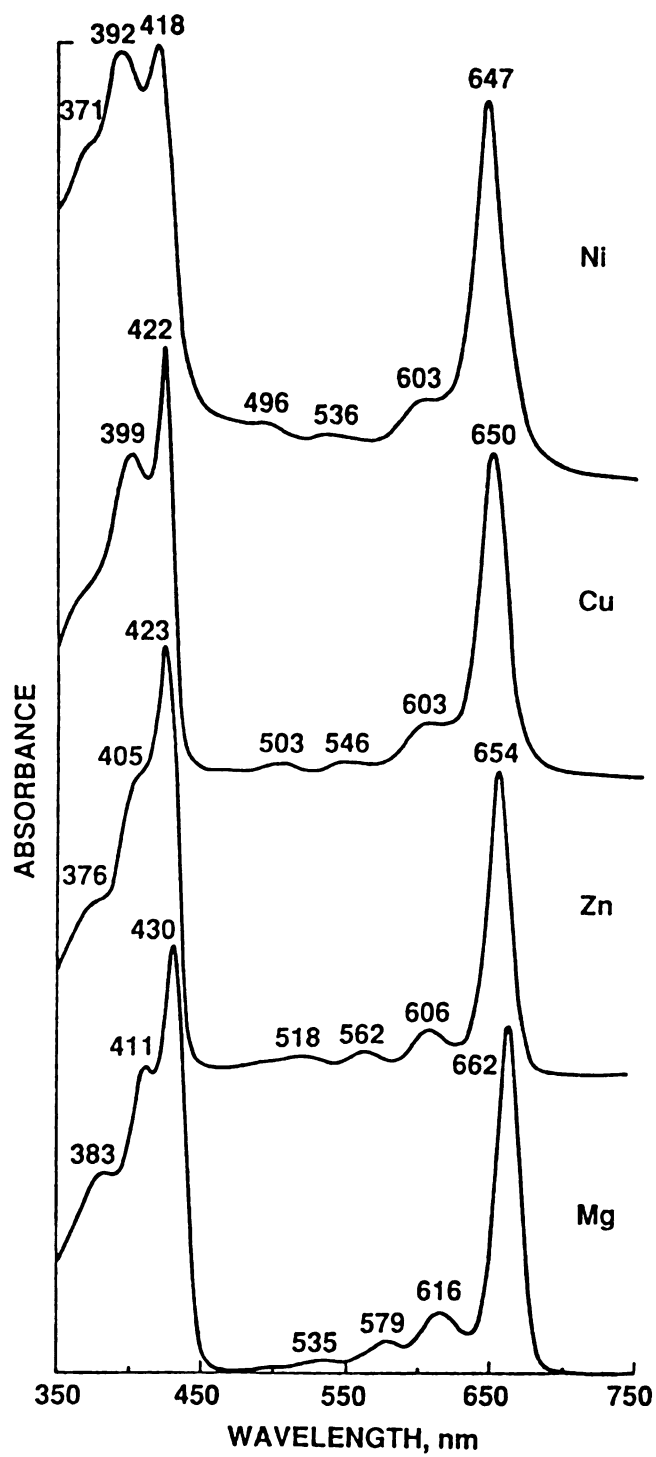


Figure 5.1 Electronic absorption spectra of chlorophyll a and Zn, Cu and Ni-substituted chlorophyll a in diethyl ether solution



MOEC, also follow the order  $\text{Ni} > \text{Cu} > \text{Zn} \approx \text{Mg}$ . Two  $\eta$  bands are observed on the high energy side of the Soret band. These are forbidden in unsubstituted porphyrins but become allowed when there is a conjugated carbonyl substituent on a porphyrin or reduced porphyrin.

Table 5.2 Electronic absorption maxima (nm) for metal-substituted chlorophyll a in diethyl ether solution

Metal	$\eta_2$	$\eta_1$	Soret	$Q_{x01}$	$Q_{x00}$	$Q_{y01}$	$Q_{y00}$	r
Mg	380	409	428	531	575	614	660	0.28
Zn	376	405	423	518	562	606	654	0.25
Cu		399	422	503	546	603	650	0.40
Ni	371	392	418	496	536	590	647	0.53

$$r = f_{Q_{y00}}/f_{\text{Soret}}$$

The electronic absorption spectra of chlorophyll a in acetone, methanol and pyridine solution are shown in Figure 5.2 and the absorption maxima are listed in Table 5.3. The spectra of chlorophyll a in acetone and diethyl ether solution are characteristic of 5-coordinate Mg. In pyridine solution, the Mg of chlorophyll a is 6-coordinate and under these conditions, the  $Q_{x00}$  band shifts to 640 nm. The Mg of chlorophyll a is also 6-coordinate in methanol solution but there is no shift of the  $Q_{x00}$  band. However, the Soret band is lower in intensity and broadened.

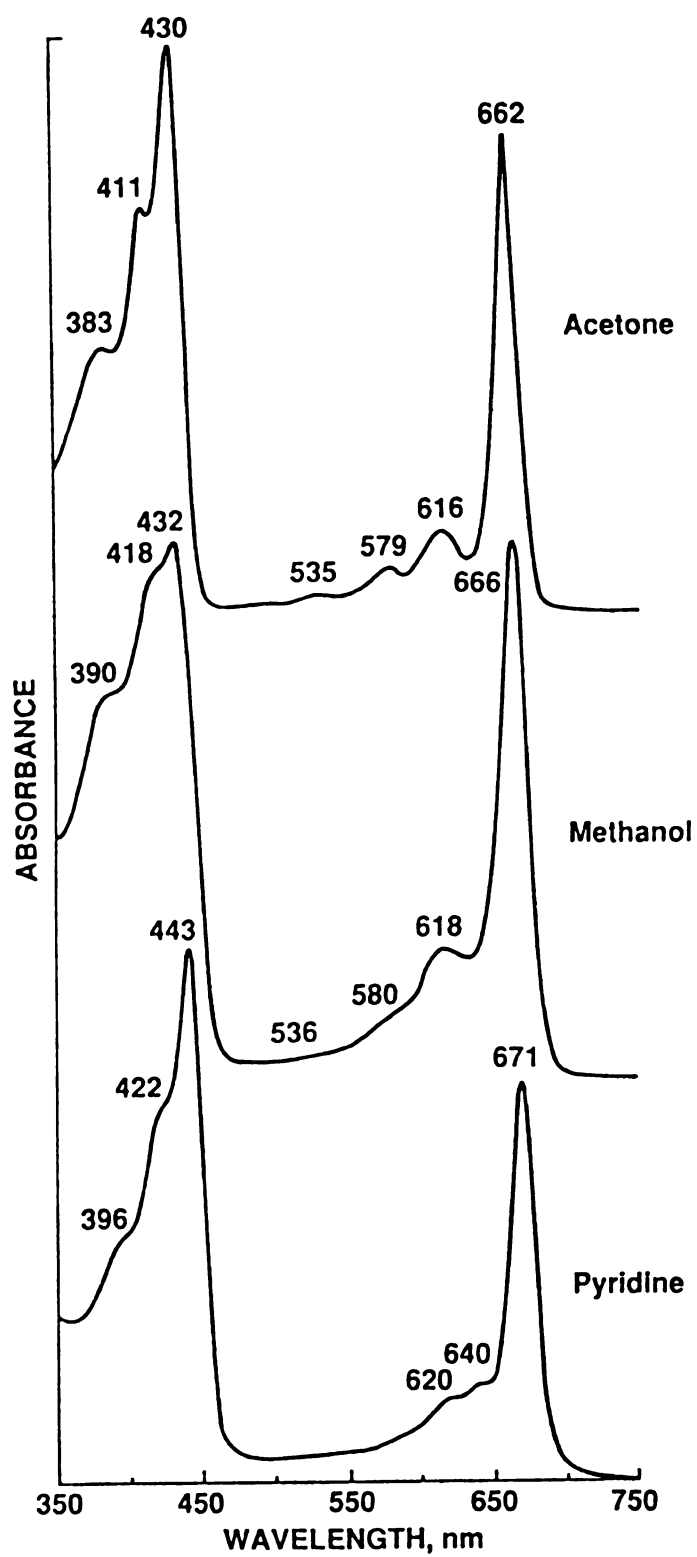


Figure 5.2 Electronic absorption spectra of chlorophyll a in acetone, methanol and pyridine solution

Table 5.3 Electronic absorption maxima (nm) for chlorophyll a in various solvents

Solvent	$\eta_2$	$\eta_1$	Soret	$Q_{x01}$	$Q_{x00}$	$Q_{y01}$	$Q_{y00}$
Diethyl ether	380	409	428	531	575	614	660
Acetone	383	411	430	535	579	616	662
Methanol	390	418	432	536	580	618	666
Pyridine	396	422	443	---	640	620	671

### ii. Resonance Raman Spectra

Figure 5.3 shows the resonance Raman spectra of chlorophyll a and the metal-substituted chlorophyll a complexes obtained with Soret excitation at 406.7 nm. The resonance Raman spectrum of chlorophyll a was recorded in frozen acetone at  $-125^{\circ}\text{C}$ . Spectra of Zn, Cu and Ni chl a were recorded in diethyl ether solution at room temperature. Vibrational frequencies are listed in Table 5.4. Twelve modes of Cu chl a exhibit a core-size dependency. The core-size correlation parameters K and A in the relation  $\nu = K (A - d)$  (62) for these twelve modes in M chl a are also included in Table 5.4.

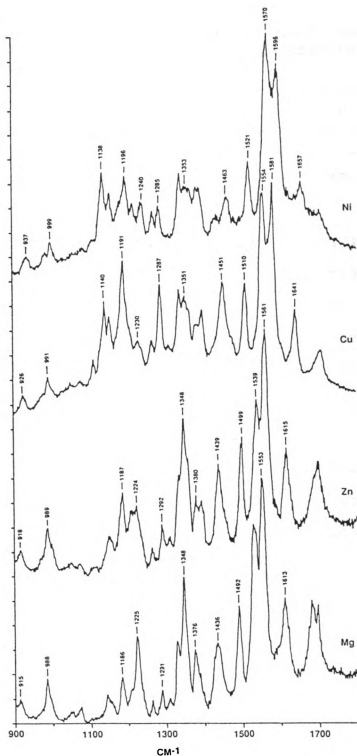


Figure 5.3 Resonance Raman spectra of chlorophyll a in acetone solution and Zn, Cu and Ni-substituted chlorophyll a in diethyl ether solution obtained with Soret excitation at 406.7 nm. Laser powers: 35, 20, 20 and 20 mW, respectively

**Table 5.4 Resonance Raman frequencies ( $\text{cm}^{-1}$ ) and core-size correlation parameters for metal-substituted chlorophyll a**

Mg	Zn	Cu	Ni	K ( $\text{cm}^{-1}/\text{\AA}$ )	A ( $\text{\AA}$ )
1613	1615	1641	1657	470	5.49
1553	1561	1581	1596	429	5.68
1532	1539	1554	1570	373	6.17
1492	1499	1510	1521	279	7.42
1436	1439	1451	1463	274	7.31
-----	1358	1361	1364	67	22.2
1348	1348	1351	1353	54	27.0
1331	1334	1336	1339	71	20.7
1225	1224	1230	1240	158	9.81
1186	1187	1191	1196	101	13.9
988	989	991	999	105	11.5
915	918	926	937	217	6.27

The resonance Raman spectra of chlorophyll a in acetone, pyridine, methanol and diethyl ether solution at  $-125^{\circ}\text{C}$  obtained with Soret excitation at 441.6 nm are shown in Figure 5.4. In the region above  $1450\text{ cm}^{-1}$ , the core-size sensitive modes of chlorophyll a are observed at 1493, 1529, 1553 and  $1616\text{ cm}^{-1}$  in acetone solution. These four modes shift to lower frequencies in pyridine, methanol and diethyl ether solution. The keto carbonyl stretching frequency is also observed to be solvent dependent, occurring at  $1681\text{ cm}^{-1}$  in acetone and pyridine solution,  $1686\text{ cm}^{-1}$  in diethyl ether solution and  $1661\text{ cm}^{-1}$  in methanol solution (see Chapter 6).

### 3. Discussion

In Chapter 3, it was shown how metal substitution could be used to distinguish the amounts of  $\text{C}_a\text{C}_m$  and  $\text{C}_b\text{C}_b$  stretching character in the core-size sensitive vibrational modes for metallo-octaethylchlorin (MOEC) complexes. Comparison of the K values with those for MOEP revealed substantial mixing of  $\text{C}_a\text{C}_m$  and  $\text{C}_b\text{C}_b$  stretching character in the MOEC normal modes. Only the  $1644$  and  $1507\text{ cm}^{-1}$  modes of CuOEC retained similar character to the porphyrin modes  $\nu_{10}$  and  $\nu_3$ , respectively. Although chlorophyll a contains a chlorin macrocycle, the effects of the additional ring V and altered peripheral substitution prohibit a direct comparison of the resonance Raman spectra of chlorophyll a with MOEC.

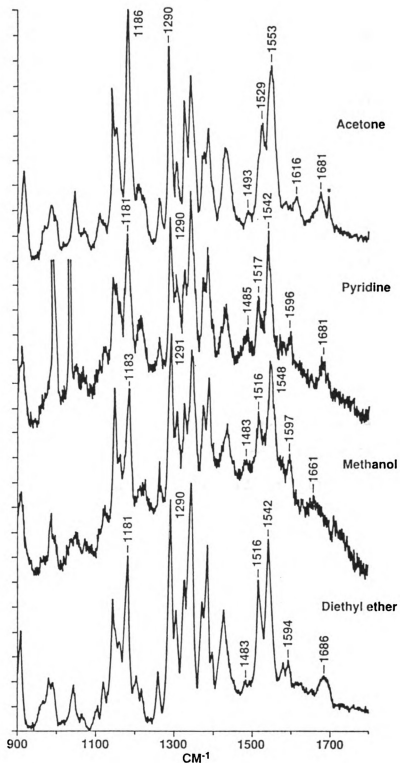


Figure 5.4 Resonance Raman spectra of chlorophyll a in acetone, pyridine, methanol and diethyl ether solution obtained with Soret excitation at 441.6 nm. Laser powers: 20, 15, 15 and 15 mW, respectively

For CuOEC, seven modes in the region above  $1475\text{ cm}^{-1}$  were observed to be core-size sensitive. With Soret excitation, apart from the  $1706\text{ cm}^{-1}$  keto carbonyl stretching mode, Cu chl a shows only four core-size sensitive modes above  $1475\text{ cm}^{-1}$  and a fifth mode at  $1451\text{ cm}^{-1}$ . The very large K values observed for the  $1641$ ,  $1581$  and  $1554\text{ cm}^{-1}$  modes of Cu chl a (Table 5.4) indicate greatly altered mode compositions as a result of the addition of the fifth ring. For the metallochlorophylls, these changes in K values cannot be attributed to a simple increase in the amount of  $\text{C}_\alpha\text{C}_\beta$  stretching character in the normal mode.

The  $1641\text{ cm}^{-1}$  mode of Cu chl a can be correlated with the  $1644\text{ cm}^{-1}$  mode of CuOEC that was assigned to  $\text{C}_\alpha\text{C}_\beta$  stretching with a greater localization in the  $\gamma,\delta$  methines than the  $\alpha,\beta$  methines. In M chl a, the K value for this mode increases to 470 from the 317 value observed in MOEC. The increased core-size sensitivity of this mode is reflected by the fact that the frequency is higher in Ni chl a compared to NiOEC but lower in Zn and Cu chl a compared to the respective MOEC complexes. The large increase in K value may be taken as an indication of further localization into the  $\gamma,\delta$  methines and that the ring V of chlorophyll places a strain on the  $\gamma$  methine bridge for the small core-size of Ni. This interpretation is supported by the results of the normal coordinate analysis by Boldt *et al.* for NiPPh (83). The resonance Raman spectrum of Ni chl a obtained with Soret excitation at  $406.7\text{ nm}$  is similar to the spectrum reported by Boldt *et al.* for



NiPPh in  $\text{Na}_2\text{SO}_4$ . The normal coordinate calculations predict that the  $1658\text{ cm}^{-1}$  mode of NiPPh (which corresponds to the  $1641\text{ cm}^{-1}$  mode of Cu chl a) does indeed have  $\text{C}_\alpha\text{C}_\beta$  stretching character localized in the  $\gamma$  methine bridge. Metal substitution shows that this mode correlates with the  $1615\text{ cm}^{-1}$  mode of chlorophyll a and not the extremely weak  $1630\text{ cm}^{-1}$  mode as assigned by Boldt et al. For the  $1451\text{ cm}^{-1}$  mode of Cu chl a, an assignment of  $\text{C}_\alpha\text{C}_\beta$  stretching character is consistent with the normal coordinate result that the corresponding  $1454\text{ cm}^{-1}$  mode of NiPPh consists of a mixture of a  $\text{CH}_2$  deformation on ring V,  $\gamma, \delta$  localized  $\text{C}_\alpha\text{C}_\beta$  stretching and  $\text{C}_\alpha\text{C}_\gamma$  stretching localized in rings I, II and III. It is also interesting to observe that two other modes, the  $1706\text{ cm}^{-1}$  keto carbonyl stretching mode and the  $1191\text{ cm}^{-1}$  mode of Cu chl a, exhibit a metal dependency. The normal coordinate analysis shows that the keto carbonyl stretching mode is mixed with  $\text{C}_\alpha\text{C}_\beta$  stretching character localized in the  $\gamma$  methine and that the analogue of the  $1191\text{ cm}^{-1}$  mode at  $1188\text{ cm}^{-1}$  in NiPPh contains a contribution from  $\text{C}_\beta\text{C}_{10}$  stretching in ring V.

Difficulties are encountered in trying to reconcile the core-size sensitivity of the other high frequency modes of M chl a with the mode assignments proposed by Boldt et al. for NiPPh. The  $1507\text{ cm}^{-1}$  mode of CuOEC that was assigned to  $\text{C}_\alpha\text{C}_\beta$  stretching delocalized over the macrocycle, correlates with the  $1510\text{ cm}^{-1}$  mode of Cu chl a. The frequencies of this mode are higher for the Zn, Cu and Ni chl a complexes compared to

MOEC. The K value for M chl a is almost the same as in MOEC, indicating that there should still be CaCm stretching character but Boldt et al. assign the corresponding mode of NiPPh at  $1522\text{ cm}^{-1}$  to  $C_4C_6$  stretching localized in rings I and III. The  $1581$  and  $1554\text{ cm}^{-1}$  modes of Cu chl a show no direct relation to any of the MOEC normal modes but are also predicted to have substantial  $C_4C_6$  stretching character based on their K values. Disagreement is again found since the analogous modes of NiPPh at  $1604$  and  $1574\text{ cm}^{-1}$ , respectively, were assigned by Boldt et al. to mixed localized  $C_4C_6$  and  $C_5C_6$  stretching character. By relying on only a single metal (i.e. Ni) it is possible that Boldt et al. were not able to assign these modes correctly. The observation of core-size sensitivity for the high frequency modes does in fact support the normal coordinate analysis which calculates ten modes from  $1467$  to  $1637\text{ cm}^{-1}$  that have some degree of  $C_4C_6$  stretching character.

Identification of the core-size sensitive modes is important because the frequencies can be used to determine the coordination number of the Mg in chlorophyll a. Lutz proposed that the coordination number of the Mg in chlorophyll a, chlorophyll b and bacteriochlorophyll a could be diagnosed based on a Mg-sensitive mode around  $300\text{ cm}^{-1}$  in each of the three molecules (76). 6-coordination in chlorophyll a was indicated by a sharp band at  $320\text{ cm}^{-1}$  with a half-bandwidth of less than  $16\text{ cm}^{-1}$  at 30 K and less than  $24\text{ cm}^{-1}$  at 300 K.

5-coordination was indicated by the presence of an additional shoulder at 302-312  $\text{cm}^{-1}$  with a half-bandwidth of 24  $\text{cm}^{-1}$  or more at 30 K and 25  $\text{cm}^{-1}$  or more at 300 K. These criteria are difficult to apply in practice especially for *in vivo* systems. The core-size sensitive modes of chlorophyll a on the other hand, are easily identifiable and show distinctly different frequencies for 5 and 6-coordination. The X-ray crystal structure of ethyl chlorophyllide a dihydrate (37) shows one water molecule as the ligand to the Mg atom which is 0.39 Å out-of-plane. Conversion to 6-coordination draws the Mg into the plane of the macrocycle thereby expanding the core. A lower set of core-size frequencies will then be observed for 6-coordinate chlorophyll a.

Chlorophyll a in acetone solution has a 5-coordinate Mg and displays resonance Raman bands at 1493, 1529, 1553 and 1616  $\text{cm}^{-1}$  (Figure 5.4). In pyridine solution, the Mg is 6-coordinate and the core-size sensitive bands occur at 1485, 1517, 1542 and 1596  $\text{cm}^{-1}$ . Previously, the shift of the  $Q_{x00}$  band in the electronic absorption spectrum of chlorophyll a to 640 nm in pyridine solution was taken to be a characteristic feature of 6-coordinate Mg (143). However, in methanol solution, the core-size sensitive modes of chlorophyll a are observed at 1483, 1516, 1548 and 1597  $\text{cm}^{-1}$  indicating 6-coordination but there is no distinct 640 nm  $Q_{x00}$  absorption band. These results for chlorophyll a in frozen solution agree with those of Fujiwara and Tasumi from their resonance Raman

study of chlorophyll a in various solvents at room temperature (142). One exception is for chlorophyll a in diethyl ether solution. The room temperature resonance Raman spectrum shows that the Mg is 5-coordinate based on the core-size sensitive frequencies at 1493, 1529, 1554 and 1607  $\text{cm}^{-1}$ . At lower temperature, two ether ligands can bind to the Mg so that the frequencies characteristic of 6-coordination at 1483, 1516, 1542 and 1594  $\text{cm}^{-1}$  are observed in the resonance Raman spectrum at  $-125^{\circ}\text{C}$ .

#### 4. Conclusions

Resonance Raman studies of the chlorophylls have been dominated by the work of Lutz (68-76). However, a major limitation to further progress has been the lack of a consistent set of vibrational mode assignments for chlorophyll. The resonance Raman results obtained by Lutz for chlorophyll in vivo (73-76) are based primarily on a single mode assignment: the keto carbonyl stretching mode. To learn more about the characteristics of the vibrational modes of chlorophyll, metal substitution has been utilized to determine the core-size sensitive modes of chlorophyll a.

Comparison of the frequencies and K values for the core-size sensitive modes of chlorophyll a with those of OEC shows that there are substantial changes in mode character

between the two types of macrocycle. The observed core-size sensitivity of the high frequency modes of chlorophyll a is consistent with the normal coordinate analysis of NiPPH by Boldt et al. (83). An important result of the normal coordinate analysis is the prediction of further mode localization from OEC to chlorophyll. Metal substitution provides information on the C<sub>4</sub>C<sub>5</sub> stretching character of the vibrational modes but does not address the issue of mode localization. This problem could be approached through the study of isotopically-substituted chlorophylls or chlorophylls with different patterns of peripheral substituents. It is clear that the ring V plays a major role in determining the mode characters for chlorophyll. Our understanding of these effects would benefit from data for model porphyrin and chlorin systems containing an additional ring V.

## CHAPTER 6

### RESONANCE RAMAN SPECTROSCOPY OF CHLOROPHYLL-BINDING PROTEINS

#### 1. Introduction

The chlorophylls in plants and bacteriochlorophylls in photosynthetic bacteria are bound to proteins (20,22). One of the advantages of resonance Raman spectroscopy in the study of biological molecules is that this technique may be used to enhance selectively the vibrational spectrum of a chromophore within a protein environment. Lutz and co-workers have obtained resonance Raman spectra of bacteriochlorophyll in the antenna (144-146) and reaction center (117,137,147,148) complexes from photosynthetic bacteria. In addition, resonance Raman spectra of the antenna chlorophylls in chloroplast preparations and in light-harvesting protein complexes have been reported by Lutz (68,69,73-76). In photosynthetic systems, the antenna chlorophylls far outnumber the reaction center chlorophylls. Isolation of reaction center chlorophyll protein complexes from higher plants in which the polypeptides containing the antenna chlorophylls have been stripped away, offers the possibility of using resonance Raman spectroscopy

to characterize the structures of P-680 and P-700 as well as their cation radicals, P-680<sup>+</sup> and P-700<sup>+</sup>.

In the photosynthetic membranes of higher plants the chlorophylls are localized within three major protein complexes: a light-harvesting chlorophyll a/b protein complex (LHC), a Photosystem I complex containing P700 and a Photosystem II complex containing P680. The PS I and PS II complexes contain the reaction center chlorophylls plus antenna chlorophylls. These protein complexes may be isolated by treatment of thylakoid membranes with mild detergents (22).

The function of LHC is to absorb light and transfer the excitation energy to the reaction center chlorophylls. LHC contains approximately 50% of the chlorophyll in a green plant with a chlorophyll a/b ratio of 1.2. There are 4 chlorophyll a, 3-4 chlorophyll b and 1-2 xanthophyll carotenoid molecules per LHC bound to several polypeptides with molecular weights in the 20 to 30 kDa range. Electron micrographs of two-dimensional LHC crystals have been reported (149,150) but these structures provide no information on the arrangement and binding of the chlorophylls in the protein.

Considerable effort has been devoted to isolation of the Photosystem II/oxygen-evolving complex (PS II/OEC) since this is the site of the water-splitting chemistry (151). In the thylakoid membrane there are approximately 400 chlorophylls

for each PS II. Early preparations yielded complexes containing PS II/OEC and LHC with 225 to 250 chlorophylls per PS II (152,153). Non-ionic detergents may be used to strip away the LHC leaving the PS II/OEC core complex with a chlorophyll/PS II ratio of 60 to 1 (92). A proposed arrangement of the polypeptides and electron transfer components in this protein complex is shown in Figure 6.1. The PS II/OEC complex consists of six membrane-bound polypeptides with molecular weights of 47, 43, 34, 32, 10 and 6 kDa as well as three extrinsic polypeptides with molecular weights of 33, 23 and 17 kDa. Cytochrome b-559 is bound by the 10 and 6 kDa polypeptides. The 33, 23 and 17 kDa polypeptides are involved in manganese binding and oxygen evolution. Namba and Satoh (77) have isolated a PS II reaction center consisting of only the 34 and 32 kDa polypeptides (also referred to as D-2 and D-1, respectively) and the cytochrome b-559 polypeptides. This preparation contains 5 chlorophyll a, 2 pheophytin a, 1  $\beta$ -carotene and 1 or 2 cytochrome b-559 molecules per PS II. The homology between the D-1 and D-2 polypeptides and the L and M subunits of the reaction center from purple photosynthetic bacteria suggests that the site of primary charge separation in PS II is located in D-1 and D-2.

While the arrangement of the polypeptides and electron transfer components in the PS II reaction center is still under investigation, procedures have already been developed for the isolation and crystallization of the reaction center



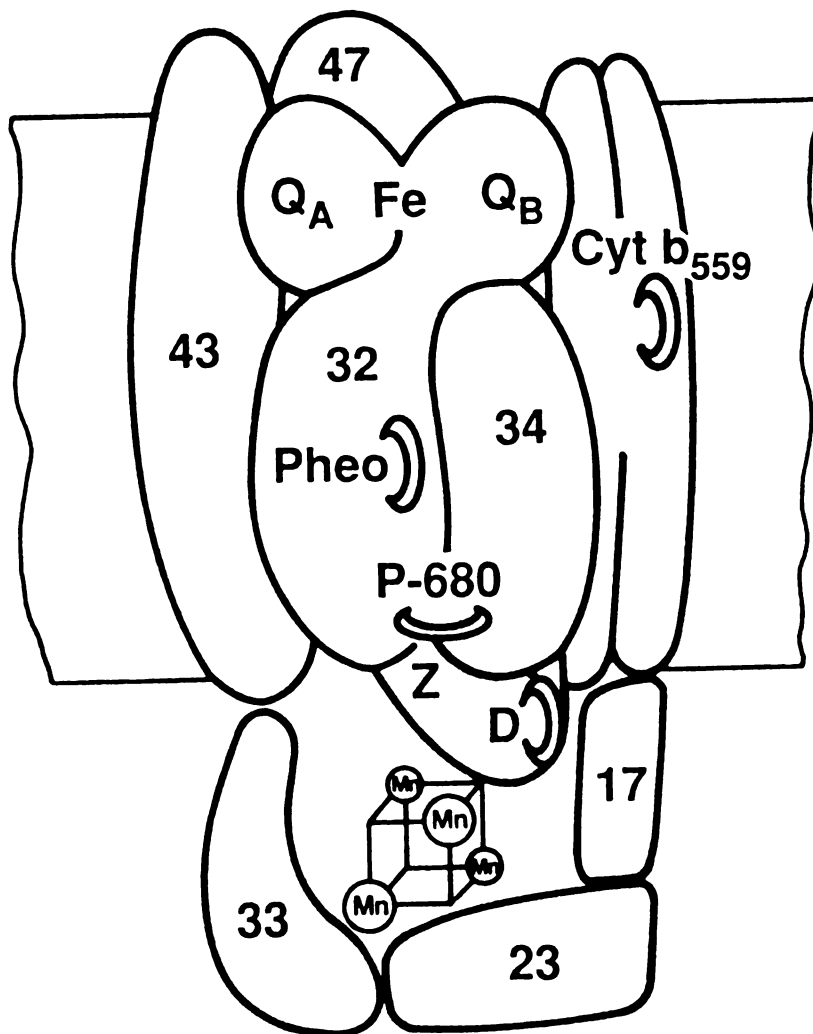


Figure 6.1 Proposed arrangement of the polypeptides and electron transfer components in the PS II/OEC complex (from ref. 154)

complexes from photosynthetic bacteria. Determination of the X-ray crystal structures of the reaction center complexes from Rhodopseudomonas viridis (155-158) and Rhodobacter sphaeroides (159-161) have provided detailed information on the structures and orientations of the pigments in the bacterial reaction center. The reaction center complex from R. viridis contains three protein subunits labelled H, M and L as well as a cytochrome subunit. 4 bacteriochlorophyll b, 2 bacteriopheophytin b, 1 menaquinone ( $Q_A$ ), 1 non-heme iron and 1 ubiquinone ( $Q_B$ ) are located in the L and M subunits. The arrangement of the pigments in the L and M subunits of the reaction center from R. viridis is shown in Figure 6.2. The primary donor consists of two bacteriochlorophyll b molecules overlapping at ring I. There are two branches of bacteriochlorophyll b and bacteriopheophytin b pigments but electron transfer follows only the pathway on the  $Q_A$  side. The X-ray crystal structure also shows that the Mg atoms of the bacteriochlorophylls are 5-coordinate with histidine residues in the L and M subunits serving as the ligands. The crystal structures of the bacterial reaction center have been of enormous importance for understanding the mechanism of primary charge separation in photosynthesis and for providing a model system to test theories of electron transfer.

The electronic absorption spectra of the antenna chlorophyll a molecules in vivo show that the  $Q_y$  band is red-shifted and broadened compared to monomeric chlorophyll

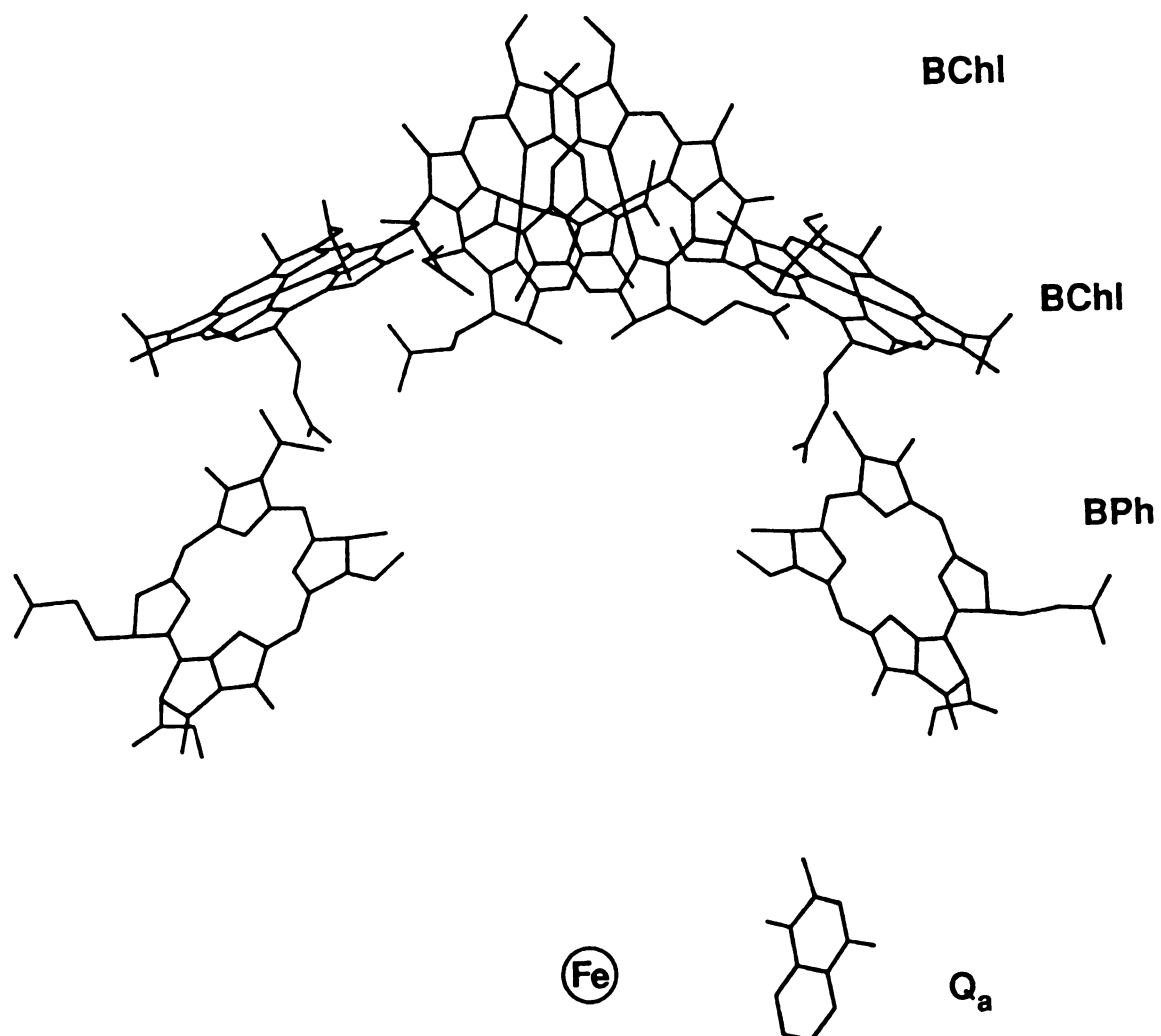
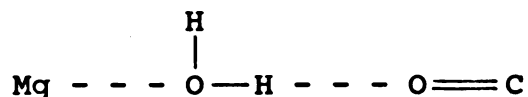


Figure 6.2 Arrangement of pigments in the L and M subunits of the reaction center from *Rhodospseudomonas viridis* (from ref. 158)

a in solution. Broadening of the absorption band can occur by a homogeneous or heterogeneous mechanism. Homogeneous broadening could result from the general protein environment of a chlorophyll a molecule whereas heterogeneous broadening would involve the creation of several distinct chlorophyll a species or protein environments. Simply placing a chlorophyll molecule in a protein environment is not sufficient to account for the spectral changes however. The spectral properties of a series of synthetic Mg and Zn chlorophyllide-apomyoglobin complexes were determined to be within the range observed for solvent effects (162). A red-shift can be produced if there are charged amino acid residues present in the chlorophyll a binding site(s). M.O. calculations predicted shifts of 482 to 740  $\text{cm}^{-1}$  for a point charge placed 3.5 Å above various positions of the chlorophyll macrocycle (163).

The combination of the central magnesium atom acting as an electron acceptor and the keto carbonyl group acting as an electron donor allows for a variety of molecular associations of chlorophyll a with solvent molecules and other chlorophyll a molecules in solution (164). In polar solvents, chlorophyll a is monomeric with one or two solvent molecules bound to the central Mg atom. In non-polar solvents, the carbonyl of one chlorophyll a molecule can coordinate to the Mg atom of a second chlorophyll a thereby forming aggregates. Hydrated polymers of chlorophyll a result from H-bonding to the keto carbonyl of chlorophyll a by a water molecule coordinated to

the Mg of a second chlorophyll a:



It has been proposed that the antenna chlorophylls consist of aggregates (165) and hydrated polymers (37). Other suggestions for chlorophyll a in vivo are chemically modified chlorophyll species, e.g. the enol form of chlorophyll a (15) or a protonated Schiff base linkage of the keto carbonyl (166-169), although none of these has been isolated from chlorophyll-binding proteins.

Support for several different forms of chlorophyll in vivo comes from the work of French et al. (170). These authors used Gaussian components to curve-fit the red absorption band ( $Q_y$ ) measured at  $-196^\circ\text{C}$  for chloroplast preparations from a variety of plants and algae. Four major peaks for chlorophyll a were observed at average wavelengths of 661.6, 669.6, 677.1 and 683.7 nm and two for chlorophyll b at 640.1 and 649.5 nm. No structures were proposed for these components but a subsequent review by Brown (171) suggested that chlorophyll dimers and aggregates are the most likely forms of chlorophyll in vivo.

Lutz observed that the resonance Raman spectra of chlorophyll a and chlorophyll b in higher plant chloroplasts

and in solution were similar except for differences in the carbonyl stretching region from 1630 to 1710  $\text{cm}^{-1}$  and for magnesium-sensitive modes in the 200 to 350  $\text{cm}^{-1}$  region (68, 69, 73-76). At least five interaction states were distinguished for the chlorophyll a keto carbonyls and two for the chlorophyll b formyl carbonyls in vivo (73-76). Comparison with the resonance Raman spectra of oligomers and hydrated polymers of chlorophyll a and chlorophyll b showed that these types of chlorophyll species do not occur in the photosynthetic membrane. It was concluded that the chlorophylls are monomeric and bound to proteins by their conjugated carbonyls and magnesium atoms.

In this Chapter, LHC is used as a model system for the investigation of the resonance Raman spectroscopic properties of chlorophyll in vivo. Variation of the excitation wavelength reveals laser frequencies that may be employed to enhance selectively the resonance Raman spectra of the chlorophyll a and chlorophyll b molecules in LHC. The results obtained are supported by crude excitation profile calculations. The variety of interactions observed for the carbonyl groups may provide a mechanism to broaden and red-shift the electronic absorption bands of the chlorophylls in LHC. Results are also presented for a 28 kDa chlorophyll a-binding protein and a PS II reaction center complex from spinach.

## 2. Results

### i. Electronic Absorption Spectra

The electronic absorption spectrum of LHC isolated from pea leaves is shown in Figure 6.3. The bands at 436 and 677 nm correspond to chlorophyll a and those at 475 and 652 nm to chlorophyll b. The absorption bands of the chlorophylls in LHC are red-shifted compared to the absorption maxima of monomeric chlorophyll a (Soret:430 nm and  $Q_y$ :662 nm) and chlorophyll b (Soret:456 nm and  $Q_y$ :645 nm) in acetone solution (Table 6.1). LHC also contains carotenoid molecules that absorb in the 400 to 500 nm region although no specific carotenoid absorption bands are resolved in the spectrum.

Table 6.1 Electronic absorption maxima (nm) of chlorophyll a and chlorophyll b

	Chlorophyll a		Chlorophyll b	
	Soret	$Q_y$	Soret	$Q_y$
Acetone	430	662	456	645
LHC (pea)	436	677	475	652
LHC (spinach)	437	676	472	652
28 kDa protein	436	677	---	---
Reaction center	437	674	---	---

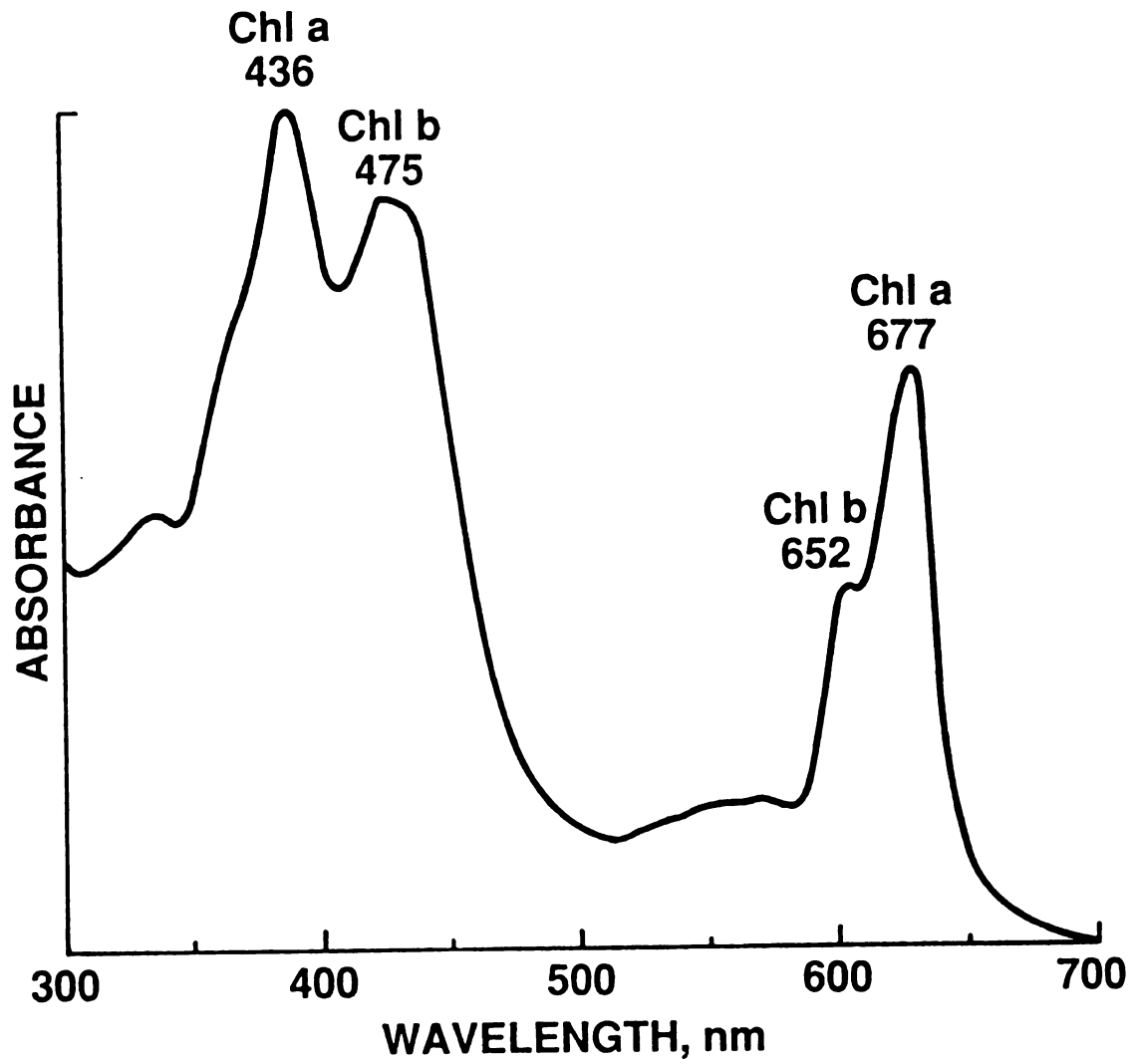


Figure 6.3 Electronic absorption spectrum of LHC isolated from pea leaves



Figure 6.4 shows the electronic absorption spectra of LHC, the 28 kDa chlorophyll a-binding protein and the LHC-depleted Photosystem II reaction center complex isolated from spinach (92). Table 6.1 lists the absorption maxima of the chlorophylls in these three protein complexes. The 28 kDa protein and the reaction center complex show absorption bands from chlorophyll a but not chlorophyll b. The 468 nm band in the 28 kDa protein results from absorption by carotenoids.

#### ii. Resonance Raman Spectra

Resonance Raman spectra of LHC at  $-125^{\circ}\text{C}$  were recorded with excitation wavelengths from 406.7 to 514.5 nm. Figures 6.5 and 6.6 show the resonance Raman spectra of LHC obtained with 413.1, 441.6, 472.7 and 514.5 nm excitation. Vibrational modes of chlorophyll a, chlorophyll b and carotenoids contribute to these spectra. By comparison with the resonance Raman spectra of chlorophyll a and chlorophyll b in solution, it is possible to determine which species contribute to the resonance Raman spectra of LHC at each excitation wavelength.

The resonance Raman spectra of chlorophyll a in acetone solution at  $-125^{\circ}\text{C}$  obtained with 413.1 and 441.6 nm excitation are shown in Figure 6.7. 413.1 nm excitation enhances the high frequency vibrational modes of chlorophyll a and with 441.6 nm excitation, both the high and low frequency modes are

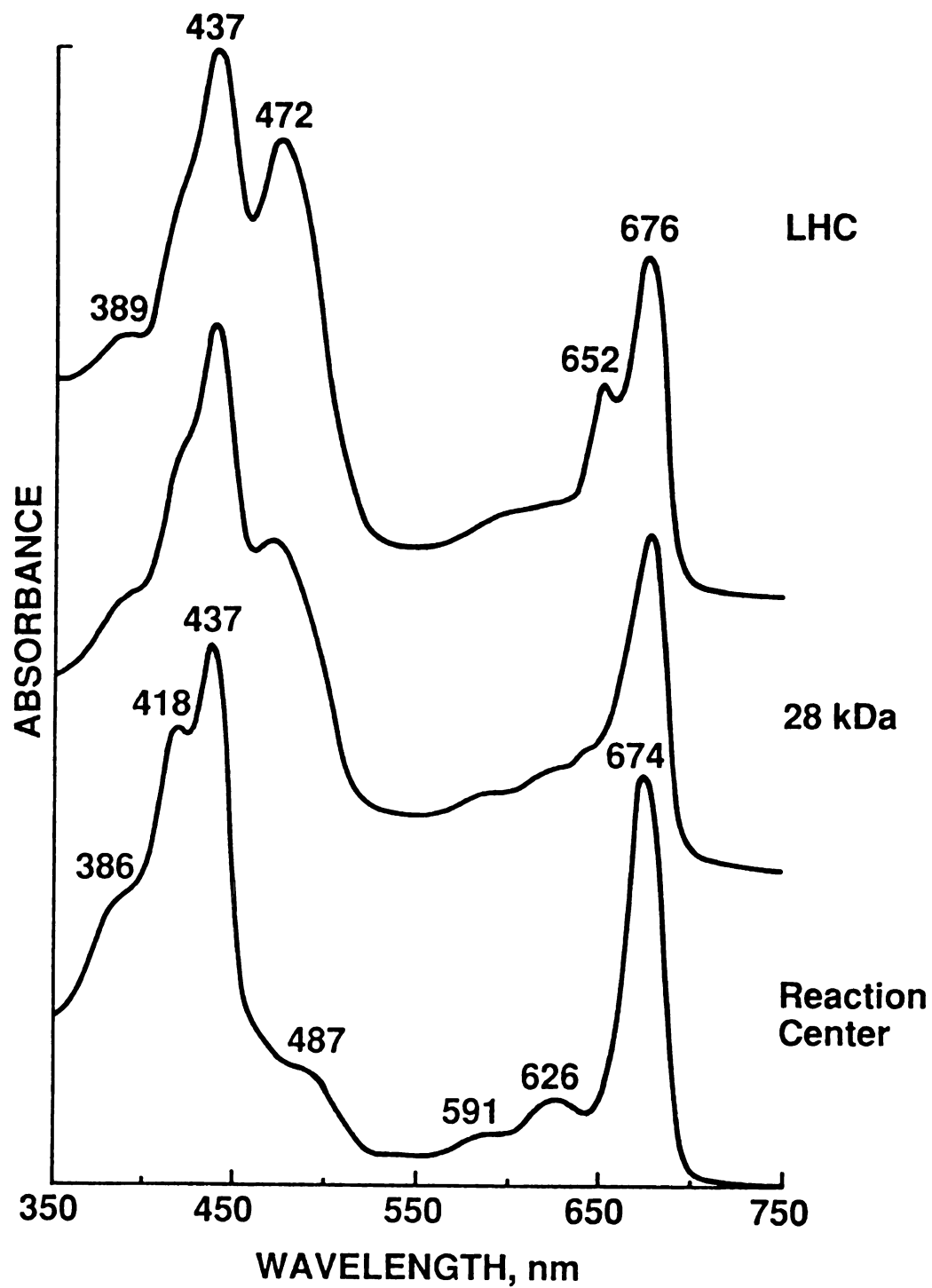


Figure 6.4 Electronic absorption spectra of LHC, the 28 kDa chlorophyll a-binding protein and the LHC-depleted Photosystem II reaction center complex isolated from spinach

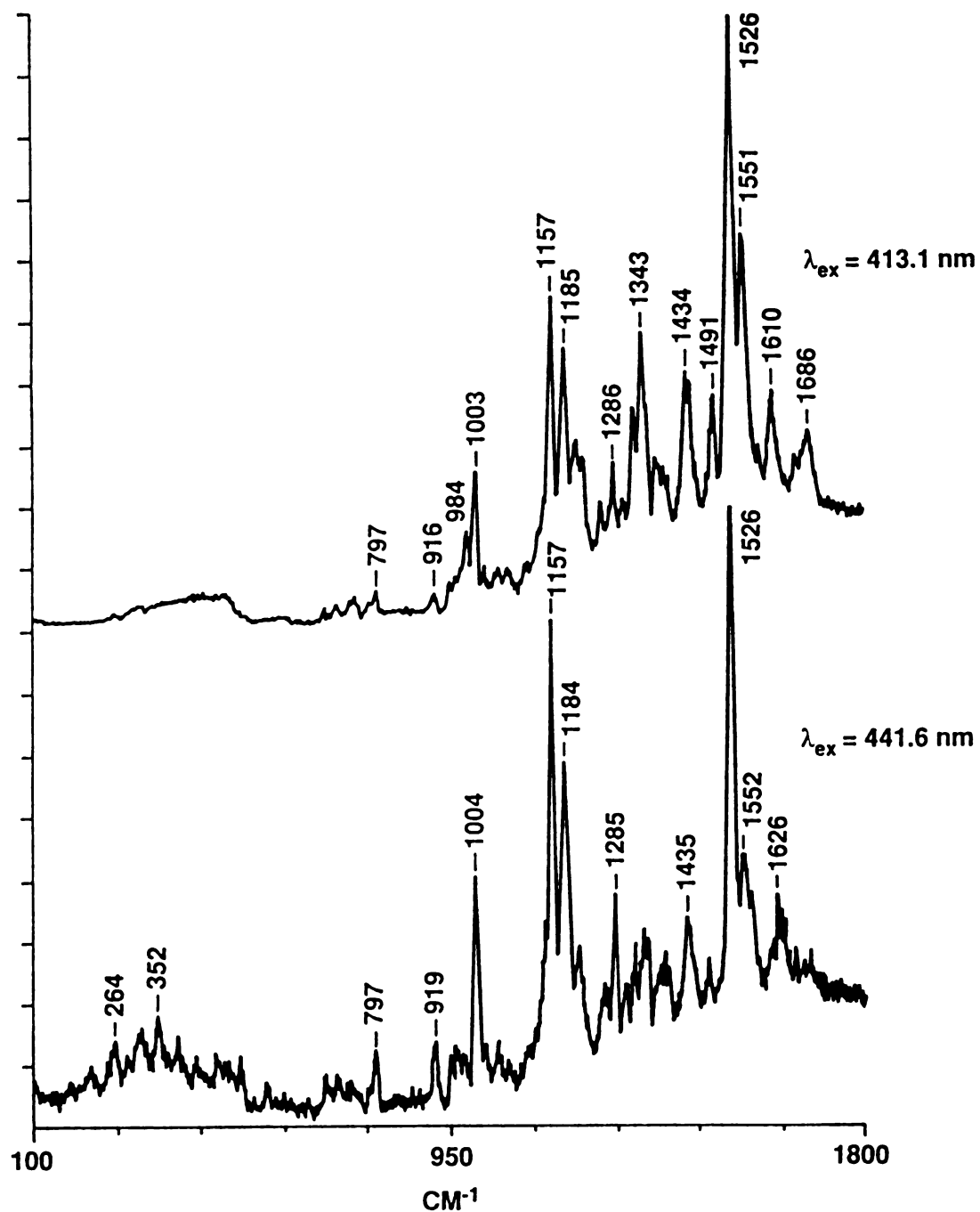


Figure 6.5 Resonance Raman spectra of LHC at  $-125^{\circ}\text{C}$  obtained with 413.1 and 441.6 nm excitation. Laser powers: 28 and 25 mW, respectively

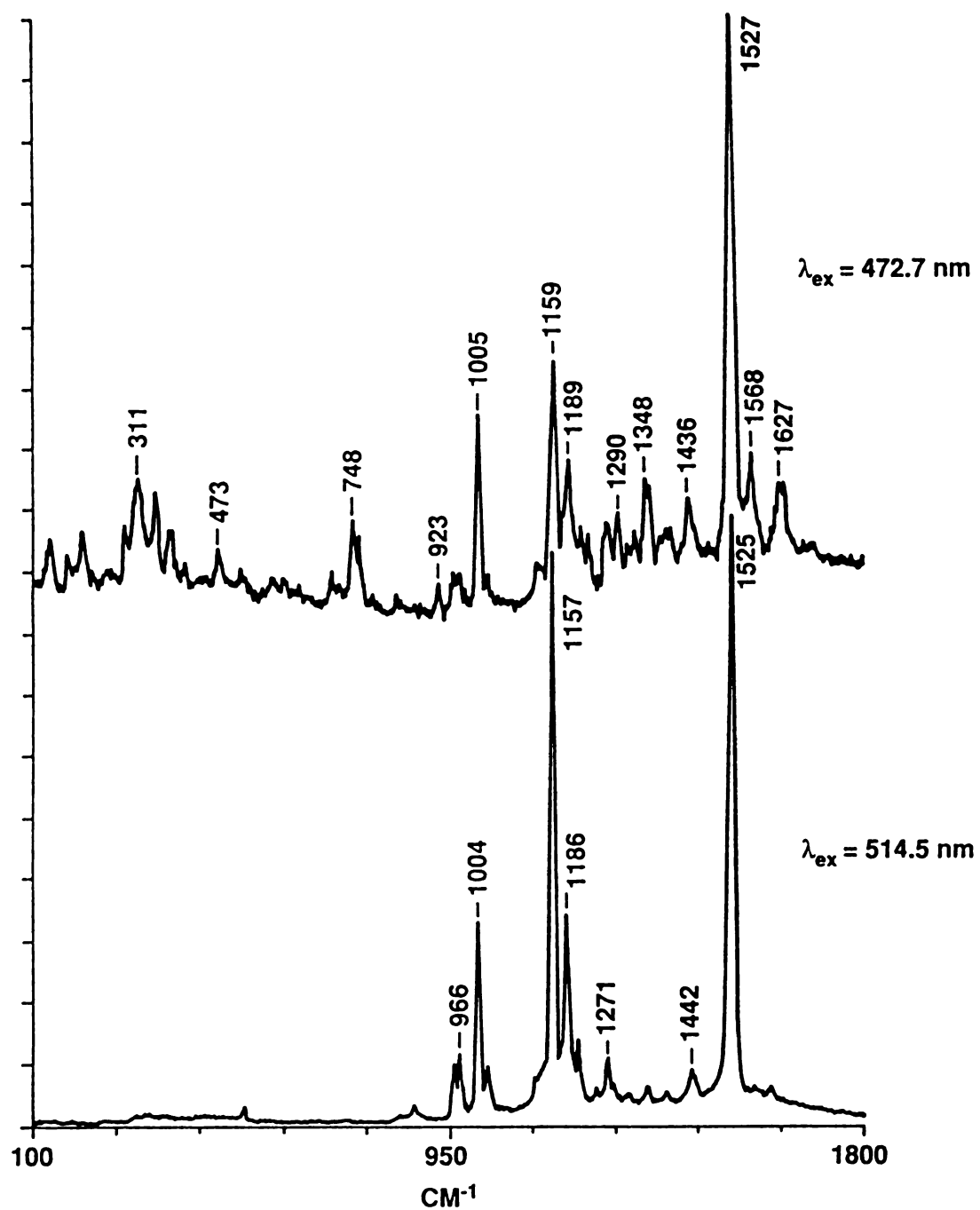


Figure 6.6 Resonance Raman spectra of LHC at  $-125^{\circ}\text{C}$  obtained with 472.7 and 514.5 nm excitation. Laser power: 45 mW

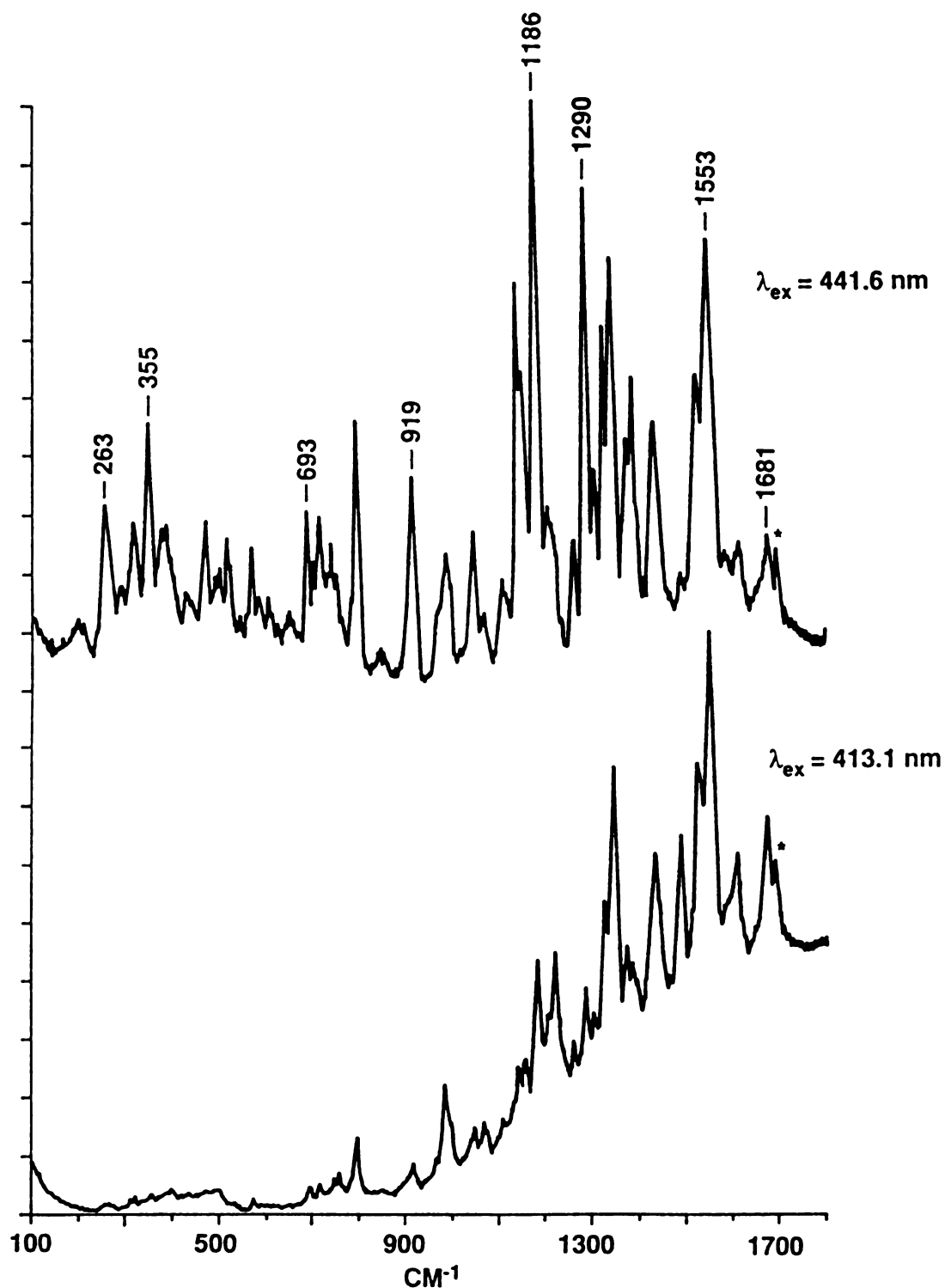


Figure 6.7 Resonance Raman spectra of chlorophyll a in acetone at  $-125^{\circ}\text{C}$  obtained with 413.1 and 441.6 nm excitation. Laser powers: 19 and 22 mW, respectively

enhanced. 472.7 nm excitation results in weak enhancement of the resonance Raman spectrum of chlorophyll a (spectrum not shown). The resonance Raman spectra of chlorophyll b in frozen acetone (Figure 6.8) show enhancement of high and low frequency modes with 472.7 nm excitation; enhancement of high frequency modes with 441.6 nm excitation; and, weak enhancement with 413.1 nm excitation (spectrum not shown).

Carotenoid vibrational modes are strongly enhanced with all of the excitation wavelengths used. The 514.5 nm excitation resonance Raman spectrum of LHC contains only carotenoid vibrational modes so that these bands are readily identified in the resonance Raman spectra of LHC recorded with other excitation wavelengths. Apart from the carotenoids, 413.1 nm excitation results in selective enhancement of the chlorophyll a vibrational modes in LHC. Chlorophyll b modes in LHC are selectively enhanced with 472.7 nm excitation. However, the resonance Raman spectrum of LHC recorded with 441.6 nm excitation contains bands from both chlorophyll a and chlorophyll b.

Resonance Raman spectra of LHC, the 28 kDa chlorophyll a-binding protein and the LHC-depleted Photosystem II reaction center complex from spinach were recorded with 406.7, 441.6 and 476.5 nm excitation for solution samples at 4°C. Figure 6.9 shows the resonance Raman spectra of the three protein complexes obtained with 406.7 nm excitation. At this

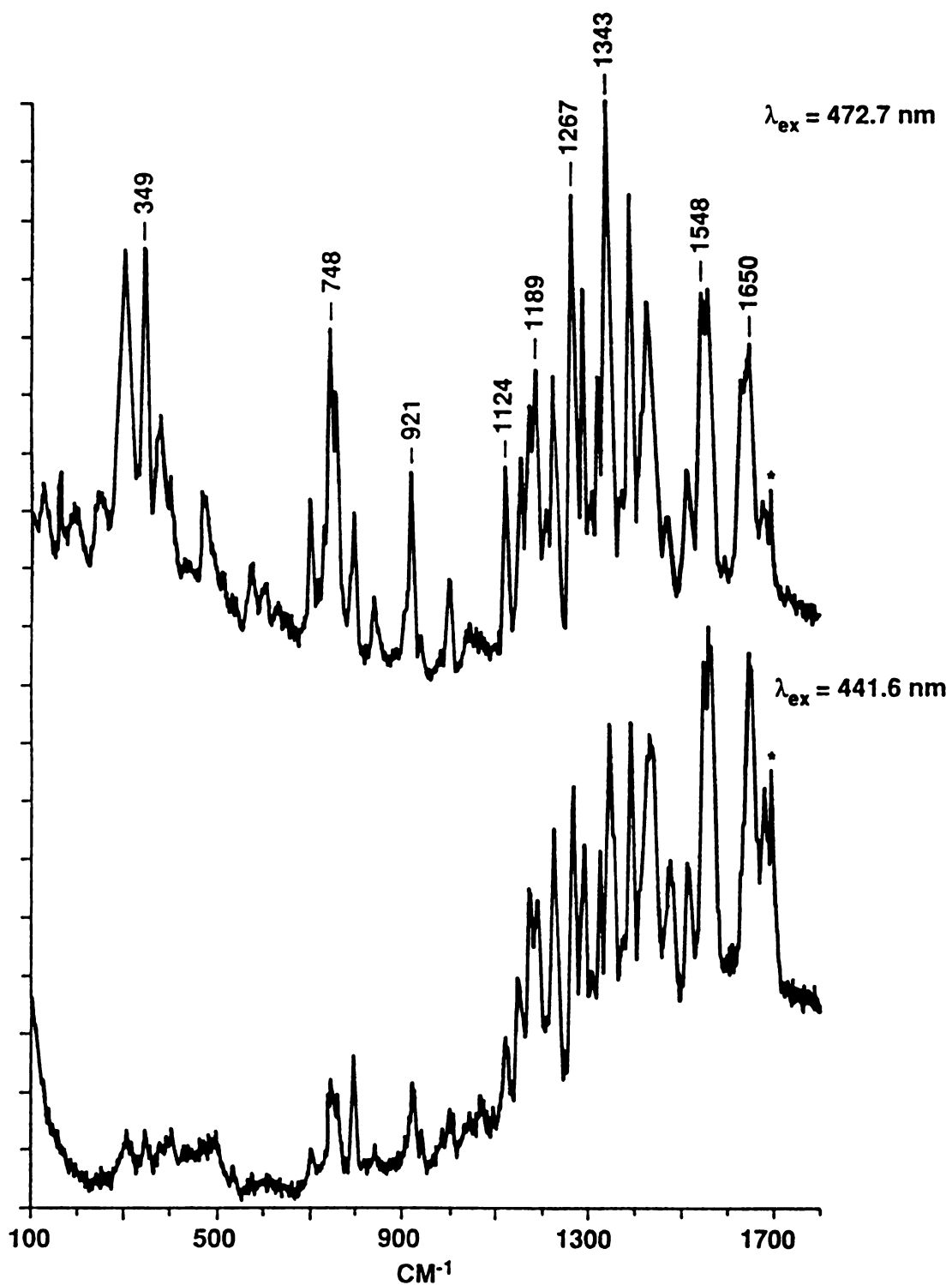


Figure 6.8 Resonance Raman spectra of chlorophyll b in acetone at  $-125^{\circ}\text{C}$  obtained with 441.6 and 472.7 nm excitation. Laser powers: 20 and 40 mW, respectively

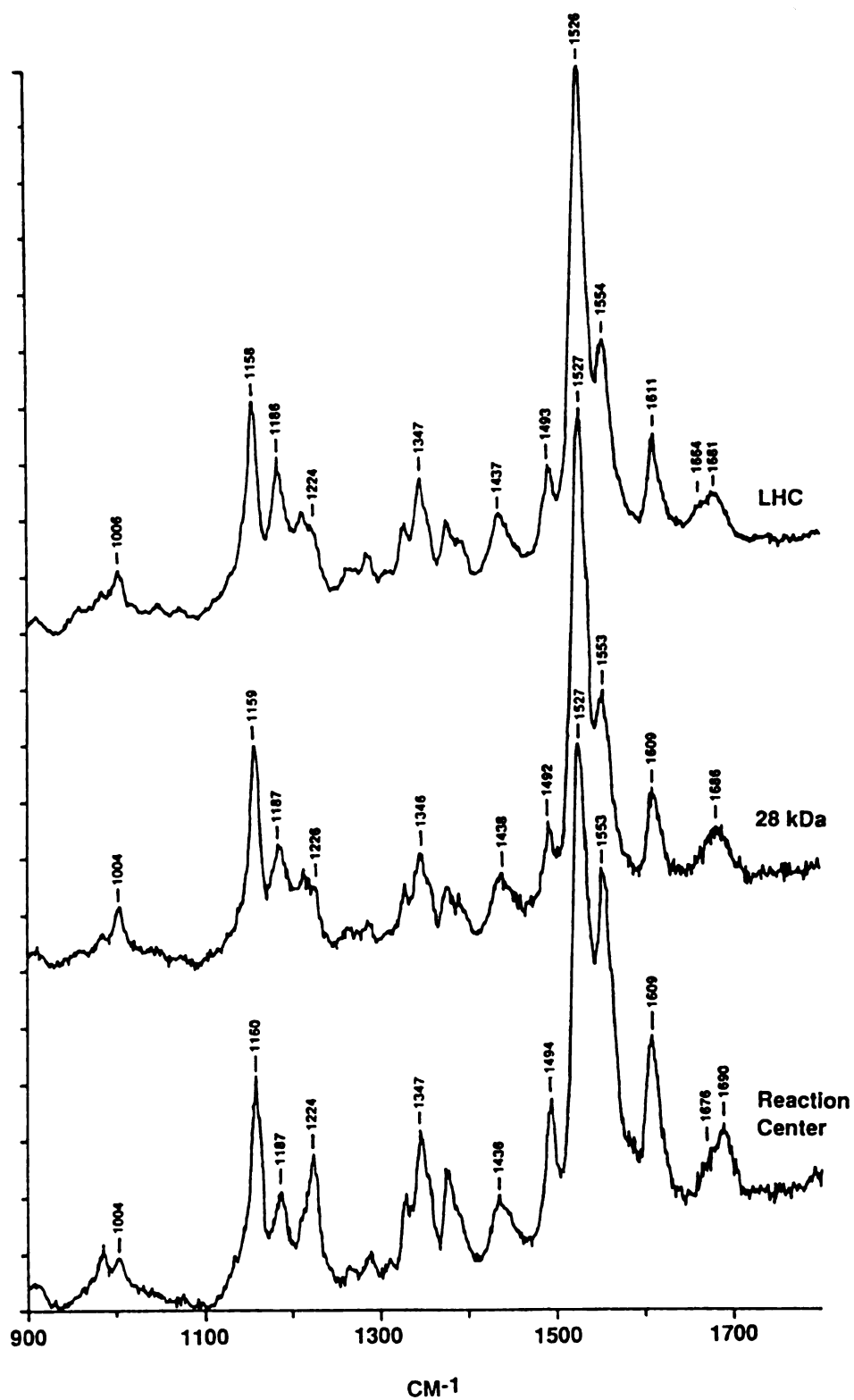


Figure 6.9 Resonance Raman spectra of LHC, the 28 kDa protein and the reaction center complex obtained with 406.7 nm excitation. Laser power: 20 mW



excitation wavelength, the high frequency vibrational modes of chlorophyll a are enhanced. The vibrational frequencies of chlorophyll a in the three complexes are nearly identical except in the carbonyl stretching region above  $1650\text{ cm}^{-1}$ . In this region, LHC shows a broad band with a maximum at  $1681\text{ cm}^{-1}$  and a second component at  $1664\text{ cm}^{-1}$ ; the 28 kDa protein shows a broad band with a maximum at  $1686\text{ cm}^{-1}$  and; the reaction center complex shows a sharper band at  $1690\text{ cm}^{-1}$  and a second component at  $1676\text{ cm}^{-1}$ .

The resonance Raman spectra of LHC, the 28 kDa protein and the reaction center complex obtained with  $441.6\text{ nm}$  excitation are shown in Figure 6.10. The high and low frequency modes of chlorophyll a are enhanced as well as several high frequency modes of chlorophyll b. In LHC, the modes at  $1564$ ,  $1631$  and  $1641\text{ cm}^{-1}$  correspond to chlorophyll b. Chlorophyll b vibrational modes are not observed in the spectra of the 28 kDa and reaction center complex proteins.

Figure 6.11 shows the resonance Raman spectra of LHC, the 28 kDa protein and the reaction center complex obtained with  $476.5\text{ nm}$  excitation. In LHC, chlorophyll b vibrational modes are observed. The 28 kDa protein and reaction center complex show only carotenoid bands.

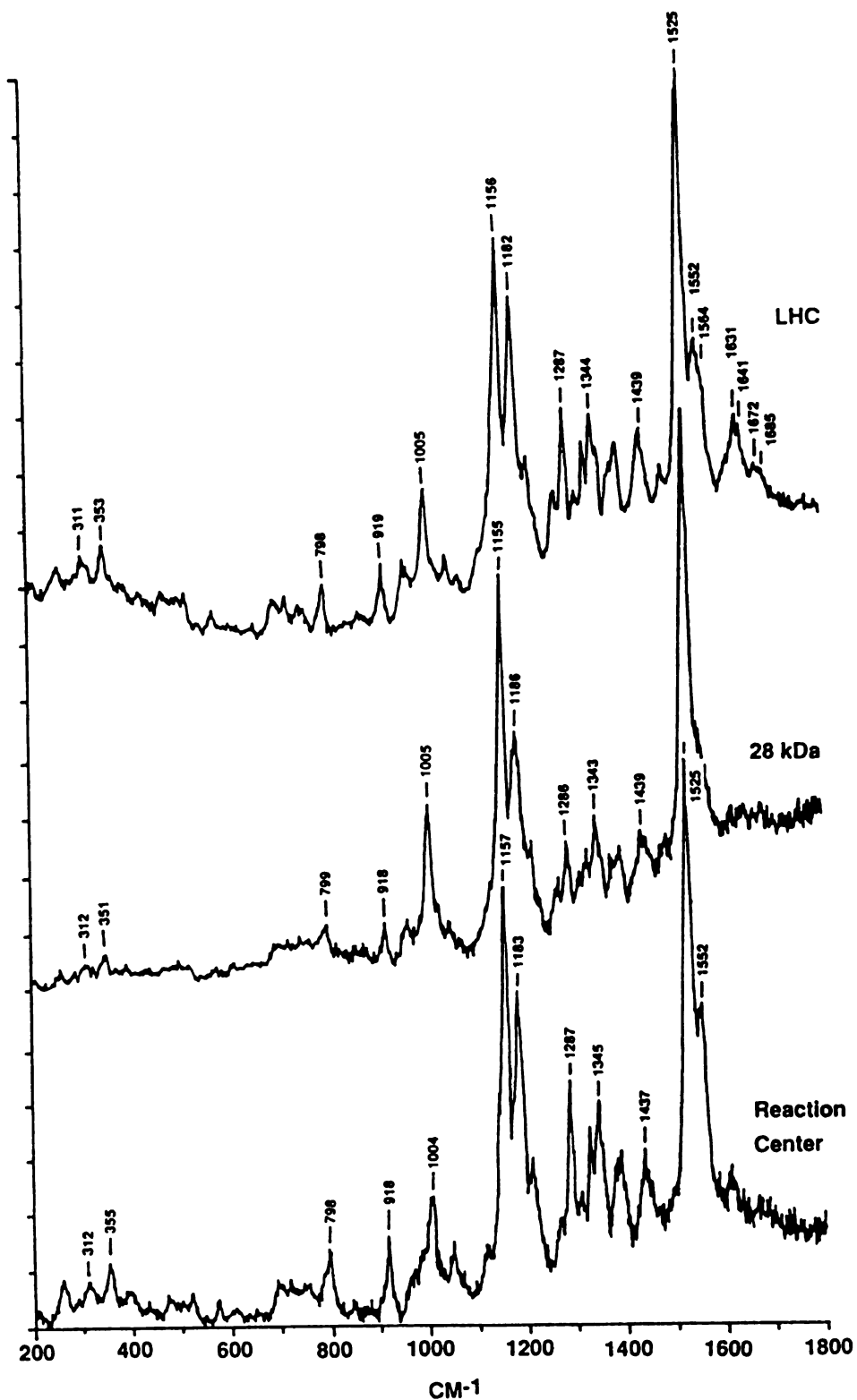


Figure 6.10 Resonance Raman spectra of LHC, the 28 kDa protein and the reaction center complex obtained with 441.6 nm excitation. Laser power: 22 mW

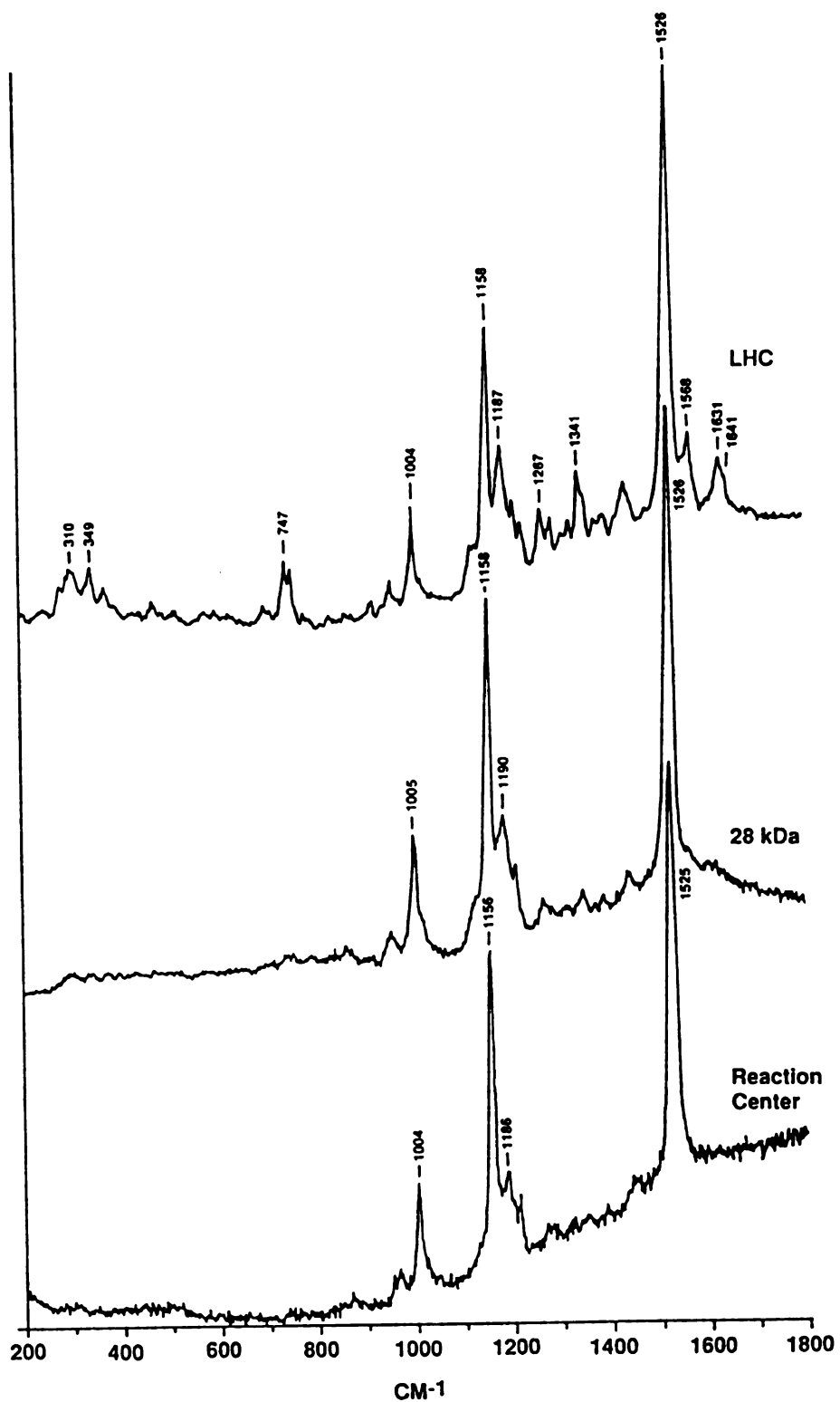


Figure 6.11 Resonance Raman spectra of LHC, the 28 kDa protein and the reaction center complex obtained with 476.5 nm excitation. Laser power: 25 mW

### 3. Discussion

#### i. Selective Enhancement of Chlorophyll a and Chlorophyll b

LHC contains chlorophyll a, chlorophyll b and carotenoid molecules, all of which have strong electronic transitions in the region from 400 to 500 nm. With Soret excitation, the resonance Raman spectrum of LHC is likely to contain contributions from all three chromophores. Unfortunately, it is not possible to record the resonance Raman spectrum of LHC without observing the carotenoid bands but by careful choice of the laser excitation wavelength, selective enhancement of the vibrational modes of chlorophyll a and chlorophyll b can be achieved. Comparison of the resonance Raman spectra of chlorophyll a and chlorophyll b in solution with those of LHC shows that with 413.1 nm excitation, the high frequency modes of chlorophyll a in LHC are enhanced; with 441.6 nm excitation, the high and low frequency modes of chlorophyll a and some of the high frequency modes of chlorophyll b are enhanced; with 472.7 nm excitation, the high and low frequency modes of chlorophyll b are enhanced; and with 514.5 nm excitation, only the carotenoid vibrational modes are enhanced. This pattern of mode enhancements can be explained by considering the excitation profiles of the chlorophyll a and chlorophyll b modes in LHC.

An excitation profile is a plot of the intensity of a Raman band as a function of excitation wavelength. Using the Born-Oppenheimer approximation to separate the electronic and vibrational wavefunctions allows the expression for the polarizability tensor,  $\alpha_{\rho\sigma}$  (Chapter 1, section 4) to be expanded and represented as the sum of two terms:

$$\alpha_{\rho\sigma} = A_{\rho\sigma} + B_{\rho\sigma}$$

The A and B terms correspond to Franck-Condon and Herzberg-Teller scattering mechanisms, respectively (45-48). For Soret excitation, the intensity of a Raman band is proportional to the square of the A term (172):

$$I = |A|^2 = \left| \frac{\langle g0|i0\rangle}{E_{00} - h\nu - i\Gamma} - \frac{\langle g0|i1\rangle}{E_{01} - h\nu - i\Gamma} \right|^2$$

where  $\langle g0|$  is the lowest vibrational level of the ground electronic state,  $E_{00}$  is the energy of the Soret transition and  $E_{01} = E_{00} + \nu$ , where  $\nu$  is the vibrational frequency for a particular mode. The incident laser frequency is  $\nu_L$  and  $\Gamma$  is the damping term or homogeneous linewidth of the Soret excited state. The first term corresponds to resonance with the lowest vibrational level of the Soret excited state,  $|i0\rangle$ , and the second term to resonance with the first vibrational level of the Soret excited state,  $|i1\rangle$ .

In the calculation of the excitation profile, the Franck-Condon factors  $\langle g_0 | i_0 \rangle$  and  $\langle g_0 | i_1 \rangle$  are approximated by the extinction coefficient,  $\epsilon$ , for the Soret band maximum. This simplified expression predicts an excitation profile for a vibrational mode to have two peaks, one at the 0-0 transition and one at the 0-1 transition. As the vibrational frequency approaches the magnitude of the damping term the two peaks in the excitation profile coalesce.

Calculated excitation profiles for a high frequency  $1600 \text{ cm}^{-1}$  mode and a low frequency  $300 \text{ cm}^{-1}$  mode of chlorophyll a and chlorophyll b are shown in Figure 6.12. The extinction coefficient and linewidth are obtained from the electronic absorption spectrum of the chlorophylls in acetone solution. The positions of the Soret maxima are for the chlorophylls in LHC. The parameters used for chlorophyll a are:  $\epsilon = 101.5 \text{ mM}^{-1}\text{cm}^{-1}$ ,  $\Gamma = 440 \text{ cm}^{-1}$  and  $E_{00} = 22936 \text{ cm}^{-1}$  ( $= 436 \text{ nm}$ ); and for chlorophyll b:  $\epsilon = 148.0 \text{ mM}^{-1}\text{cm}^{-1}$ ,  $\Gamma = 640 \text{ cm}^{-1}$  and  $E_{00} = 21053 \text{ cm}^{-1}$  ( $= 475 \text{ nm}$ ). Figure 6.12 shows two peaks in the excitation profiles for the  $1600 \text{ cm}^{-1}$  mode but only one for the  $300 \text{ cm}^{-1}$  mode. The  $1600 \text{ cm}^{-1}$  mode of chlorophyll a is enhanced with  $413.1 \text{ nm}$  or  $441.6 \text{ nm}$  excitation but not with  $472.7 \text{ nm}$  or  $514.5 \text{ nm}$  excitation. The  $1600 \text{ cm}^{-1}$  mode of chlorophyll b is enhanced with  $441.6$  or  $472.7 \text{ nm}$  excitation but not with  $413.1 \text{ nm}$  or  $514.5 \text{ nm}$  excitation. The low frequency  $300 \text{ cm}^{-1}$  mode of chlorophyll a is enhanced with  $441.6 \text{ nm}$  excitation. For chlorophyll b, the low frequency  $300 \text{ cm}^{-1}$  mode is enhanced with  $472.7 \text{ nm}$

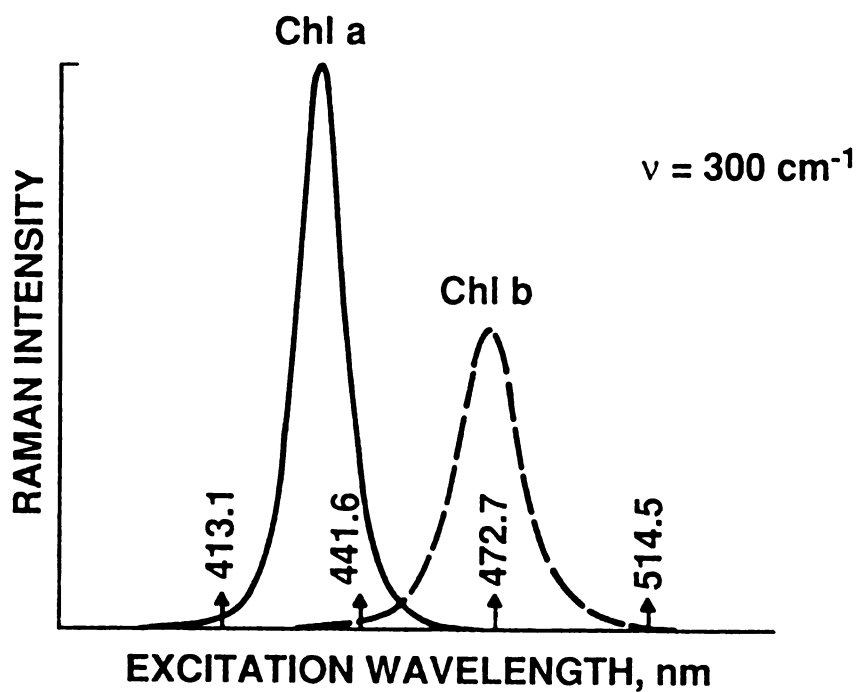
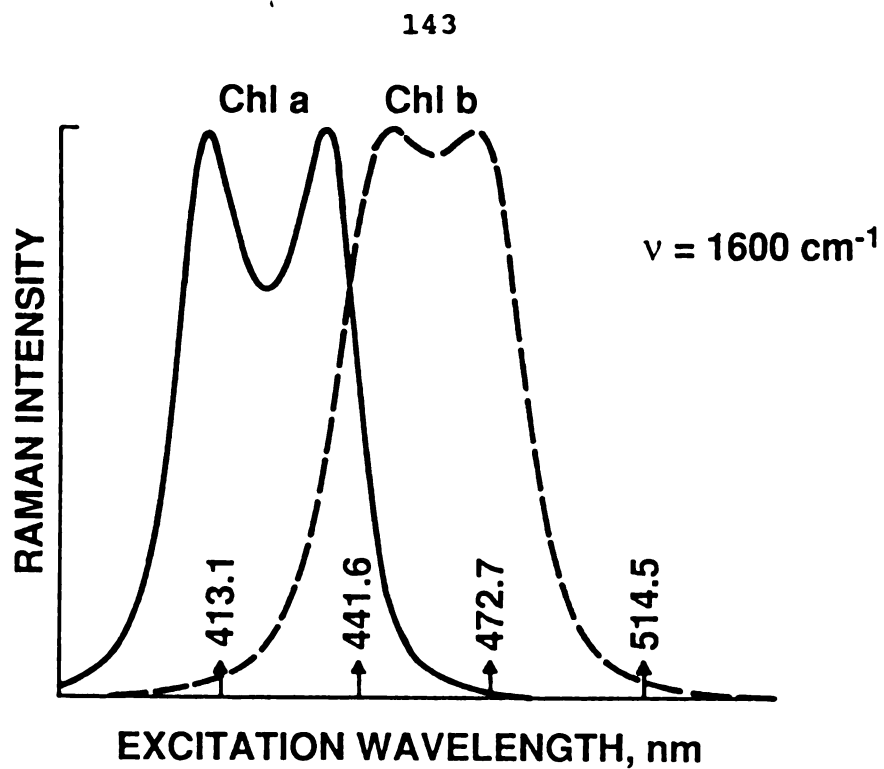


Figure 6.12 Calculated excitation profiles for a  $1600 \text{ cm}^{-1}$  mode and a  $300 \text{ cm}^{-1}$  mode of chlorophyll a (—) and chlorophyll b (— —) in LHC

excitation. These calculated excitation profiles provide a useful means of interpreting the pattern of chlorophyll a and chlorophyll b vibrational modes observed in LHC with changing excitation wavelength.

In previous studies by Lutz on the resonance Raman spectra of chlorophylls in vivo it was assumed that the 441.6 nm line provided selective enhancement of chlorophyll a modes and lines from 457.9 nm to 472.7 nm could be used for selective enhancement of chlorophyll b modes. The results obtained here clearly show that care must be taken in asserting that a resonance Raman spectrum corresponds to only chlorophyll a or chlorophyll b. Selective enhancement for the high and low frequency modes of chlorophyll b is indeed possible at 472.7 nm. For chlorophyll a however, the low frequency modes may be selectively enhanced at 441.6 nm and the high frequency modes at 413.1 nm.

## ii. Mg Coordination State

The electronic absorption spectra of chlorophyll a in solution are characteristic of the coordination state of the Mg atom. The most pronounced effect is the large red-shift of the  $Q_{x00}$  band of 6-coordinate chlorophyll a in pyridine solution compared to 5-coordinate chlorophyll a in acetone solution (Figure 5.2). One possible mechanism to broaden the



absorption bands of the chlorophylls in LHC would be to create a mixture of 5 and 6-coordinate chlorophyll species in the protein.

In Chapter 5, the core-size sensitive resonance Raman modes of chlorophyll a were identified by metal substitution and it was demonstrated that the frequencies of these modes could be used to diagnose the coordination state of the Mg atom in chlorophyll a. From these results and those of Fujiwara and Tasumi (142), the resonance Raman bands of chlorophyll a at 1527-1529, 1551-1554 and 1606-1612  $\text{cm}^{-1}$  indicate 5-coordination while a set of lower frequency bands at 1518-1521, 1545-1548 and 1596-1599  $\text{cm}^{-1}$  indicate 6-coordination. The two resonance Raman bands of chlorophyll a at 1551 and 1610  $\text{cm}^{-1}$  in the 413.1 nm excitation spectrum of LHC are characteristic of 5-coordinate Mg. The strong 1526  $\text{cm}^{-1}$  carotenoid band obscures the third core-size sensitive chlorophyll a mode. There is no evidence for any 6-coordinate chlorophyll a.

For chlorophyll b, core-size sensitive resonance Raman modes at 1520-1523, 1564-1566 and 1607  $\text{cm}^{-1}$  were determined by Fujiwara and Tasumi (142) to be characteristic of 5-coordination. Upon 6-coordination, the 1564-1566  $\text{cm}^{-1}$  mode splits into two components at 1549-1551 and 1559  $\text{cm}^{-1}$  and the two other core-size sensitive modes shift to lower frequencies at 1516-1519 and 1594-1596  $\text{cm}^{-1}$ . The 441.6 nm excitation

resonance Raman spectrum of LHC shows two chlorophyll b bands at 1568 and 1607  $\text{cm}^{-1}$  indicating 5-coordination. Again, the third core-size sensitive mode is obscured by the 1526  $\text{cm}^{-1}$  carotenoid band. The 1552  $\text{cm}^{-1}$  band in the 441.6 nm excitation spectrum is a chlorophyll a vibrational mode and not an indicator of 6-coordinate chlorophyll b. 472.7 nm excitation clearly shows the 1568  $\text{cm}^{-1}$  5-coordinate chlorophyll b mode with no contributions from 6-coordinate chlorophyll b (173).

The observation of 5-coordination only for the chlorophyll a and chlorophyll b molecules in LHC rules out mixtures of 5 and 6-coordinate chlorophyll species as a mechanism to broaden the absorption bands. X-ray crystal structures of the reaction center from *R. viridis* (157,158) and a light-harvesting bacteriochlorophyll a-protein from the green photosynthetic bacterium *Prosthecochloris aestuarii* (174) show that all of the bacteriochlorophylls are 5-coordinate. The four bacteriochlorophyll b molecules in the reaction center complex and five of the seven bacteriochlorophyll a molecules in the *P. aestuarii* complex are ligated by histidine residues from the protein. Resonance Raman spectroscopy can distinguish between 5 and 6-coordination for chlorophyll but cannot identify the ligands.

## iii. Carbonyl Stretching Region

In agreement with the findings of Lutz, the resonance Raman spectra of chlorophyll a and chlorophyll b in LHC and as monomers in acetone solution differ mainly in the carbonyl stretching region. Chlorophyll a has a conjugated keto carbonyl at the 9-position (Figure 1.1). In chlorophyll b there are two conjugated carbonyl groups: a keto carbonyl at the 9-position and a formyl carbonyl at the 3-position. Table 6.2 lists the bands observed for LHC in the carbonyl stretching region and their assignments.

Table 6.2 Chlorophyll a and chlorophyll b carbonyl stretching frequencies ( $\text{cm}^{-1}$ ) in LHC

413.1	441.6	472.7	Assignment
1697			unbound keto chl a
		1693	unbound keto chl b
1686	1688		unbound keto chl a
1675	1674		H-bonded keto chl a
1659	1656		H-bonded keto chl a
	1635	1636	H-bonded formyl chl b
	1626	1627	H-bonded formyl chl b

Resonance Raman spectra of LHC obtained with 413.1 nm excitation show four chlorophyll a keto carbonyl stretching modes at 1697, 1686, 1675 and 1659  $\text{cm}^{-1}$ . 441.6 nm excitation is expected to enhance both chlorophyll a and chlorophyll b carbonyl stretching modes. The frequencies of the chlorophyll a keto carbonyl stretching modes at 1688, 1674 and 1656  $\text{cm}^{-1}$  are close to those observed with 413.1 nm excitation. The two modes at 1635 and 1626  $\text{cm}^{-1}$  are assigned to chlorophyll b formyl carbonyl stretching modes. The Soret band maximum of chlorophyll b in LHC occurs at 475 nm ( $= 21053 \text{ cm}^{-1}$ ) so that the  $E_{01}$  transition for a 1630  $\text{cm}^{-1}$  mode of chlorophyll b is expected at 22683  $\text{cm}^{-1}$  or 440.9 nm. Strong enhancement of the chlorophyll b formyl carbonyl stretching modes is therefore expected with 441.6 nm excitation. Only chlorophyll b modes are enhanced in the 472.7 nm excitation spectrum. Using this excitation wavelength, the two formyl stretching modes at 1636 and 1627  $\text{cm}^{-1}$  are seen as well as the chlorophyll b keto carbonyl stretching mode at 1693  $\text{cm}^{-1}$ .

The variety of chlorophyll a and chlorophyll b carbonyl stretching frequencies in LHC indicates different populations of chlorophyll molecules in the protein. Four populations of chlorophyll a and two of chlorophyll b can be distinguished from the resonance Raman spectra of LHC. The interactions with the chlorophyll carbonyl groups may account for the broadened and red-shifted absorption bands in LHC.

The two modes at 1697 and 1686  $\text{cm}^{-1}$  in LHC most likely correspond to stretching vibrations of the unbound keto carbonyls of chlorophyll a molecules within two different environments in the protein. The frequency of the keto carbonyl stretching mode of chlorophyll a is highly dependent on the solvent. The resonance Raman spectra of chlorophyll a in acetone, diethyl ether and pyridine solution at  $-125^{\circ}\text{C}$  show the keto carbonyl stretching frequency at 1681, 1686 and 1681  $\text{cm}^{-1}$ , respectively (Figure 5.4). Fujiwara and Tasumi (142) and Koyama *et al.* (175) have reported resonance Raman spectra of monomeric chlorophyll a in polar solvents at room temperature. The keto carbonyl stretching frequency ranged from 1680 to 1702  $\text{cm}^{-1}$  with the frequency increasing as the dielectric constant of the solvent decreased. The two carbonyl stretching modes at 1697 and 1686  $\text{cm}^{-1}$  are in the frequency range expected for an unbound keto carbonyl of monomeric chlorophyll a.

The 413.1 nm excitation spectrum of LHC shows two additional chlorophyll a keto carbonyl stretching modes at 1675 and 1659  $\text{cm}^{-1}$ . Lutz has proposed that the chlorophyll carbonyls that are not free are H-bonded to amino acid residues in the protein (76). The resonance Raman spectrum of chlorophyll a in methanol solution (Figure 5.4) shows the H-bonded keto carbonyl stretching frequency at 1661  $\text{cm}^{-1}$ . The frequency of this mode increases to 1668  $\text{cm}^{-1}$  in methanol solution at room temperature (142,175). Koyama *et al.* observed that the H-bonded keto carbonyl stretching frequency for

chlorophyll a in other alcohol solutions ranged from 1670 to 1675  $\text{cm}^{-1}$  and appeared to be independent of the dielectric constant of the solvent. The 1675 and 1659  $\text{cm}^{-1}$  bands may therefore be attributed to chlorophyll a H-bonded keto carbonyl stretching modes with differing H-bond strengths.

H-bonding to the conjugated keto carbonyl of chlorophyll a can produce a red-shift of the electronic absorption spectrum. Babcock and Callahan (1976) determined that H-bonding to the conjugated formyl group of heme a model compounds lowered the carbonyl stretching frequency and resulted in a red-shift of the  $\alpha$  ( $Q_{00}$ ) absorption band. The magnitude of the carbonyl stretching frequency decrease and red-shift both increase as the strength of the H-bond increases. The low frequencies of the 1675 and 1659  $\text{cm}^{-1}$  chlorophyll a keto carbonyl stretching modes and the red-shifted absorption bands in LHC can be explained by H-bonding. A larger red-shift is expected for the chlorophyll a population in LHC that has the 1659  $\text{cm}^{-1}$  keto carbonyl stretching frequency.

The same type of analysis can be applied to the chlorophyll b carbonyl stretching frequencies in LHC. The 1693  $\text{cm}^{-1}$  mode in the 472.7 nm excitation is attributed to the unbound keto carbonyl of chlorophyll b. H-bonded formyl carbonyls are observed at 1636 and 1627  $\text{cm}^{-1}$ . Thus there are two populations of chlorophyll b molecules in LHC with H-bonded formyls of differing strength but with their keto carbonyls free.

## iv. 28 kDa and Reaction Center Complex Proteins

Ghanotakis et al. have isolated an oxygen-evolving PS II reaction center core complex from spinach that contains approximately 60 chlorophylls per PS II (92). Treatment of PS II membranes with octyl glucopyranoside separates LHC from the reaction center complex of 9 polypeptides with molecular weights of 47, 43, 33, 32, 30, 28, 20, 10 and 9 kDa. Solubilization of the reaction center complex with dodecyl  $\beta$ -D-maltoside followed by gel-filtration chromatography leaves a PS II reaction center core complex containing the 47, 43, 33, 32, 30 and 9 kDa polypeptides. The 28 kDa chlorophyll-binding protein is also isolated in this procedure.

The LHC, 28 kDa protein and LHC-depleted PS II reaction center complexes isolated by Ghanotakis et al. were studied by resonance Raman spectroscopy. The resonance Raman spectra of LHC from spinach (Figures 6.9-6.11) are similar to those of LHC from pea (Figures 6.5 and 6.6). These spectra show the presence of both chlorophyll a and chlorophyll b in spinach LHC with 5-coordination of the Mg atoms. Two populations of chlorophyll b molecules can be distinguished by the stretching frequencies of their formyl carbonyls at 1631 and 1641  $\text{cm}^{-1}$  in the 441.6 and 476.5 nm excitation spectra. The chlorophyll a carbonyl stretching region is not resolved since spectra were recorded at 4°C as compared to -125°C for LHC from pea.

Resonance Raman spectra of the 28 kDa and reaction center complex proteins recorded with 406.7 and 441.6 nm excitation show only chlorophyll a and carotenoid vibrational modes. The reaction center complex preparation still contains 60 chlorophylls per PS II. The resonance Raman spectra are dominated by the antenna chlorophylls so that it is not possible to observe vibrational modes of the reaction center chlorophylls or the two pheophytin a molecules in each reaction center. More importantly, the lack of any chlorophyll b vibrational modes in the 476.5 nm excitation spectra of the 28 kDa protein and reaction center complex confirms the absence of chlorophyll b in these two complexes. Ghanotakis et al. suggested that the 28 kDa protein is either a separate protein intermediate between LHC and the PS II reaction center complex or a component of LHC. The 28 kDa protein has a molecular weight that is typical of LHC polypeptides but these authors were unable to isolate the 28 kDa protein from LHC. The absence of chlorophyll b indicates that the 28 kDa protein is not part of LHC.



#### 4. Conclusions

LHC contains three types of chromophore: chlorophyll a, chlorophyll b and carotenoids. The primary function of this protein is to absorb light. Comparison with the spectra of the chlorophylls in solution shows that the electronic absorption bands of LHC are broadened and red-shifted. Broadening of the absorption bands allows light to be absorbed over a greater wavelength range thereby increasing the efficiency of light energy utilization. This is accomplished by the creation of four separate populations of chlorophyll a and two of chlorophyll b in LHC. Different coordination states of the Mg atoms are not a factor since all of the chlorophylls are 5-coordinate. H-bonds to the conjugated keto carbonyls are responsible for creating two of the chlorophyll a populations. The local protein environments may account for the two other chlorophyll a populations. The chlorophyll b molecules are distinguished by the strength of the H-bond to their conjugated formyl carbonyls. Each of these species has its own distinct absorption spectrum that contributes to the overall absorption spectrum of LHC. H-bonding to the unconjugated ester carbonyls may also occur and help to orient the chlorophyll molecules in the protein but will not influence the absorption spectrum.

Determination of the structures of the chlorophylls in LHC is essential to understanding their function. Once a photon has been absorbed by LHC, the excitation energy needs to be transferred to the reaction center. Elucidation of the mechanism of exciton migration from the antenna chlorophylls to the reaction center requires knowledge of the arrangements of the chlorophylls in the protein and the relation of LHC to the reaction center polypeptides. Help in this area is likely to come from biochemical procedures for isolating the individual chlorophyll-binding proteins and determining their amino acid sequences.

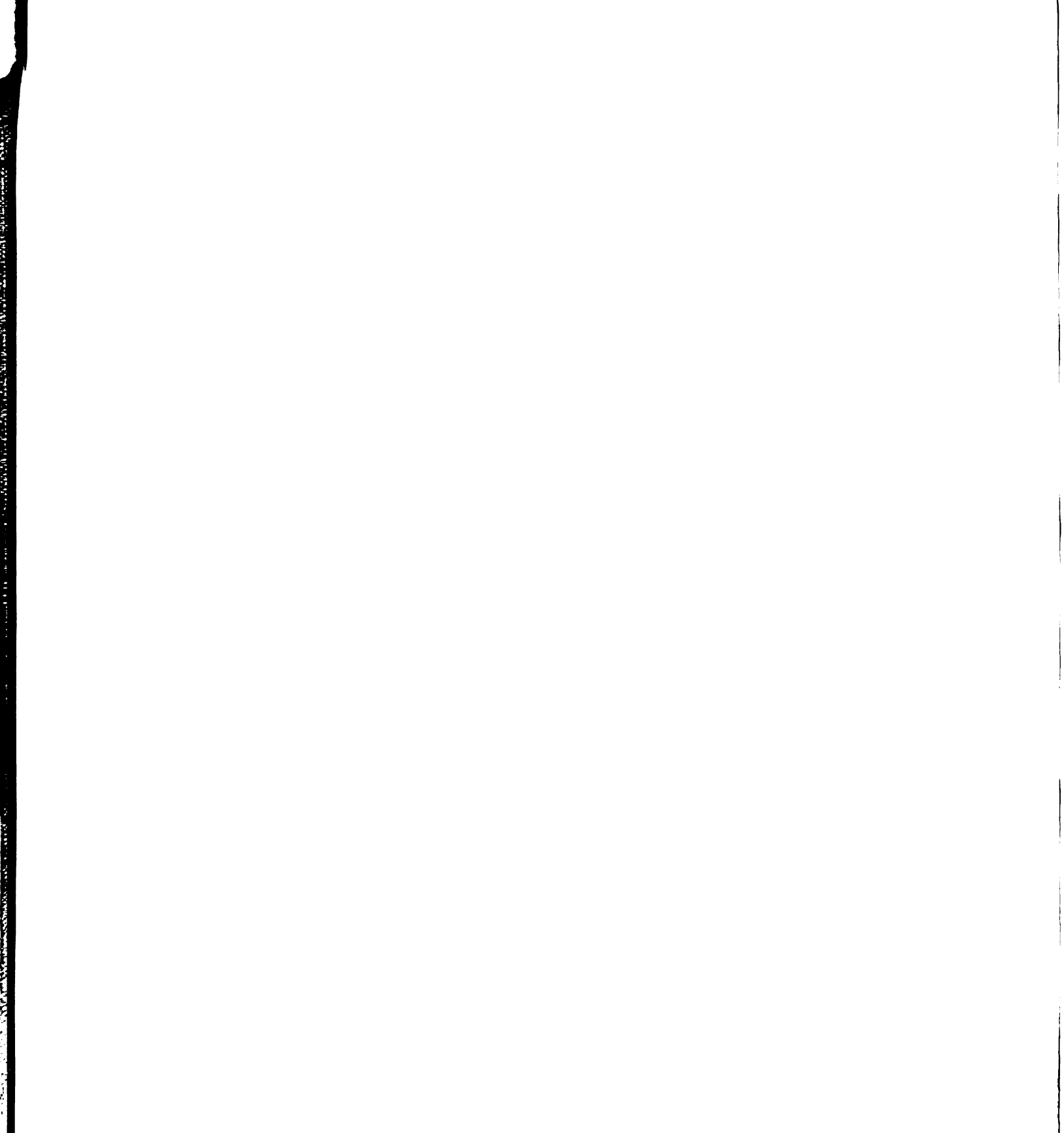
## CHAPTER 7

### SUGGESTIONS FOR FURTHER WORK

The original goal of this research project was to explore the vibrational properties of chlorophyll and chlorophyll-binding proteins using resonance Raman spectroscopy. Resonance Raman spectra of chlorophyll a and chlorophyll b were recorded in solution and in the light-harvesting chlorophyll a/b protein complex. However, a major obstacle in the interpretation of these spectra was the lack of a set of vibrational mode assignments for chlorophyll. Attention was therefore focused on determining the vibrational characteristics of metallochlorins as models for the more complex chlorophyll. In contrast to the approach taken by other groups (45,66,95-98), the vibrational modes of metallochlorins could not be assigned by a direct comparison with the normal modes of metalloporphyrins.

The starting point for the interpretation of the resonance Raman and IR spectra of metalloporphyrins is the normal coordinate analysis of NiOEP performed by Abe et al. (55,56). The set of mode assignments for NiOEP are widely accepted in resonance Raman studies of metalloporphyrins

although there is still disagreement over the form of the IR active  $E_u$  modes. The NiOEP normal coordinate analysis attributes modes  $\nu_{37}$  and  $\nu_{38}$  to  $C_aC_m$  and  $C_bC_b$  stretching, respectively. These assignments are supported by the work of Willems and Bocian on acetyl and formyl-substituted deuterioporphyrins (177,178). Other groups have argued that the assignments for  $\nu_{37}$  and  $\nu_{38}$  should be reversed (65,100,179) since it is  $\nu_{38}$  that exhibits the larger core-size dependency and deuteration shift characteristic of  $C_aC_m$  stretching. Oertling et al. have shown that changing the peripheral substituents from OEP to EPI can identify those resonance Raman modes with a contribution from  $C_bC_b$  and  $C_bC_a$  stretching and  $C_bC_a$  bending coordinates (99). Comparison of the IR spectra of MOEP and MEPI would be useful for clarifying the  $E_u$  mode characters. The  $E_u$  modes for NiOEP have been recalculated by Abe (compare ref. 56 with 55) but the mode characters for  $\nu_{37}$  and  $\nu_{38}$  were unchanged. A possible source of error in the determination of the  $E_u$  modes is the use of resonance Raman frequencies from NiOEP in  $CH_2Cl_2$  solution but IR frequencies from NiOEP in a CsI disk. NiOEP has two crystal structures: a planar triclinic form (60) and a buckled tetragonal form (180). We have observed resonance Raman spectra of both forms of NiOEP in KBr disc samples depending on the ratio of porphyrin to KBr in the sample. Ideally, resonance Raman and IR spectra of metalloporphyrins should be measured in the same medium.



Numerous factors such as the central metal, axial ligation, peripheral substitution, macrocycle distortions, ring oxidation and reduction influence the vibrational properties of metalloporphyrins in biological systems. Many of these effects are well understood but one area that requires further investigation is to determine the consequences of symmetry-lowering. The mode assignments for metalloporphyrins are based on the normal coordinate analysis of the highly symmetric NiOEP molecule. Protoheme and heme a are two examples of naturally-occurring porphyrins that have conjugated peripheral substituents. The presence of conjugated substituents eg. vinyl and carbonyl groups, lowers the molecular symmetry thereby allowing the  $E_u$  modes to become resonance Raman active. Analyses have been reported for protoporphyrin IX (65,116,179) as well as formyl and acetyl-substituted deuteroporphyrins (177,178). Further studies of model compounds are needed to establish precisely how far the symmetry must be lowered to induce Raman activity of the  $E_u$  modes (and IR activity of the resonance Raman modes). Determination of excitation profiles would be useful since Shelnutt has developed expressions for calculating excitation profiles of metalloporphyrins that include the effects of symmetry-lowering (181,182).

A special case of symmetry-lowering is the reduction of a  $C_bC_b$  bond in a metalloporphyrin to form a metallochlorin. We have seen that the high frequency modes of metallochlorins are

simultaneously IR and resonance Raman active and exhibit mixing of  $C_aC_m$  and  $C_bC_b$  stretching character. The normal coordinate analysis of NiOEC by Boldt et al. (83) represented several modes as linear combinations of normal modes of NiOEP. For example, the  $1648\text{ cm}^{-1}$  mode of NiOEC in  $\text{Na}_2\text{SO}_4$  was described as a 50/50 linear in-phase combination of  $\nu_{10}$  and  $\nu_{37a}$ . It is not clear whether this is simply a convenient representation of the form of the metallochlorin normal mode or if it is actually derived by mixing of the metalloporphyrin  $\nu_{10}$  mode with the  $E_u$  mode  $\nu_{37}$  as a result of symmetry-lowering.

There are several experiments to complete the characterization of the vibrational modes of metallochlorins. Our study has concentrated on the modes above  $900\text{ cm}^{-1}$  which leaves the assignments for the low frequency modes unresolved. Also, a complication in the assignment of the  $C_mH$  modes is that the normal coordinate analysis of NiOEC predicts that the  $\alpha,\beta$  and  $\gamma,\delta$ -hydrogen motions are mixed with porphyrin skeletal modes and that the  $\gamma,\delta$ -hydrogen motions are further mixed with  $C_bH$  deformations on ring IV. Involvement of the ring IV  $C_bH$  modes can be tested by preparing CuOEC with deuterium substitution on ring IV. Results for this complex as well as the selectively methine-deuterated CuOEC complexes could then be utilized in a refinement of the normal coordinate analysis for MOEC.

Once the mode assignments for metallochlorins have been firmly established then the features that are of interest to the study of metallochlorins in nature e.g. peripheral substituents and axial ligation can be explored. Excitation profiles of the intensities and depolarization ratios of the metallochlorin Raman bands are a topic for investigation. Ozaki et al. (95) measured the depolarization ratios for the high frequency modes of CuOEC with 488.0 nm excitation and attempted to correlate the metallochlorin resonance Raman modes with those of NiOEP. However, the resonance Raman bands of CuOEC show a wide variation in the depolarization ratio depending on the excitation wavelength. For example, the 1602  $\text{cm}^{-1}$  mode of CuOEC has a depolarization ratio of 0.6 (p) at 406.7 nm, 1.0 (ap) at 488.0 nm and 0.5 (p) at 615.0 nm. Excitation profiles and depolarization ratio studies would help in understanding the resonance Raman scattering mechanism and symmetry effects in metallochlorins.

Although chlorophyll contains a chlorin macrocycle, the effects of the peripheral substituents and ring V prevent a direct correlation of the resonance Raman modes of chlorophyll with those of MOEC. Boldt et al. examined a series of Ni chlorins in which the structural features of chlorophyll a were added stepwise (83). However, only a single metal was utilized. Our results for metal-substituted chlorophyll a show that ring V plays a major role in determining the vibrational properties of chlorophyll. The normal modes of metallochlorins



and metalloporphyrins cannot be directly compared but characterization of porphyrin model compounds with an isocyclic ring would help in understanding the effects of ring V in chlorophyll. Suitable model compounds are protochlorophyll a, which is a porphyrin with the same peripheral substituents as chlorophyll a (183,184) and the porphyrin compounds prepared by Kenner and co-workers (185-187). The peripheral substituents also complicate the determination of the vibrational mode characters of chlorophyll. It is possible that vibrational modes of the conjugated carbonyl groups are mixed with those of the chlorophyll macrocycle. Centeno observed that several resonance Raman modes of heme a contained contributions from the conjugated formyl group by use of  $O^{18}$  substitution of the formyl (188). This substitution was achieved through preparation of the Schiff base of heme a followed by hydrolysis with  $H_2O^{18}$ . The same approach may be used for chlorophyll a except that the Schiff base must be prepared for pyrochlorophyll a (189). Reaction of chlorophyll a with amines to form the Schiff base would instead result in the rupture of ring V (190,191).

H-bonding to the conjugated keto and formyl carbonyls of chlorophyll a and chlorophyll b, respectively, has been proposed as a mechanism to account for the broadened and red-shifted electronic absorption bands of the chlorophylls in LHC. This conclusion is based on a comparison with the results obtained for H-bonded heme a model compounds (176).

To support the LHC results, a further study of H-bonding to the chlorophyll carbonyls could be carried out. Aggregation of chlorophyll in H-bonding solvents such as alcohols can be avoided by using the pheophytins or metal-substituted chlorophylls.

A final suggestion concerns the manner in which future resonance Raman studies of metalloporphyrins are conducted. Resonance Raman work on metalloporphyrins and hemoproteins for the past decade have relied almost exclusively on the normal coordinate analysis of NiOEP performed by Abe et al. in 1978 (55). While the mode assignments for NiOEP have benefitted the study of porphyrins, investigations of other macrocycles have been limited. Currently, the best approach is that of the Bocian group. In recent years, these workers have explored a variety of new systems including metallochlorins (83,192,193), chlorophyll model compounds (83), bacteriochlorins (193), a bacteriochlorophyll a model compound (194) and metalloporphyrin anion radicals (195). The resonance Raman spectra were supported by normal coordinate calculations for each system thus removing the reliance on the NiOEP mode assignments. It is anticipated that computer calculations will assume a much greater role in future resonance Raman studies of metalloporphyrins and other related systems.

## LIST OF REFERENCES

## LIST OF REFERENCES

1. Clayton, R.K. *Photosynthesis: Physical Mechanisms and Chemical Patterns*; Cambridge Univ. Press: Cambridge, MA, 1980.
2. Forti, G. in *Photosynthesis*; Ames, J., Ed.; Elsevier: Amsterdam, 1987; pp 1-20.
3. Hill, R.; Bendall, F. *Nature (London)* 1960, **186**, 136-137.
4. Kok, B. *Biochem. Biophys. Acta* 1956, **22**, 399-401.
5. Doring, G.; Stiehl, H.H.; Witt, H.T. *Z. Naturforsch.* 1967, **22b**, 639-644.
6. Davis, M.S.; Forman, A.; Fajer, J. *Proc. Natl. Acad. Sci. USA* 1979, **76**, 4170-4174.
7. Norris, J.R.; Uphaus, R.A.; Crespi, H.L.; Katz, J.J. *Proc. Natl. Acad. Sci. USA* 1971, **68**, 625-628.
8. Philipson, K.D.; Sato, V.L.; Sauer, K. *Biochemistry* 1972, **11**, 4591-4595.
9. Norris, J.R.; Scheer, H.; Druyan, M.E.; Katz, J.J. *Proc. Natl. Acad. Sci. USA* 1974, **71**, 4897-4900.
10. Shipman, L.L.; Cotton, T.M.; Norris, J.R.; Katz, J.J. *Proc. Natl. Acad. Sci. USA* 1976, **73**, 1791-1794.
11. Wasielewski, M.R.; Norris, J.R.; Crespi, H.L.; Harper, J. *J. Am. Chem. Soc.* 1981, **103**, 7664-7665.
12. Den Blanken, H.J.; Hoff, A.J. *Biochim. Biophys. Acta* 1983, **724**, 52-61.
13. Dikanov, S.A.; Astashkin, A.V.; Tsvetkov, Yu.D.; Goldfeld, M.G. *Chem. Phys. Lett.* 1983, **101**, 206-210.
14. O'Malley, P.J.; Babcock, G.T. *Proc. Natl. Acad. Sci. USA* 1984, **81**, 1098-1101.
15. Wasielewski, M.R.; Norris, J.R.; Shipman, L.L.; Lin, C.-P.; Svec, W.A. *Proc. Natl. Acad. Sci. USA* 1981, **78**, 2957-2961.

16. Dörnemann, D.; Senger, H. Photochem. Photobiol. 1986, 43, 573-581.
17. Watanabe, T.; Kobayashi, M.; Hongu, A.; Nakazato, M.; Hiyama, T.; Murata, N. FEBS Lett. 1985, 19, 252-256.
18. Setif, P.; Mathis, P. Arch. Biochem. Biophys. 1980, 204, 477-485.
19. Klimov, V.V.; Allakhverdiev, S.I.; Demeter, S.; Krasnovskii, A.A. Dokl. Akad. Nauk. SSSR 1979, 249, 227-230.
20. Thornber, J.P. Ann. Rev. Plant Physiol. 1975, 26, 127-158.
21. Burke, J.J.; Ditto, C.L.; Arntzen, C.J. Arch. Biochem. Biophys. 1978, 187, 252-263.
22. Glazer, A.N. Ann. Rev. Biochem. 1983, 52, 125-157.
23. Dolphin, D., Ed. The Porphyrins; Academic Press: New York, 1978; Vol. VII.
24. Scheer, H. in The Porphyrins; Dolphin, D., Ed.; Academic Press: New York, 1978; Vol. II, pp 1-44.
25. Svec, W.A. in The Porphyrins; Dolphin, D., Ed.; Academic Press: New York, 1978; Vol. V, pp 341-399.
26. Sibbet, S.S.; Hurst, J.K. Biochemistry 1984, 23, 3007-3013.
27. Babcock, G.T.; Ingle, R.T.; Oertling, W.A.; Davis, J.C.; Averill, B.A.; Hulse, C.L.; Stufkens, D.J.; Bolscher, B.G.J.M.; Wever, R. Biochem. Biophys. Acta 1985, 828, 58-66.
28. Timkovich, R.; Cork, M.S.; Gennis, R.B.; Johnson, P.Y. J. Am. Chem. Soc. 1985, 107, 6069-6075.
29. Chang, C.K. J. Biol. Chem. 1985, 260, 9520-9522.
30. Chang, C.K.; Wu, W. J. Biol. Chem. 1986, 261, 8593-8596.
31. Strauss, S.H.; Silver, M.E.; Ibers, J.A. J. Am. Chem. Soc. 1983, 105, 4108-4109.
32. Strauss, S.H.; Thompson, R.G. J. Inorg. Biochem. 1986, 27, 173-177.
33. Feng, D.; Ting, Y.-S.; Ryan, M.D. Inorg. Chem. 1985, 24, 612-617.

34. Stolzenberg, A.M.; Strauss, S.H.; Holm, R.H. J. Am. Chem. Soc. 1981, **103**, 4763-4778.
35. Strauss, S.H.; Silver, M.E.; Long, K.M.; Thompson, R.G.; Hudgens, R.A.; Spartalian, K.; Ibers, J.A. J. Am. Chem. Soc. 1985, **107**, 4207-4215.
36. Gallucci, J.C.; Swepston, P.N.; Ibers, J.A. Acta Cryst. 1982, **B38**, 2134-2139.
37. Chow, H.-C.; Serlin, R.; Strouse, C.E. J. Am. Chem. Soc. 1975, **97**, 7230-7237.
38. Jensen, A.; Aasmundrud, O.; Eimhjellen, K.E. Biochim. Biophys. Acta 1964, **88**, 466-479.
39. Strain, H.H.; Cope, B.T.; McDonald, G.N.; Svec, W.A.; Katz, J.J. Phytochemistry 1971, **10**, 1109-1114.
40. Dougherty, R.C.; Strain, H.H.; Svec, W.A.; Uphaus, R.A.; Katz, J.J. J. Am. Chem. Soc. 1970, **92**, 2826-2833.
41. Gouterman, M. J. Chem. Phys. 1958, **30**, 1139-1161.
42. Gouterman, M. J. Molec. Spectrosc. 1961, **6**, 138-163.
43. Longuet-Higgins, H.C.; Rector, C.W.; Platt, J.R. J. Chem. Phys. 1950, **18**, 1174-1181.
44. Weiss, C. in The Porphyrins; Dolphin, D., Ed.; Academic Press: New York, 1978; Vol. III, pp 211-223.
45. Kitagawa, T.; Ozaki, Y. Structure and Bonding 1987, **64**, 71-114.
46. Tang, J.; Albrecht, A.C. in Raman Spectroscopy; Szymanski, H.A., Ed.; Plenum Press: New York, 1970; pp 33-68.
47. Clark, R.J.H.; Stewart, B. Structure and Bonding 1970, **36**, 1-80.
48. Rousseau, D.L.; Friedman, J.M.; Williams, P.F. in Topics in Current Physics; Weber, A., Ed.; Springer-Verlag: Berlin, 1979; Vol. 11, pp 203-252.
49. Carey, P.R.; Salares, V.R. in Advances in Infrared and Raman Spectroscopy; Clark, R.J.H.; Hester, R.E., Eds.; Heyden: London, 1980; Vol. 7, pp 1-58.
50. Parker, F.S. Applications of Infrared, Raman, and Resonance Raman Spectroscopy in Biochemistry; Plenum Press: New York, 1983.

51. Spiro, T.G., Ed. *Biological Applications of Raman Spectroscopy*; Wiley: New York, 1988; Vol. 3.
52. Felton, R.H.; Yu, N.-T. in *The Porphyrins*; Dolphin, D., Ed.; Academic Press: New York, 1978; Vol. III, pp 347-393.
53. Spiro, T.G. in *Iron Porphyrins*; Lever, A.B.P.; Gray, H.B., Eds.; Addison-Wesley: Reading, MA, 1983; Part Two, pp 89-159.
54. Babcock, G.T. in *Biological Applications of Raman Spectroscopy*; Spiro, T.G., Ed.; Wiley: New York, 1988; Vol. 3, pp 293-346.
55. Abe, M.; Kitagawa, T.; Kyogoku, Y. *J. Chem. Phys.* 1978, **69**, 4526-4534.
56. Abe, M. in *Spectroscopy of Biological Systems*; Clark, R.J.H.; Hester, R.E., Eds.; Wiley: London, 1986; pp 347-393.
57. Kitagawa, T.; Ogoshi, H.; Watanabe, E.; Yoshida, Z. *J. Phys. Chem.* 1975, **79**, 2629-2635.
58. Kitagawa, T.; Abe, M.; Kyogoku, Y.; Ogoshi, H.; Watanabe, E.; Yoshida, Z. *J. Phys. Chem.* 1976, **80**, 1181-1186.
59. Kitagawa, T.; Abe, M.; Ogoshi, H. *J. Chem. Phys.* 1978, **69**, 4516-4525.
60. Cullen, D.L.; Meyer, E.F. Jr. *J. Am. Chem. Soc.* 1974, **96**, 2095-2102.
61. Spaulding, L.D.; Chang, C.C.; Yu, N.-T.; Felton, R.H. *J. Am. Chem. Soc.* 1975, **97**, 2517-2525.
62. Huong, P.V.; Pommier, J.-C. *C. R. Acad. Sci. Paris* 1977, **C285**, 519-522.
63. Spiro, T.G.; Stong, J.D.; Stein, P. *J. Am. Chem. Soc.* 1979, **101**, 2648-2655.
64. Callahan, P.M.; Babcock, G.T. *Biochemistry* 1981, **20**, 952-958.
65. Choi, S.; Spiro, T.G.; Langry, K.C.; Smith, K.M.; Budd, D.L.; La Mar, G.N. *J. Am. Chem. Soc.* 1982, **104**, 4345-4351.
66. Ozaki, Y.; Iriyama, K.; Ogoshi, H.; Ochiai, T.; Kitagawa, T. *J. Phys. Chem.* 1986, **90**, 6105-6112.
67. Teraoka, J.; Kitagawa, T. *J. Phys. Chem.* 1980, **84**, 1928-1935.

68. Lutz, M. C. R. Acad. Sci. Paris 1972, B275, 497-500.
69. Lutz, M. and Breton, J. Biochem. Biophys. Res. Commun. 1973, 53, 413-418.
70. Lutz, M. J. Raman Spectrosc. 1974, 2, 497-516.
71. Lutz, M.; Kleo, J. C. R. Acad. Sci. Paris 1974, D279, 1413-1416.
72. Lutz, M.; Kleo, J.; Gilet, R.; Henry, M.; Plus, R.; Leickman, J.P. in Proc. 2nd. International Conference on Stable Isotopes, Oak Brook, IL; Klein, E.R.; Klein, P.D., Eds.; U.S. Dept. of Commerce: Springfield, VA, 1975; pp 462-469.
73. Lutz, M. in Lasers in Physical Chemistry and Biophysics; Joussot-Dubien, J., Ed.; Elsevier: Amsterdam, 1975; pp 451-463.
74. Lutz, M. Biochem. Biophys. Acta 1977, 460, 408-430.
75. Lutz, M.; Brown, J.S.; Remy, R. in Chlorophyll Organization and Energy Transfer in Photosynthesis; Wolstenholme, G.; Fitzsimons, D.W., Eds.; Excerpta Medica: Amsterdam, 1979; pp 105-125.
76. Lutz, M. in Advances in Infrared and Raman Spectroscopy; Clark, R.J.H.; Hester, R.E., Eds.; Wiley Heyden: London, 1983; Vol. 11, pp 211-300.
77. Nanba, O.; Satoh, K. Proc. Natl. Acad. Sci. USA 1987, 84, 109-112.
78. Akabori, K.; Tsukamoto, H.; Tsukihara, J.; Nagatsuka, T.; Motokawa, O.; Toyoshima, Y. Biochem. Biophys. Acta 1988, 932, 345-357.
79. Ghanotakis, D.F.; de Paula, J.C.; Demetriou, D.M.; Bowlby, N.R.; Petersen, J.; Babcock, G.T.; Yocum, C.F. Biochim. Biophys. Acta 1989, 974, 44-53.
80. Whitlock, H.W.Jr.; Hanauer, R.; Oester, M.Y.; Bower, B.K. J. Am. Chem. Soc. 1969, 91, 7485-7489.
81. Eisner, U.; Linstead, R.P.; Parkes, E.A.; Stephen, E. J. Chem. Soc. 1956, 1655-1661.
82. Falk, J.E. in Porphyrins and Metalloporphyrins; Elsevier: New York, 1964; p 798.
83. Boldt, N.J.; Donohoe, R.J.; Birge, R.R.; Bocian, D.F. J. Am. Chem. Soc. 1987, 109, 2284-2298.



84. Bonnett,R.; Stephenson,G.F. Proc. Chem. Soc. 1964, 291.
85. Salehi,A.; Fonda,H.N.; Oertling,A.W.; Babcock,G.T.; Chang,C.K. J. Labeled Compd. Radiopharm. 1988, **XXV**, 1333-1337.
86. Eisner,U. J. Chem. Soc. 1957, 3461-3469.
87. Omata,T.; Murata,N. Plant & Cell Physiol. 1983, **24**, 1093-1100.
88. Iriyama,K.; Ogura,N.; Takamiya,A. J. Biochem. 1974, **76**, 901-904.
89. Kenner,G.W.; McCombie,S.W.; Smith,K.M. J. Chem. Soc., Perkin Trans. 1973, **1**, 2517-2523.
90. Boucher,L.J.; Katz,J.J. J. Am. Chem. Soc. 1967, **89**, 4703-4708.
91. Mackinney,G. J. Biol. Chem. 1941, **140**, 315-322.
92. Ghanotakis,D.F.; Demetriou,D.M.; Yocum,C.F. Biochim. Biophys. Acta 1987, **891**, 15-21.
93. Kean,R.T. Ph.D. Thesis; Michigan State University: East Lansing, MI, 1987.
94. Ogoshi,H.; Watanabe,E.; Yoshida,Z.; Kincaid,J.; Nakamoto, K. Inorg. Chem. 1975, **14**, 1344-1350.
95. Ozaki,Y.; Kitagawa,T.; Ogoshi,H. Inorg. Chem. 1979, **18**, 1772-1776.
96. Ozaki,Y.; Iriyama,K.; Ogoshi,H.; Ochiai,T.; Kitagawa,T. J. Phys. Chem. 1986, **90**, 6113-6118.
97. Andersson,L.A.; Loehr,T.M.; Chang,C.K.; Mauk,A.G. J. Am. Chem. Soc. 1985, **107**, 182-191.
98. Andersson,L.A.; Sotiriou,C.; Chang,C.K.; Loehr,T.M. J. Am. Chem. Soc. 1987, **109**, 258-264.
99. Oertling,W.A.; Salehi,A.; Chang,C.K.; Babcock,G.T. J.Phys. Chem. 1989, **93**, 1311-1319.
100. Kincaid,J.R.; Urban,M.W.; Watanabe,T.; Nakamoto,K. J. Phys. Chem. 1983, **87**, 3096-3101.
101. The  $\nu_{11}$  mode appears as a shoulder on the broad  $\nu_2$  band in the resonance Raman spectra of CuOEP and CuOEP-d<sub>2</sub> with Soret excitation at 406.7 nm. With 363.8 nm excitation, the spectra of CuOEP and CuOEP-d<sub>4</sub> obtained by Oertling et al. (99) show an increase in the relative intensity of

$\nu_{11}$  compared to  $\nu_2$  and no frequency shift upon d, methine deuteration.

102. Ozaki *et al.* (95) assigned the  $1602\text{ cm}^{-1}$  mode of CuOEC as dp and the  $1584\text{ cm}^{-1}$  mode as ap. These polarizations should be reversed, i.e.  $1602\text{ (ap)}$  and  $1584\text{ (dp)}$ .
103. Moustakali, I.; Tulinsky, A. J. Am. Chem. Soc. 1973, **95**, 6811-6815.
104. Collins, D.M.; Hoard, J.L. J. Am. Chem. Soc. 1970, **92**, 3761-3771.
105. Kitagawa, T.; Ogoshi, H.; Watanabe, E.; Yoshida, Z. J. Phys. Chem. 1975, **79**, 2629-2635.
106. The K values reported by Ozaki *et al.* (66) for the FeOEP high frequency resonance Raman modes follow the same relative order as the K values based on Ni, Cu and ZnOEP (Table 3.5) but are all higher:  $\nu_{10}$  (K=495),  $\nu_2$  (K=322),  $\nu_{19}$  (K=576),  $\nu_{11}$  (K=288) and  $\nu_3$  (K=414). Using the same porphyrin core-sizes for the FeOEC complexes and their previous mode assignments for chlorins, the K values obtained for the chlorins were: " $\nu_{10}$ " (K=472), " $\nu_2$ " (K=404), " $\nu_{19}$ " (K=332), " $\nu_{11}$ " (K=367) and " $\nu_3$ " (K=347). On this basis, the K values for the chlorin  $C_bC_b$  modes " $\nu_2$ " and " $\nu_{11}$ " are higher than the chlorin  $C_aC_m$  modes " $\nu_{19}$ " and " $\nu_3$ ". Moreover, the frequencies predicted for CuOEC and ZnOEC based on the FeOEC core-size correlation parameters of Ozaki are too low (CuOEC: 1633, 1593, 1579, 1538 and  $1500\text{ cm}^{-1}$ ; ZnOEC: 1611, 1574, 1564, 1521 and  $1484\text{ cm}^{-1}$ ).
107. The six  $C_aN$  stretching modes are derived from the  $\nu_4$ ,  $\nu_{12}$ ,  $\nu_{20}$ ,  $\nu_{22}$  and  $\nu_{41}$  modes of NiOEP. The most recent normal coordinate treatment of the  $E_u$  modes of NiOEP by Abe (56) assigned the P.E.D. of  $\nu_{45}$  to  $C_aC_m$  stretching and not  $C_aN$  stretching (55).
108. The  $1157\text{ cm}^{-1}$  mode of CuOEC and  $1154\text{ cm}^{-1}$  mode of NiOEC are overlapped by the  $1154\text{ cm}^{-1}$  band of  $\text{CH}_2\text{Cl}_2$ . The presence of these modes is confirmed by the resonance Raman spectra in KBr that show an  $1155\text{ cm}^{-1}$  mode for CuOEC and an  $1153\text{ cm}^{-1}$  mode for NiOEC.
109. Ogoshi, H.; Saito, Y.; Nakamoto, K. J. Chem. Phys. 1972, **57**, 4194-4202.
110. Stein, P.; Burke, J.M.; Spiro, T.G. J. Am. Chem. Soc. 1975, **97**, 2304-2305.
111. Sunder, S.; Bernstein, H. J. Raman Spectrosc. 1976, **5**, 351-371.

112. Susi, H.; Ard, J.S. *Spectrochim. Acta* 1977, **33A**, 561-567.
113. Gladkov, L.L.; Gradyushko, A.T.; Shulga, A.M.; Solovyov, K.N.; Starukhin, A.S. *J. Mol. Struct.* 1978, **47**, 463-493.
114. Warshel, A.; Lippicirella, A. *J. Am. Chem. Soc.* 1981, **103**, 4664-4673.
115. Gladkov, L.L.; Solovyov, K.N. *Spectrochim. Acta* 1986, **42A**, 1-10.
116. Lee, H.; Kitagawa, T.; Abe, M.; Pandey, R.K.; Leung, H.-K.; Smith, K.M. *J. Mol. Struct.* 1986, **146**, 329-347.
117. Lutz, M.; Kleo, J. *Biochim. Biophys. Acta* 1979, **546**, 365-369.
118. Salehi, A.; Oertling, W.A.; Babcock, G.T.; Chang, C.K. *J. Am. Chem. Soc.* 1986, **108**, 5630-5631.
119. Salehi, A.; Oertling, W.A.; Babcock, G.T.; Chang, C.K. *Inorg. Chem.* 1987, **26**, 4296-4298.
120. Oertling, W.A.; Salehi, A.; Chung, Y.C.; Leroy, G.E.; Chang, C.K.; Babcock, G.T. *J. Phys. Chem.* 1987, **91**, 5887-5898.
121. Salehi, A.; Oertling, W.A.; Fonda, H.N.; Babcock, G.T.; Chang, C.K. *Photochem. Photobiol.* 1988, **48**, 525-530.
122. Chang, C.K. *Biochemistry* 1980, **19**, 1971-1976.
123. Spangler, D.; Maggiora, G.M.; Shipman, L.L.; Christoffersen, R.E. *J. Am. Chem. Soc.* 1977, **99**, 7470-7477.
124. Forman, A.; Renner, M.W.; Fujita, E.; Barkigia, K.M.; Evans, M.C.W.; Smith, K.M.; Fajer, J. *Israel J. Chem.* 1989, **29**, 57-64.
125. X-ray crystal structures of the metalloporphyrin cation radicals  $\text{Mg}(\text{ClO}_4^-)\text{TPP}^+$  (126) and  $\text{Zn}(\text{ClO}_4^-)\text{TPP}^+$  (127) show non-planarity of the porphyrin macrocycle. This distortion is attributed to non-bonding interactions of the coordinated perchlorate ion and phenyl groups (120, 128-130).
126. Barkigia, K.M.; Spaulding, L.D.; Fajer, J. *Inorg. Chem.* 1983, **22**, 349-351.
127. Spaulding, L.D.; Eller, P.G.; Bertrand, J.A.; Felton, R.H. *J. Am. Chem. Soc.* 1974, **96**, 982-987.

128. Scholz, W.F.; Reed, C.A.; Lee, Y.J.; Scheidt, W.R.; Lang, G. J. Am. Chem. Soc. 1982, 104, 6791-6793.
129. Reed, C.A.; Mashiko, T.; Bentley, S.P.; Kestner, M.E.; Scheidt, W.R.; Spartalian, K.; Lang, G. J. Am. Chem. Soc. 1979, 101, 2948-2958.
130. Masuda, H.; Taga, T.; Osaki, K.; Sugimoto, H.; Yoshida, Z.-I.; Ogoshi, H. Inorg. Chem. 1980, 19, 950-955.
131. Strekas, T.C.; Spiro, T.G. Biochim. Biophys. Acta 1972, 263, 830-833.
132. Spiro, T.G.; Strekas, T.C. Proc. Natl. Acad. Sci. U.S.A. 1972, 69, 2622-2626.
133. Brunner, H.; Mayer, A.; Sussner, H. J. Mol. Biol. 1972, 70, 153-156.
134. Fonda, H.N.; Babcock, G.T. in Progress in Photosynthesis Research; Biggins, J., Ed.; Martinus Nijhoff: Dordrecht, The Netherlands, 1987; Vol. I, pp 449-452.
135. Fujiwara, M.; Tasumi, M. J. Phys. Chem. 1986, 90, 5646-5650.
136. Heald, R.L.; Callahan, P.M.; Cotton, T.M. J. Phys. Chem. 1988, 92, 4820-4824.
137. Lutz, M.; Kleo, J. Biochem. Biophys. Res. Comm. 1976, 69, 711-717.
138. Cotton, T.M.; Van Duyne, R.P. Biochem. Biophys. Res. Comm. 1978, 82, 424-433.
139. Cotton, T.M.; Parks, K.D.; Van Duyne, R.P. J. Am. Chem. Soc. 1980, 102, 6399-6407.
140. Cotton, T.M.; Van Duyne, R.P. J. Am. Chem. Soc. 1981, 103, 6020-6026.
141. Wagner, W.-D.; Waidelich, W. Appl. Spectrosc. 1986, 40, 191-195.
142. Fujiwara, M.; Tasumi, M. J. Phys. Chem. 1986, 90, 250-255.
143. Shipman, L.L.; Cotton, T.M.; Norris, J.R.; Katz, J.J. J. Am. Chem. Soc. 1976, 98, 8222-8230.
144. Lutz, M.; Hoff, A.J.; Brehmet, L. Biochim. Biophys. Acta 1982, 679, 331-341.

145. Robert, B.; Vermeglio, A.; Lutz, M. *Biochim. Biophys. Acta* 1984, **766**, 259-262.
146. Robert, B.; Lutz, M. *Biochim. Biophys. Acta* 1985, **807**, 10-23.
147. Agalidis, I.; Lutz, M.; Reiss-Husson, F. *Biochim. Biophys. Acta* 1984, **766**, 188-197.
148. Robert, B.; Lutz, M. *Biochemistry* 1986, **25**, 2303-2309.
149. Kuhlbrandt, W. *Nature (London)* 1984, **307**, 478-480.
150. Li, J. *Proc. Natl. Acad. Sci. USA* 1985, **82**, 386-390.
151. Babcock, G.T. in *Photosynthesis*; Ames, J., Ed.; Elsevier: Amsterdam, 1987; pp 125-158.
152. Berthold, D.A.; Babcock, G.T.; Yocum, C.F. *FEBS Lett.* 1981, **134**, 231-234.
153. Ghanotakis, D.F.; Babcock, G.T.; Yocum, C.F. *Biochim. Biophys. Acta* 1984, **765**, 388-398.
154. Mathis, P.; Rutherford, A.W. in *Photosynthesis*; Ames, J., Ed.; Elsevier: Amsterdam, 1987; pp 63-96.
155. Michel, H. *J. Mol. Biol.* 1982, **158**, 567-572.
156. Deisenhofer, J.; Epp, O.; Miki, K.; Huber, R.; Michel, H. *J. Mol. Biol.* 1984, **180**, 385-398.
157. Deisenhofer, J.; Epp, O.; Miki, K.; Huber, R.; Michel, H. *Nature (London)* 1985, **318**, 618-624.
158. Michel, H.; Deisenhofer, J. in *Progress in Photosynthesis Research*; Biggins, J., Ed.; Martinus Nijhoff: Dordrecht, The Netherlands, 1987; Vol. I, pp 353-362.
159. Allen, J.P.; Feher, G. *Proc. Natl. Acad. Sci. USA* 1984, **81**, 4795-4799.
160. Chang, C.-H.; Schiffer, M.; Tiede, D.; Smith, U.; Norris, J. *J. Mol. Biol.* 1985, **186**, 201-203.
161. Allen, J.P.; Feher, G.; Yeates, T.O.; Komiyama, H.; Rees, D.C. *Proc. Natl. Acad. Sci. USA* 1987, **84**, 6162-6166.
162. Wright, K.A.; Boxer, S.G. *Biochemistry* 1981, **20**, 7546-7556.
163. Eccles, J.; Honig, B. *Proc. Natl. Acad. Sci. USA* 1983, **80**, 4959-4962.

164. Katz, J.J.; Shipman, L.L.; Cotton, T.M.; Janson, T.R.  
in *The Porphyrins*; Dolphin, D., Ed.; Academic Press: New  
York, 1978; Vol. V, pp 401-458.
165. Cotton, T.M.; Trifunac, A.D.; Ballschmiter, K.; Katz, J.J.  
*Biochim. Biophys. Acta* 1974, **368**, 181-198.
166. Ward, B.; Callahan, P.M.; Young, R.; Babcock, G.T.;  
Chang, C.K. *J. Am. Chem. Soc.* 1983, **105**, 634-636.
167. Maggiora, L.L.; Maggiora, G.M. *Photochem. Photobiol.*  
1984, **39**, 847-849.
168. Ward, B.; Chang, C.K.; Young, R. *J. Am. Chem. Soc.* 1984,  
**106**, 3943-3950.
169. Hanson, L.K.; Chang, C.K.; Ward, B.; Callahan, P.M.;  
Babcock, G.T.; Head, J.D. *J. Am. Chem. Soc.* 1984, **106**,  
3950-3958.
170. French, C.S.; Brown, J.S.; Lawrence, M.C. *Plant Physiol.*  
1972, **49**, 421-429.
171. Brown, J.S. *Ann. Rev. Plant Physiol.* 1972, **23**, 73-86.
172. Babcock, G.T.; Callahan, P.M.; Ondrias, M.R.; Salmeen, I.  
*Biochemistry* 1981, **20**, 959-966.
173. Lutz claimed to observe both 5 and 6-coordinate  
chlorophyll b in LHC based on the relative intensities  
of two low frequency bands at 312 and 304  $\text{cm}^{-1}$  (75). The  
312  $\text{cm}^{-1}$  component was attributed to 5-coordinate  
chlorophyll b and the 304  $\text{cm}^{-1}$  component was attributed  
to 6-coordination. Lutz has proposed (76) for chlorophyll  
b that a single band at 300-310  $\text{cm}^{-1}$  with a half-bandwidth  
of 25  $\text{cm}^{-1}$  or less at 30 K and 27  $\text{cm}^{-1}$  or less at 300 K  
indicates 6-coordination. A 5-coordinate Mg is indicated  
by the presence of an additional band at 310-320  $\text{cm}^{-1}$  with  
an increase of half-bandwidth to 28-35  $\text{cm}^{-1}$ . However,  
these criteria are not reliable predictors of the Mg  
coordination state. For example, chlorophyll b in acetone  
solution at room temperature is predicted by Lutz to have  
6-coordination (76) but the frequencies of the core-size  
sensitive modes indicate 5-coordination (142).
174. Matthews, B.W.; Fenna, R.E.; Bolognesi, M.C.; Schmid, M.F.;  
Olson, J.M. *J. Mol. Biol.* 1979, **131**, 259-285.
175. Koyama, Y.; Umemoto, Y.; Akamatsu, A.; Uehara, K.;  
Tanaka, M. *J. Mol. Struct.* 1986, **146**, 273-287.
176. Babcock, G.T.; Callahan, P.M. *Biochemistry* 1983, **22**,  
2314-2319.

177. Willems,D.L.; Bocian,D.F. J. Am. Chem. Soc. 1984, 106, 880-890.
178. Willems,D.L.; Bocian,D.F. J. Phys. Chem. 1985, 89, 234-239.
179. Choi,S.; Spiro,T.G.; Langry,K.C.; Smith,K.M. J. Am. Chem. Soc. 1982, 104, 4337-4344.
180. Meyer,E.F.Jr. Acta Cryst. 1972, B28, 2162-2167.
181. Shelnutt,J.A. J. Chem. Phys. 1980, 72, 3948-3958.
182. Shelnutt,J.A. J. Chem. Phys. 1981, 74, 6644-6657.
183. Houssier,C.; Sauer,K. Biochim. Biophys. Acta 1969, 172, 476-491.
184. Houssier,C.; Sauer,K. Biochim. Biophys. Acta 1969, 172, 492-502.
185. Cox,M.T.; Howarth,T.T.; Jackson,A.H.; Kenner,G.W. J. Chem. Soc. Perkin I 1974, 512-516.
186. Cox,M.T.; Jackson,A.H.; Kenner,G.W.; McCombie,S.W.; Smith,K.M. J. Chem. Soc. Perkin I 1974, 516-527.
187. Kenner,G.W.; McCombie,S.W.; Smith,K.M. J. Chem. Soc. Perkin I 1974, 527-530.
188. Centeno,J. Ph.D. Thesis; Michigan State University: East Lansing, MI, 1987.
189. Pennington,F.C.; Strain,H.H.; Svec,W.A.; Katz,J.J. J. Am. Chem. Soc. 1964, 86, 1418-1426.
190. Pennington,F.C.; Boyd,S.D.; Horton,H.; Taylor,S.W.; Wolf,D.G.; Katz,J.J.; Strain,H.H. J. Am. Chem. Soc. 1967, 89, 3871-3875.
191. Pennington,F.C.; Boettcher,N.B.; Katz,J.J. Bioorganic Chemistry 1974, 3, 204-212.
192. Boldt, N.J.; Bocian,D.F. J. Phys. Chem. 1988, 92, 581-586.
193. Donohoe,R.J.; Atamian,M.; Bocian,D.F. J. Phys. Chem. 1989, 93, 2244-2252.
194. Donohoe,R.J.; Frank,H.A.; Bocian,D.F. Photochem. Photobiol. 1988, 48, 531-537.
195. Atamian,M.; Donohoe,R.J.; Lindsey,J.S.; Bocian,D.F. J. Phys. Chem. 1989, 93, 2236-2243.





MICHIGAN STATE UNIV. LIBRARIES



31293006299345